

FP7-PEOPLE-2008-IAPP : Indoor radio network PLANning and optimization

Contractual date of delivery to EC: before Month 48

Actual date of delivery to EC: 29/06/2013

Lead beneficiary: INSA Lyon

Nature: Restricted

Version: 1.0

Project Name: Indoor radio network PLANning and optimisation

Acronym: iPLAN

Start date of project: 01/06/2009 **Duration:** 48 Months

Project no.: 230745

Leading editor : Guillaume Villemaud

Contributors : Luis Goncalvez, Guillaume Villemaud, Meiling Luo, Jialai Weng and Peng Wang

1. Summary

In the context of Femtocell deployment, the important issue of interaction between outdoor macrocells and indoor femtocells is to propose some efficient tools to simulate the behavior of radio waves at the interface between the two kinds of environments: the large scale outdoor and the smaller scale indoor environments.

In this report, we present some measurement campaigns which have been performed to validate and calibrate the simulation tools developed in this project.

2. Description of the work

1. Introduction

The ubiquitous deployment of various wireless communication networks, particularly in urban areas, requires careful planning of new wireless networks, as well as optimization of the existing ones. Successful accomplishment of these tasks calls for efficient radio network design tools.

Unavoidably, any debate about merits and demerits peculiar to a concrete tool, or more precisely, to an underlying electromagnetic wave propagation modeling approach, leads to a discussion about the trade-off between the computational load and the achievable accuracy

of the prediction. To a large extent, the compromise between efficiency and accuracy depends on the modeled propagation environment.

It has been demonstrated that the multi-resolution frequency domain ParFlow (MR-FDPF) method [20] is an efficient and accurate radio network design tool for indoor and indoor-like environments. Yet the computational load associated with this method quickly becomes excessively large due to the size increase of the propagation environment as, for example, in outdoor wave propagation scenarios. On the other hand, the well-known ray-optical approaches [10] are widely used for modeling the outdoor as well as indoor environments. Even so, using the ray-optical methods for accurate prediction of the electrical field strength inside a building might not be as computationally efficient as employing the MR-FDPF method. Moreover, MR-FDPF method is usually more accurate since it does not restrict the number of reflections to be computed as it is the case in ray-optical approaches.

For scenarios where both the indoor and outdoor wave propagations have to be considered, a combination of the MR-FDPF and the ray-optical methods promises advantages in providing accurate prediction results without sacrificing the computational efficiency. Indeed, performing the simulation of the whole indoor-to-outdoor scenario based on MR-FDPF only would require too much memory.

Moreover, to further enrich the prediction of the radio link quality, much more statistics than only a mean power value are required. The discrete method of MR-FDPF intrinsically offers the potential of such a statistical analysis. In this report we describe all the measurements done to validate our tools, not only for power measurements, but also for fading statistics, time-domain statistics, and finally for a bit-error-rate estimation.

2. Indoor to outdoor and outdoor to indoor simulation tool

Before describing more in details the measurements and the additional developments on the propagation tool, we here briefly summarize the previous studies on I2O and O2I, already presented in details in deliverable D1.3.

2.1 O2I: outdoor to indoor scenarios

Taking into consideration the properties described in D1.3, it appears as an optimal choice to select the most appropriate approach depending in the location, i.e.:

- **Indoors:** The scenario is not very large, and it is made of numerous walls. Thus, normally the number of reflections/diffractions is very high. Moreover, in case of multi-floored buildings, the scenario at each floor is quite flat i.e. a 2D approximation of the propagation is a suitable assumption. Hence in this case a 2D FD model such as MR-FDPF appears to be the most favorable.
- **Outdoors:** The environment is not flat and cannot be easily approximated with a 2D model, in particular in scenarios with high buildings where antennas can be located on the roofs. Furthermore, there is more open space areas and the number of reflections to compute is smaller than indoors. Finally the size of the scenario is too large to be computed with a FD model. That is why in this case a 3D RO model such as IRLA is preferred.

Hence the new model for outdoor to indoor predictions proposed in this project combines IRLA (for the outdoor propagation part) with MR-FDPF (for the in-building propagation).

2.1.1 IRLA for outdoor

The outdoor IRLA prediction is performed. 3D rays are launched in all the directions and recursively reflected and diffracted on the obstacles. The tool is based on a maximum number of 15 reflections and 15 diffractions, which provides high accuracy. Since IRLA has a cube approach, a resolution of 5cm is chosen, i.e. the received signal power is computed every 5 centimeters. The 3D antenna pattern is generated from horizontal and vertical 2D antenna pattern obtained from the data sheets.

2.1.2 Wiplan (MR-FDPF) for indoor

In each cube located on the borders of the building (at the height corresponding to the floor), the amplitudes and directions of all the N rays reaching the cube are stored. Each arriving ray is represented by a vector v_i and the equivalent ParFlow source (flows are represented by complex numbers [20]) can be computed from the vector V corresponding to all the rays, i.e. $V = \sum_{i=0}^{N-1} v_i$. In this case, the amplitude of the equivalent source corresponds to the amplitude of V and the phase of the equivalent source corresponds to the direction of V .

The indoor radio coverage is computed in 2D (a 5cm resolution 2D cut of the scenario at the height of the floor is taken) using the MR-FDPF model and using the previously calculated equivalent sources. It is to be noticed that, due to the properties of MR-FDPF model, the complexity of simulating many sources (i.e. all the borders of the building) is in the same order than for one source only.

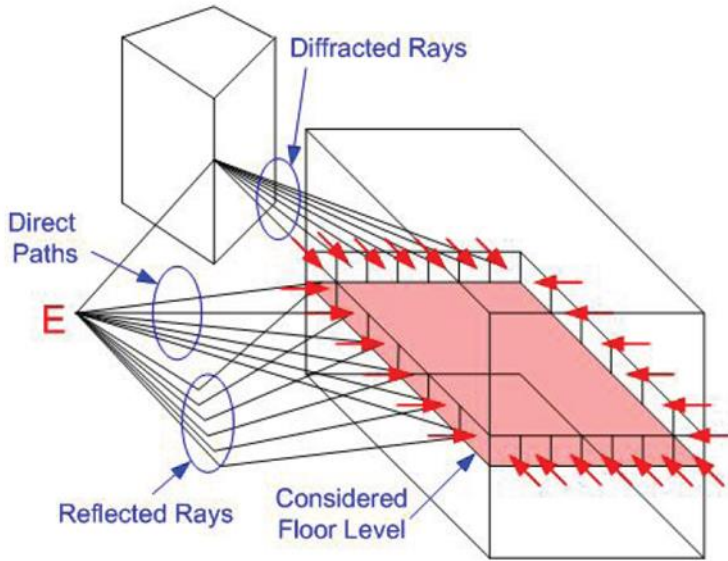


Figure 2.1: Schematic representation of the combined approach. First the outdoor part is simulated, then the incoming indoor flows are computed and used for the indoor simulation.

2.2 I2O: indoor to outdoor scenarios

As it has been mentioned above, the MR-FDPF method can be directly interfaced with the ray-optical methods, even for the reverse problem of indoor-to-outdoor propagation.

2.2.1 Principle of MR-FDPF to IRLA link

In this section, we propose a method that allows combining the MR-FDPF method and the ray-optical methods in attempt to efficiently model indoor-to-outdoor propagation environments.

At every point characterized by the radius-vector \mathbf{r} , the complex scalar electrical field strength $E(\mathbf{r}, f)$ predicted by the MR-FDPF method at the frequency $f \in B$, where B denotes the signal bandwidth, satisfies the wave equation [20].

Thus, it is eligible to approximate the field strength by a finite sum of plane waves arriving at the point from different directions, i.e.,

$$E(\mathbf{r}, f) = \sum_{n=1}^N g_n e^{-j2\pi f \tau_n} e^{-j\langle \mathbf{k}_n, \mathbf{r} \rangle} + w(\mathbf{r}, f) \quad (2.1)$$

where each of the N plane waves is characterized by the complex-value amplitude g_n , propagation delay τ_n , and the wave vector \mathbf{k}_n pointing in the direction of the wave propagation.

The operator $\langle \cdot \rangle$ denotes the scalar product of two vectors.

The term $w(r, f)$ in Eq. 2.1 (the approximation error) corresponds to the diffuse wave component (see, e.g., [20]).

In spite of the deterministic nature of the MR-FDPF method, we assume that the field strength $E(r, f)$ in Eq. 2.1 predicted by the MR-FDPF method is a single available realization of the corresponding stochastic process. To some degree, this assumption can be justified by observing that multiple uncertainties are inherent in modeling of any complex propagation scenario. For example, adjustments (corrections) made to the model geographical database, would result in a new realization of the predicted field strength $E(r, f)$. We also presume that the term $w(r, f)$ is a realization of the random zero-mean Gaussian process uncorrelated with respect to the frequency and the spatial position.

The task is to estimate the parameters $\{g_n, \tau_n, \mathbf{k}_n\}_{n=1}^N$ from the values of the electrical field strength predicted by the MR-FDPF method at the point r and its vicinity.

For this purpose, we employ the space-alternating generalized expectation-maximization algorithm (SAGE) [9], [10]. Note that under the assumptions made above, the estimates $\{\hat{g}_n, \hat{\tau}_n, \hat{\mathbf{k}}_n\}_{n=1}^N$ asymptotically approach the maximum likelihood (ML) estimates.

As the parameter estimates $\{\hat{g}_n, \hat{\tau}_n, \hat{\mathbf{k}}_n\}_{n=1}^N$ are determined for all points along the border of the propagation environment covered by MR-FDPF method, the rays can be launched in the directions defined by the wave vectors $\hat{\mathbf{k}}_n$ pointing outside of the indoor area. A further propagation of the rays is controlled by the ray-optical method, where the rays are propagated in the outdoor environment, thus allowing to compute the received signal in the whole scenario. In the next section a measurement campaign is performed in order to evaluate the performance of this approach.

3. Measurements at INSA Lyon

Three main kinds of measurements were performed or exploited at INSA Lyon in order to validate and calibrate the models:

- power only measurements, to validate: coverage maps for the indoor tool, hybridization of the outdoor and indoor tools, and small scale and large scale fading evaluation;
- channel sounding, to validate the time domain statistical evaluation;
- bit-error-rate transmission, to validate the full radio link quality evaluation.

3.1 Power only measurements

Most of the radio propagation tools provide coverage maps, thus only mean power values obtained in the simulated area. This is of course a meaningful criterion to have a global view of the quality of a wireless network deployment, even if in this project we will provide more detailed characteristics. Therefore, we first present here the most significant measurements that we have performed on the received power.

3.1.1 Theoretical Background

In wireless telecommunications, the term "path loss", in decibel (dB), is defined as the transmitted power minus the received power. Thus, path loss represents the signal attenuation introduced by the propagation channels. It is always a positive quantity. Due to the complexity of radio propagation

environments and various propagation mechanisms, in reality, the instantaneous path loss is a combination of the mean path loss, the large scale fading and the small scale fading as shown in Fig. 3.1. Among these, the mean path loss is considered to be deterministic while the large scale fading, i.e. the shadow fading, and the small scale fading are usually described statistically. The channel models which tackle the relationship between the mean path loss and the Tx-Rx (Transmitter and Receiver) separation distances are called the path loss models. Those which tackle the large scale fading and the small scale fading are called the large scale fading models and the small scale fading models, respectively.

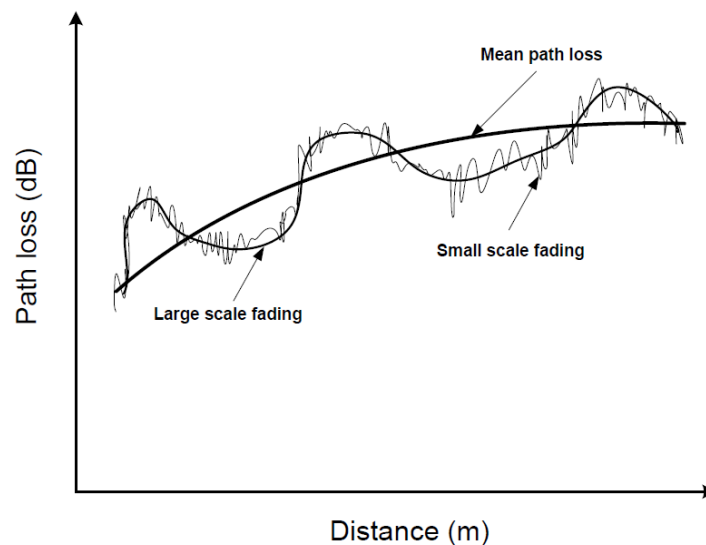


Figure 3.1: Addition of the three phenomena: pathloss, shadowing and fading.

Therefore, we have performed power measurements not only to validate the mean power prediction of our simulation tool, but also to prove that the fine accuracy of this discrete tool is able to capture efficiently the three phenomena: pathloss, large scale fading (shadowing) and small scale fading.

3.1.2 Model calibration

In the case when the parameters corresponding to the materials are not perfectly well known it may be useful to calibrate the model. This is the common approach used by all propagation tools and most of commercial network planning software such as [11, 12]. Since the number of materials could be high it is not possible to test all the possible values in a short time. That is why meta-heuristic methods have been implemented:

- Calibration of IRLA is based on Simulated Annealing [27].
- Calibration of MR-FDPF is calibrated using the Direct Search algorithm [28].

The choice of a search method is due to the fact that IRLA has few parameters to optimize (since the buildings are represented by a single material) which can be solved in a short time using Simulated Annealing. On the contrary MR-FDPF models all the materials of the different walls (for example in the later scenario there are 3 kinds of walls with 2 coefficients for each of them) which cannot be optimized in a short time using Simulated Annealing. Therefore Direct Search is chosen providing a less accurate result but in a shorter time. Let us remind that the model we propose in this paper is aimed at wireless network planners, i.e. the calibration of the materials has to be performed in a

short time, and since all the elements of the scenario (such as passing users, furniture) are not simulated, reaching the absolute global minimum is not of practical use.

The function to minimize during the calibration is the Root Mean Square Error (RMSE) defined as:

$$RMSE = \sqrt{\frac{1}{N} \cdot \sum_{i=0}^{N-1} (M_i - S_i)^2} \tag{3.1}$$

where:

N is the number of comparison points,

M_i is the measured received signal at location i ,

S_i is the simulated received signal at location i .

Typically, calibration of IRLA takes few seconds (since all the rays as stored in the memory it is not required to run numerous simulations), whereas MR-FDPF is calibrated in few minutes because multiple independent predictions have to be run. Based on our experience, calibration is important mostly outdoors where database information of the environment is limited, and due to more frequent unpredictable phenomena such as moving vehicles and fast fading.

3.1.3 Indoor measurements

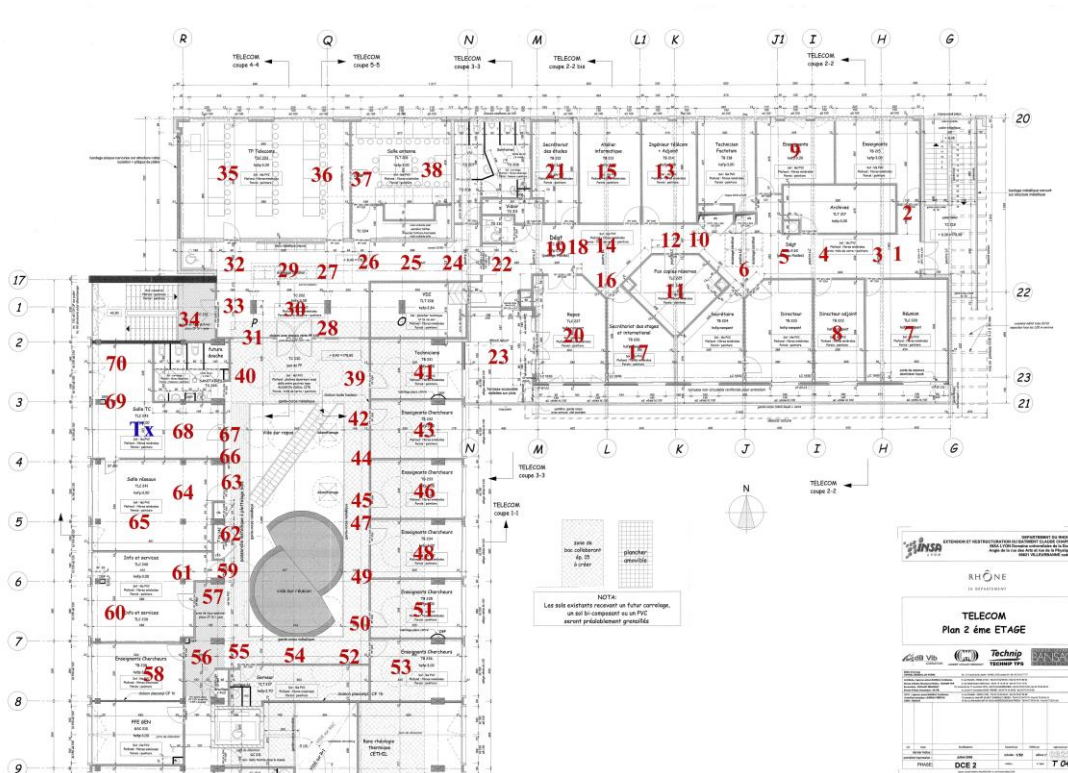


Figure 3.2: The CITI measurement scenario

The measurements were done in the CITI laboratory, INSA-Lyon, France.

The scenario

The scenario is the CITI lab building at INSA-Lyon, France. The location of the transmitter is marked by "Tx" in Fig. 3.2. The numbers in Fig. 3.2 indicate the locations of the receivers. There are totally 70 numbers marked in Fig. 3.2, but the point 41 was not measured due to the closure of the office door. Hence, we finally have 69 measurement points.

Measurement setup

The measurements were done at 3,4 GHz. The transmitter included the arbitrary waveform generator (ESG4438C by Agilent Technology) and the 6 dBi omnidirectional antenna ECO6-3500. The equivalent isotropically radiated power (EIRP) was 20 dBm. The mean powers at the 69 points above were measured with the Handheld Spectrum Analyzer ROHDE & SCHWARZ FSH8 equipped with the omnidirectional antenna ECO6-3500 (see Fig. 4.10). The parameters of the FSH8 were configured as follows: F0 = 3.4 GHz; SPAN = 4.5 MHz; RBW = 300 KHz; SWT = 50 ms, where RBW and SWT denote the resolution bandwidth and the sweep time, respectively.

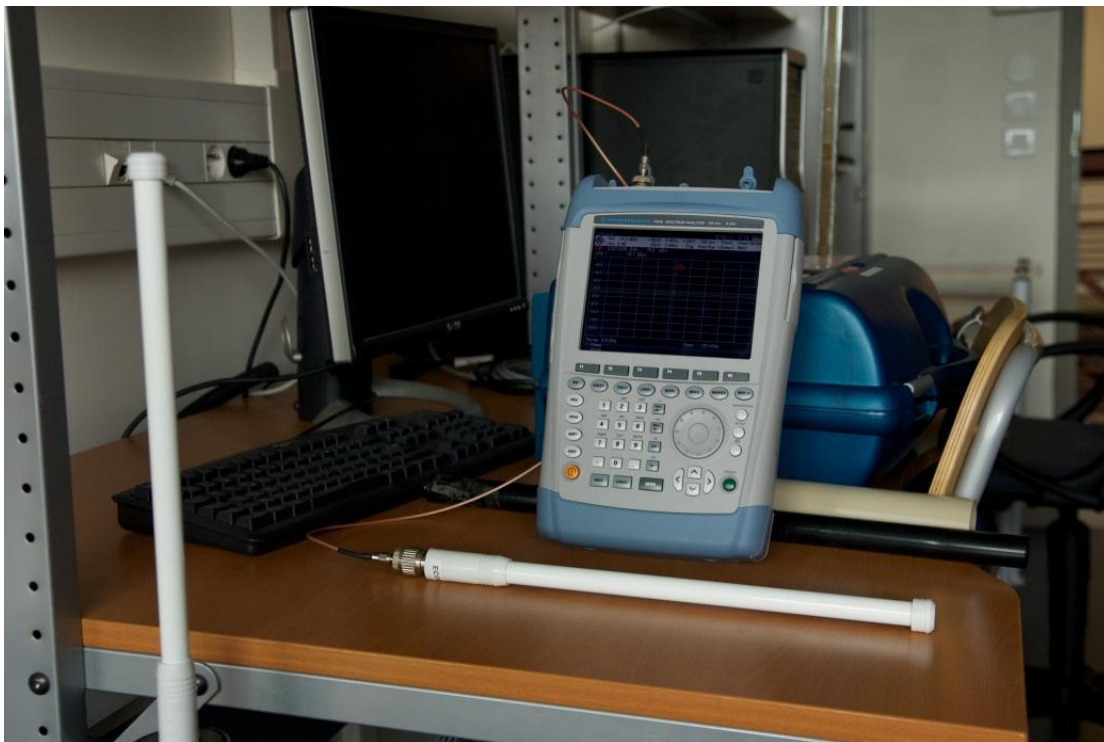


Figure 3.3: The Spectrum Analyzer FSH8 and the omnidirectional antenna ECO6-3500

	air	absorbant	concrete	plaster	wood	glass
n_{mat}	1.0	1.0	5.4444447	1.9444444	1.1666666	1.4166667
a_{mat}	0.9996667	0.9688	1.0	1.0	1.0	1.0

Table 3.1: Parameter values of materials optimized from the calibration

Calibration

The calibration is performed with 12 measurement points: 1, 5, 7, 11, 15, 20, 24, 27, 28, 32, 35, 40. The parameter values of materials optimized from the calibration process are listed in Table. 4.3.

The obtained parameter values are configured to run the MR-FDPF simulations at both 3,4 GHz and 3,5 GHz. And then the offset and the RMSE can be computed from all the 69 measurement points. Fig. 4.11 shows the radio coverage map predicted at 3.5 GHz with the MR-FDPF model as an example.

The offset and the RMSE computed from the 3:4 GHz MR-FDPF simulation are: offset = -43.0176 dB; RMSE = 8.4617 dB; The offset and the RMSE computed from the 3.5 GHz MR-FDPF simulation are: offset = -41.7559 dB; RMSE= 8.5568 dB.

From the above results, we know that it is better to calibrate the simulations at the exact frequency as you want to simulate because the RMSE will be larger if you use the parameter values calibrated at a different frequency to perform the simulations.

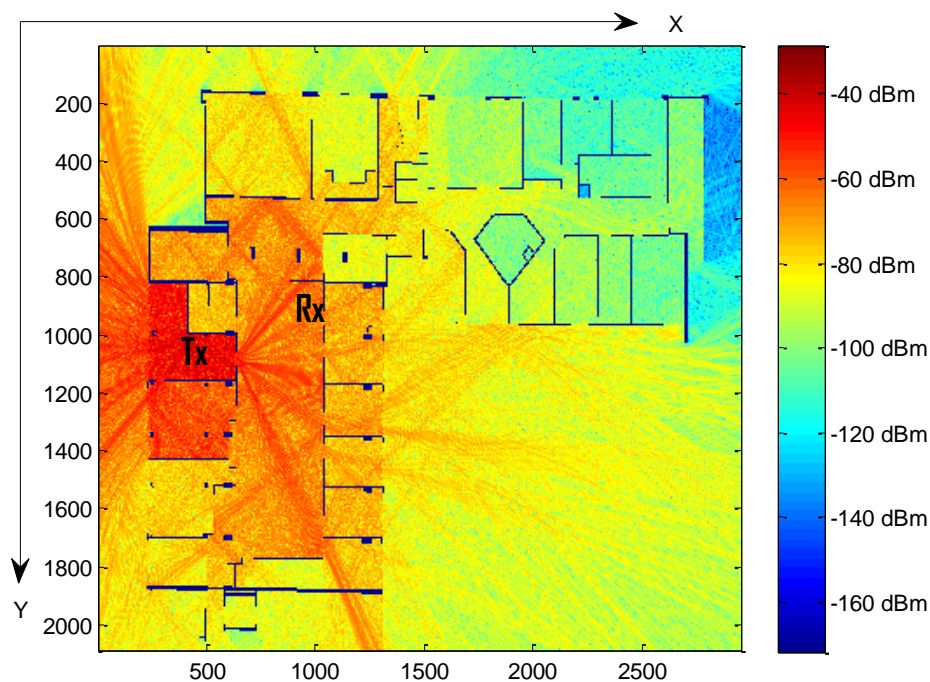


Figure 3.4: The coverage map predicted with the MR-FDPF model.

3.1.4 Scenario and Measurements for outdoor-to-indoor

The scenario for the evaluation of the model is the INSA university campus in Lyon, France (see Fig.3.5). The size of the scenario is 800×560meters. The size of CITI building (surrounded in red in Fig.3.5), where the indoor radio coverage is simulated, is approximately 110 × 100 meters.



Figure 3.5: outdoor to indoor scenario. In red: the building where the indoor measurements were performed. E1 and E2 represent the position of each emitter and the black arrows show the directions where the directive antennas were pointing.

The combined models require working at two scales i.e. an outdoor scale where a database of the buildings without their content is used, and an indoor scale where the details of the building to simulate are taken into consideration.

Hence two databases of the scenario were generated:

- The outdoor database, required by IRLA, was created using Google maps for extracting the shapes of the buildings, and a laser meter to measure the height of each building. Hence it is not a real full 3Ddatabase but a 2.5D database, in a .dat format similar to the one used by commercial RO software. A unique material coefficient was used for all the buildings.
- The indoor database containing all the walls of the floors used by MR-FDPF was generated from the .dxf format architect files. A 2D cut of the floor in the horizontal plane was used. The environment was modeled using 3 different materials for the obstacles: concrete for the main walls, plaster for the internal walls and glass for the windows.

To validate the model, two measurement campaigns at different frequencies and emitters' locations were performed in the same scenario, as detailed in Tab.3.2. The two frequencies chosen for the validation (i.e. 3.5GHz and 2.4GHz) correspond respectively to the frequencies of Worldwide Interoperability for Microwave Access (WiMAX) and Wireless Fidelity (WiFi) in Europe.

	Experiment 1	Experiment 2
Frequency	3.5GHz	2.4GHz
Position on map	E1	E2
Emitting antenna	ETS-Lindgren Horn antenna Model 3115	Stella Doradus Parabolic antenna Model 24 SD21

Table 3.2: Measurement campaign

The directive antennas, simulating sector of external macrocells, located at approximately 3m height, were pointing on CITI building in the directions represented in Fig.2 (represented by arrows).

The equipment for the measurements is based on an Agilent generator ESG4438C and an N9340A Handheld RF Spectrum Analyzer. A total of 104 measurement points were chosen (32 indoors and 72 outdoors). At the receiver's side, omnidirectional antennas were used. Moreover, in order to avoid fading effects, these antennas were slightly moved and the mean value after continuous 20 second measurements was recorded.

Before running the MR-FDPF simulations, IRLA has been calibrated for both measurement campaigns, providing a RMSE of 8dB, which is acceptable considering the arguments given in section 3.3 and also the fact that the points were distributed in the scenarios and some of them far from the building of interest (see Fig.4.b for the location of these points).

Results

As an illustration, the rays and the coverage map computed with IRLA and corresponding to experiment 1 are plotted in Fig.3.6. The simulated signal inside the CITI building based on the new combined model is plotted in Fig.3.7 (Experiment1) and Fig.3.8 (Experiment 2), as well as the comparison between simulation and measurements for the received signals (before calibration of MR-FDPF). It is seen on these figures that the effects of the windows are well taken into account, and that the measurements and simulation are well in accordance.

In order to evaluate the accuracy of the model more in details, the RMSE values are plotted in Tab.3.3, depending on if MR-FDPF is calibrated, and depending on the number of points used for the calibration.

X	Experiment 1	Experiment 2
No calibration	2.80dB	2.28dB
Calibration (4 points)	2.61dB	1.77dB
Calibration (all points)	2.39dB	1.17dB

Table 3.3: Performance of the model: accuracy

It is verified that, even without calibration (default material values for the indoor walls) the model performs well (less than 3dB RMSE which corresponds to the accuracy that MR-FDPF reaches for indoor simulations only [21]).

Moreover, and as expected, calibrating the model using few points (4) improves the accuracy. As an illustration of what is the best possible accuracy the model could reach, the RMSE after calibrating using all the points is also given.

However and as said bellow, the aim of such model is to be used by radio engineers in order to save time due to radio measurement campaigns that is why such calibration using all the points has no practical meaning. Nevertheless it is proven in this experiment that only few measurement points suffice to improve the model and reach a high accuracy (Less than 2dB in the case of WiFi). Finally, let us just notice that in practice it makes no sense to reach lower values of accuracy (typically less than 2dB), since the accuracy of the measurement equipment (even after the small scale fading is removed) may have larger variations.

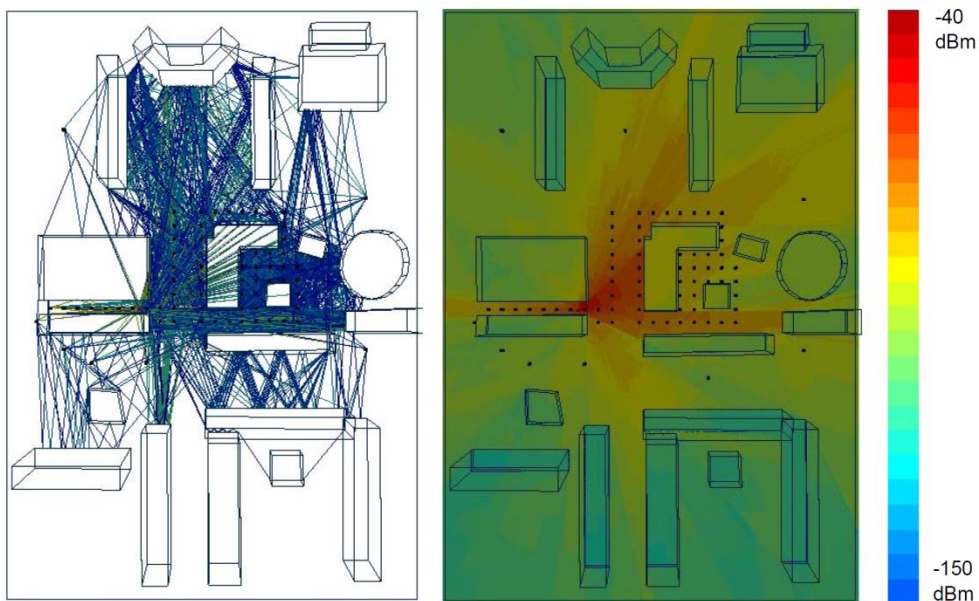


Figure 3.6: IRLA simulation (Experiment 1), left: outdoor rays, right: outdoor coverage map

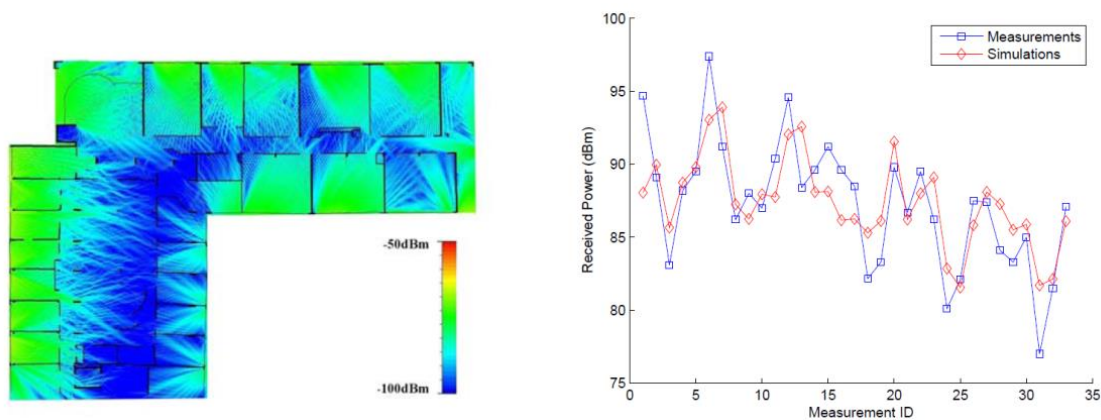


Figure 3.7: Outdoor to Indoor simulation results (Experiment 1)

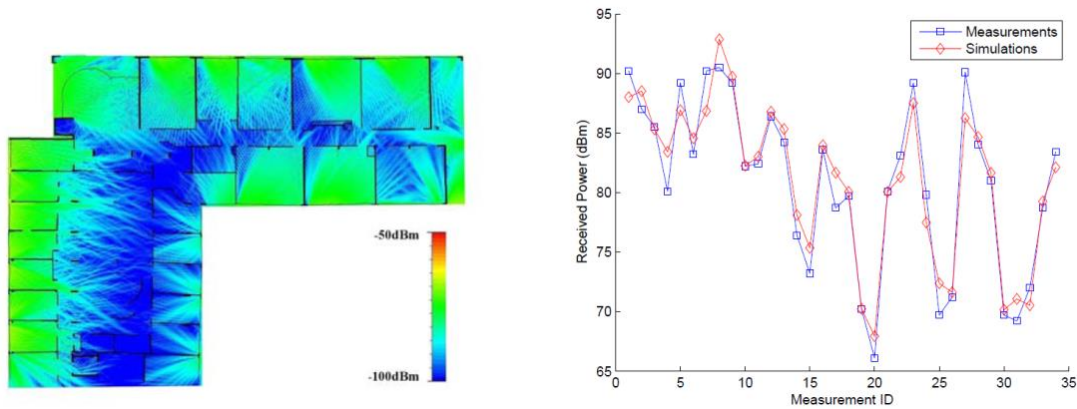


Figure 3.8: Outdoor to Indoor simulation results (Experiment 2)

The time durations of the simulations are given in Tab.3.4 and it is shown that the total simulation time (once the MRFDPF preprocessing has been already done) for one outdoor to indoor prediction is less than 2 minutes on a standard computer. Let us remind here that the preprocessing of MR-FDPF does not need to be run if the walls are not modified, since the ParFlow scattering matrices does not depend on the location of the sources.

X	IRLA	MR-FDPF	Total
Pre-processing	0s	41s	41s
Simulation	58s	57s	115s

Table 3.4: Performance of the model: simulation times (on PC, 2.4GHz, 2Gb RAM).

Advantages of the model

It is important to notice that, without combining MRFDPF with IRLA, it would not have been possible to compute the whole scenario with MR-FDPF only, due to high memory requirements during the preprocessing step. However, by supposing that this amount of memory is large enough, it is then possible to interpolate the simulation time duration it would take for simulating the whole scenario with MR-FDPF. Indeed, and as detailed in [20], the complexity of the propagation phase of MR-FDPF varies in $O(\log_2(N).N^2)$, where N is the smallest dimension of the scenario in pixels. Thus a simulation of the full environment (560 meter large) at the same resolution would be $\log_2(560/100).(560/100)^2 = 78$ times slower, i.e. it would take approximately 2.5 hours instead of less than 2minutes (115s) with the proposed combined model. Furthermore, such simulation would only simulate a 2D cut, where the height of the outdoor emitters would not be properly taken into account; hence it would provide a low accuracy, compared to the approach we use where the outdoor signal effects are simulated in 3D. Consequently, the new model proposed in this study is advantageous both in term of speed and accuracy.

3.1.5 Performance evaluation

The propagation scenario considered in this section is the same as previously: INSA university campus in Lyon, France, already shown in Fig. 3.5.

The size of the environment is 800 by 560 m. Marked in red in Fig. 1 is the CITI building. The CITI building dimensions are approximately 110 by 100 m.

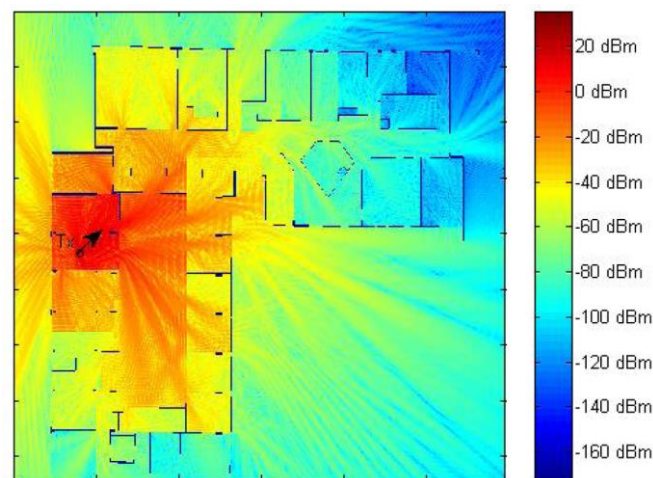
The electrical field strength $E(r, f)$ inside the CITI building and its immediate surroundings has been computed with a spatial resolution of 5 cm in the frequency band $B = 60$ MHz.

The power of the electrical field obtained by the MR-FDPF method at the central frequency $f = 3,5$ GHz is shown in Fig. 3.9.

The electrical field at every 40 cm (8 times 5 cm) interval located at 2 m outside the walls around the CITI building is modeled by the sum (2) of $N = 20$ plane waves propagating from the inside of the CITI building. Note that the choice of the number N of the plane waves in (2) is mainly dictated by the trade-off between the prediction accuracy and the computational load associated with estimating the parameters

of the plane waves. The useful parameters for each of the intervals are estimated by using the SAGE algorithm. The estimated amplitudes and the propagation directions in the horizontal plane defined by the estimated wave vectors are then supplied to the intelligent ray launching algorithm (IRLA) [12].

The rays constructed based on the estimated parameters for the considered propagation scenario are visualized in Fig. 3.10. The coverage map computed with the IRLA for the outdoor environment is



depicted in Fig. 3.11.

Figure 3.9: The predicted indoor radio coverage

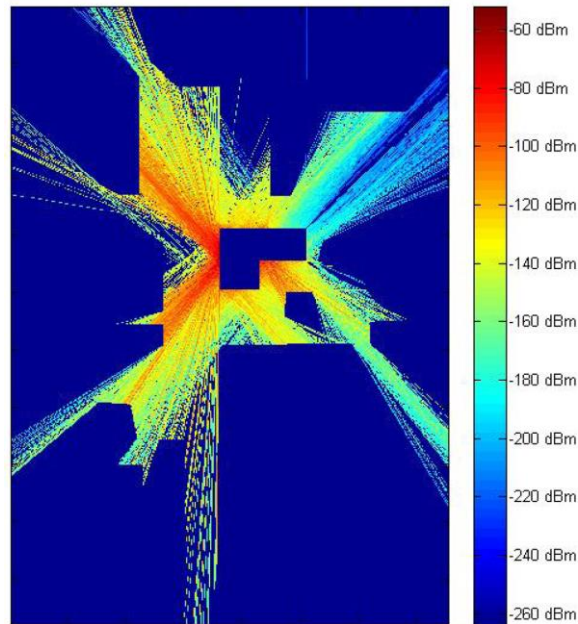


Figure 3.10: Rays constructed based on the indoor radio coverage prediction.

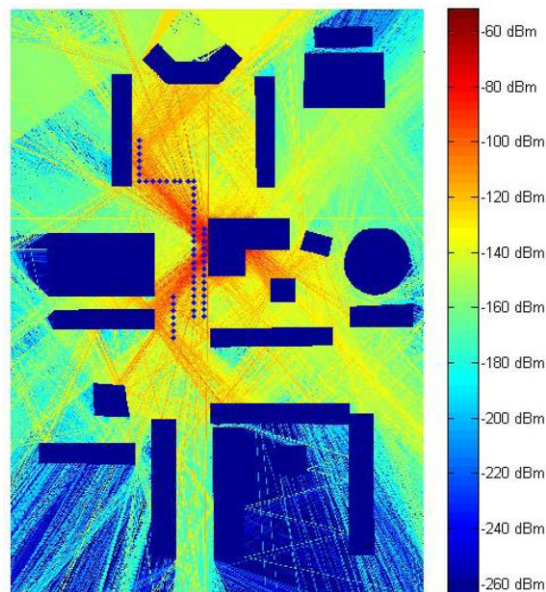


Figure 3.11: The predicted outdoor radio coverage.

In order to evaluate the performance of the new combined model a measurement campaign has been carried out. A transmitter equipped with a directive antenna has been deployed inside the CITI building. The transmitting antenna has been located approximately 10 m above the ground. The position of the transmitter (Tx) and the orientation of transmitting antenna's diagram are depicted in Fig. 3.9. Radio measurements have been performed at the locations marked with the dots in Fig.3.11. The omnidirectional antenna has been used at the receiver. The height of the receiving antenna is approximately 1.5 m. To reduce the effect of uncertainties inherent in the modeling and measurement processes, the calibration of the IRLA has been conducted. It is to be noticed that, due

to restricted details in the outdoor buildings database, all the buildings have been modeled using the same unique material.

Hence, during the calibration process, the path loss coefficients for reflection and diffraction for both LOS and NLOS cases have been optimized. The approach is based on a hill climbing algorithm whose cost function to minimize is the root mean square error (RMSE) between the measurements and the simulations. In order to avoid the algorithm stopping in a local minimum, a random change of parameters is regularly performed.

In Fig. 3.12 the comparison between the measurements and simulation results (after calibration) is plotted. A relatively large discrepancy between the simulation results and the measurements observed in Fig. 3.12 can partly be explained by the fact that the transmitting and the receiving antennas have been positioned at different heights. The question of antenna height compensation for the indoor-to-outdoor model will be considered in the following works.

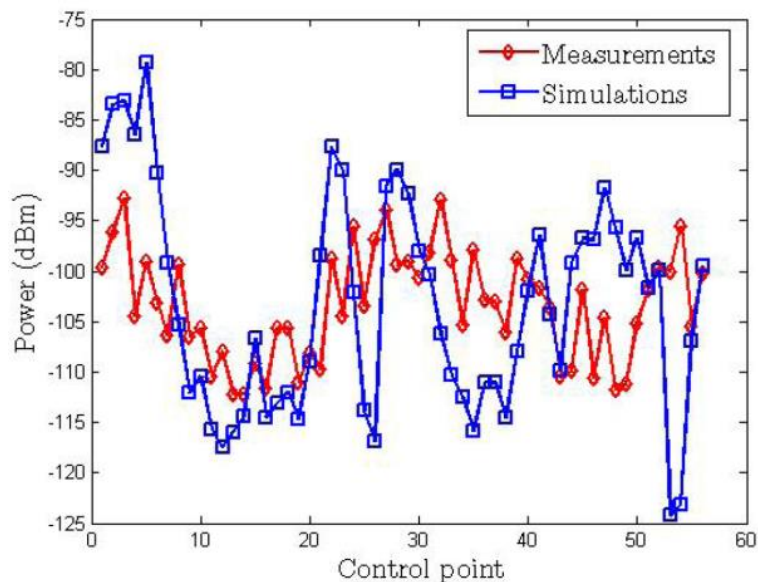


Figure 3.12: Comparison between measurements and simulation results.

3.2 Channel Sounding

For the validation of the coverage prediction software tool it was implemented an instrument setup to estimate the channel that will be described below.

3.2.1 The channel sounder and results

This system consist in a SISO wireless transmitter-receiver with BPSK modulation which was chosen because it is a robust and simple modulation and the availability of well-studied PN sequences with good autocorrelation properties for it. The signal source is the vector signal generator Agilent E4438C. The transmitting chain could be seen in 3.13. The carrier frequency is 3.5GHz (WIMAX) with 12dBm of power signal level which is near the maximum allowed by the generator. It is used the Maximal Length Sequence of order 15 that is available in the generator. The sequence is filtered at emitter with a RRC with $\alpha=0.35$. For a good channel estimation time resolution it is used the symbol or bit rate near the maximum sampling time of the baseband ADC of the receiver (46Mbits/sec). The

receiver is the Agilent VSA with principal modules 89605B and E1439C. The first is the bandpass Receiver and the later is the ADC module. Both sides are connected each one to an omnidirectional antenna with 6dBi gain. The Baseband sampled signal at the receiver is processed by Matlab Scripts. The receiving chain is shown at 3.14.

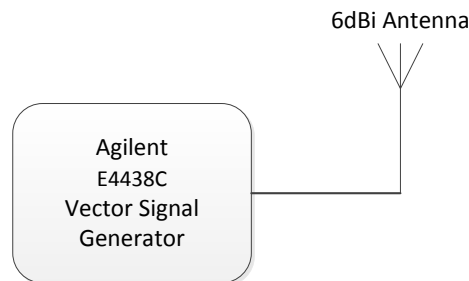


Figure 3.13 Transmitter end for the Setup of Channel Estimation

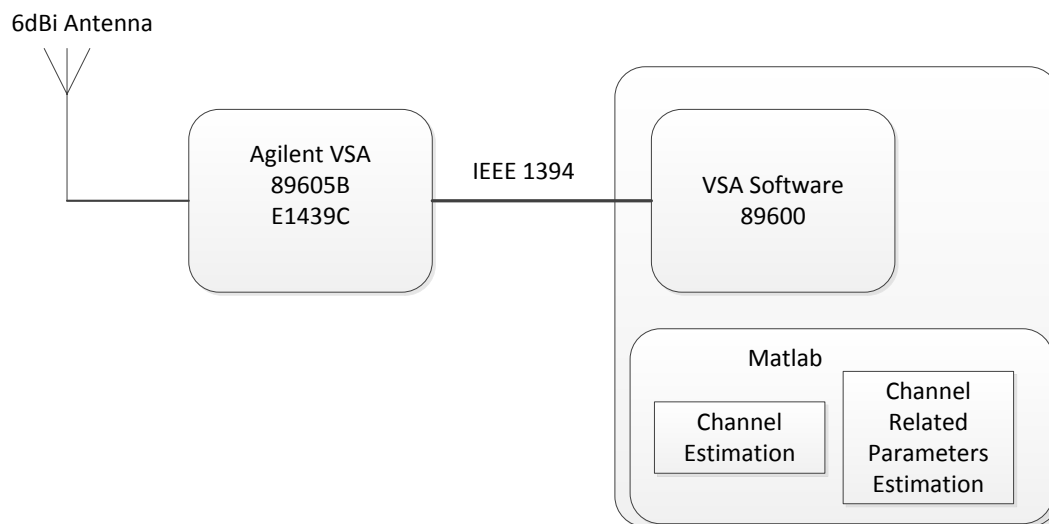


Figure 3.14 Receiver end for the Setup of Channel Estimation

3.2.3 Measurement results

We first present here some sample examples of the time-domain analysis that we can extract from this channel sounder. CIR (Channel Impulse Response), PDP (Power Delay Profile), evolution of the PDP over time, and therefore time of coherence and coherence bandwidth can be obtained. A more detailed discussion about these results will be provided in part 4.1.3.

It could be seen some of the generated graphics in Figure 3.15, 3.16, Figure 3.17. The Matlab Scripts also give parameters like the RMS Delay of the Channel, Maximum Delay of the Channel and Coherence Bandwidth of the Channel. The channel estimation method is through crosscorrelation between the received sequence (with noise) and the transmitted sequence. Figure 3.18 shows the very good stability of the power measurements during the data acquisition.

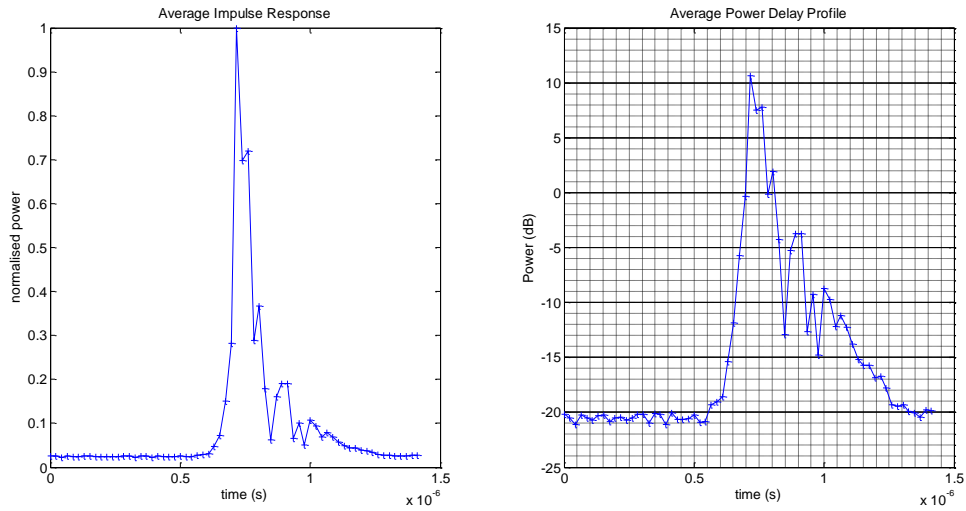


Figure 3.15 Channel Impulse Response (left) and Power Delay Profile (right) example.

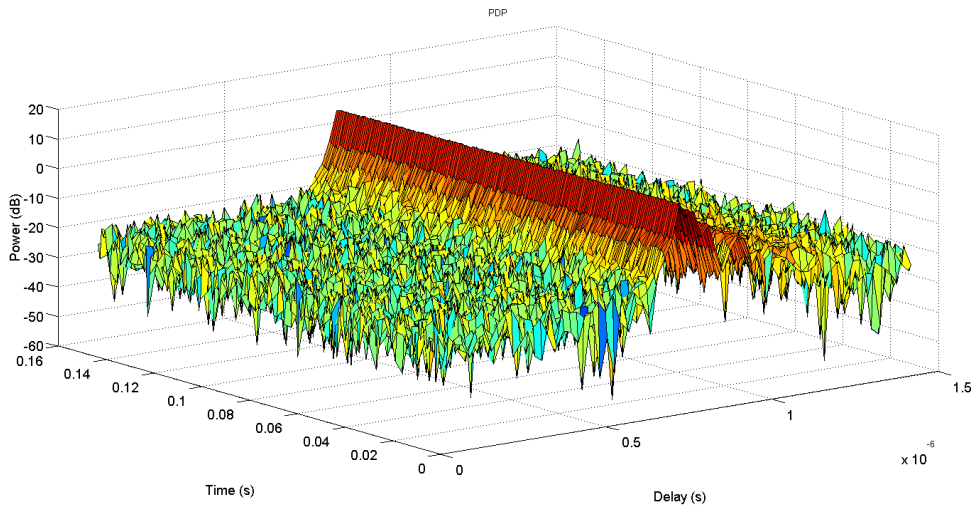


Figure 3.16 Consecutive estimates of the channel through time.

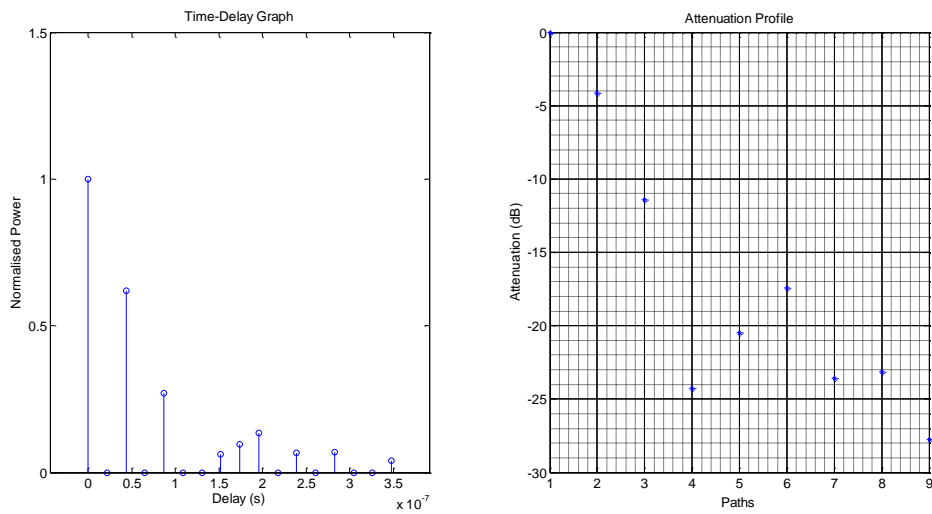


Figure 3.17 Discretized Channel Profile

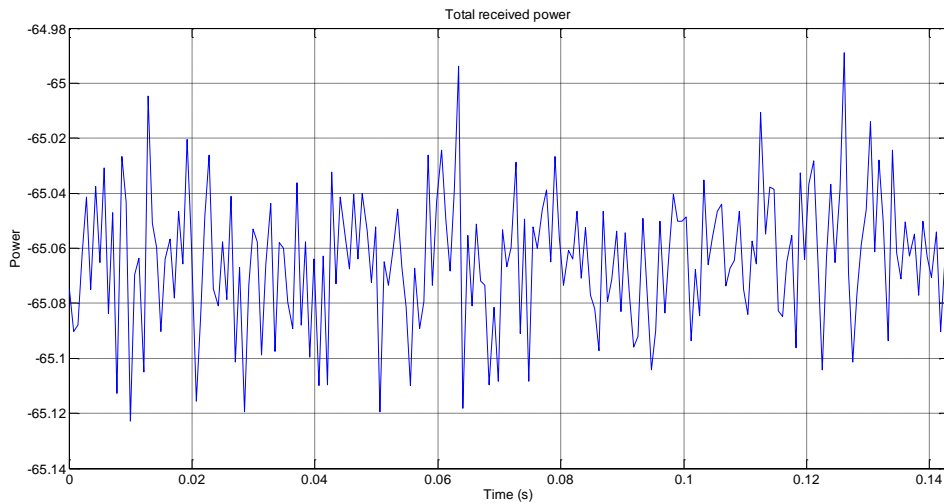


Figure 3.18 Power variation through time.

Large scale channel sounding

A large scale measurement campaign was done at the second floor of the CITI Laboratory at INSA in Lyon. The channel was sounded by a probing signal at carrier frequency of 3.5GHz, BPSK modulated by a train of pulses shaped by a PN15 sequence. The Rx antenna height was 0.88m and the TX antenna height 1.433m.

The measures were carried out with the Tx antenna vertically and horizontally polarized. The blueprint of the floor is shown in the next figures.

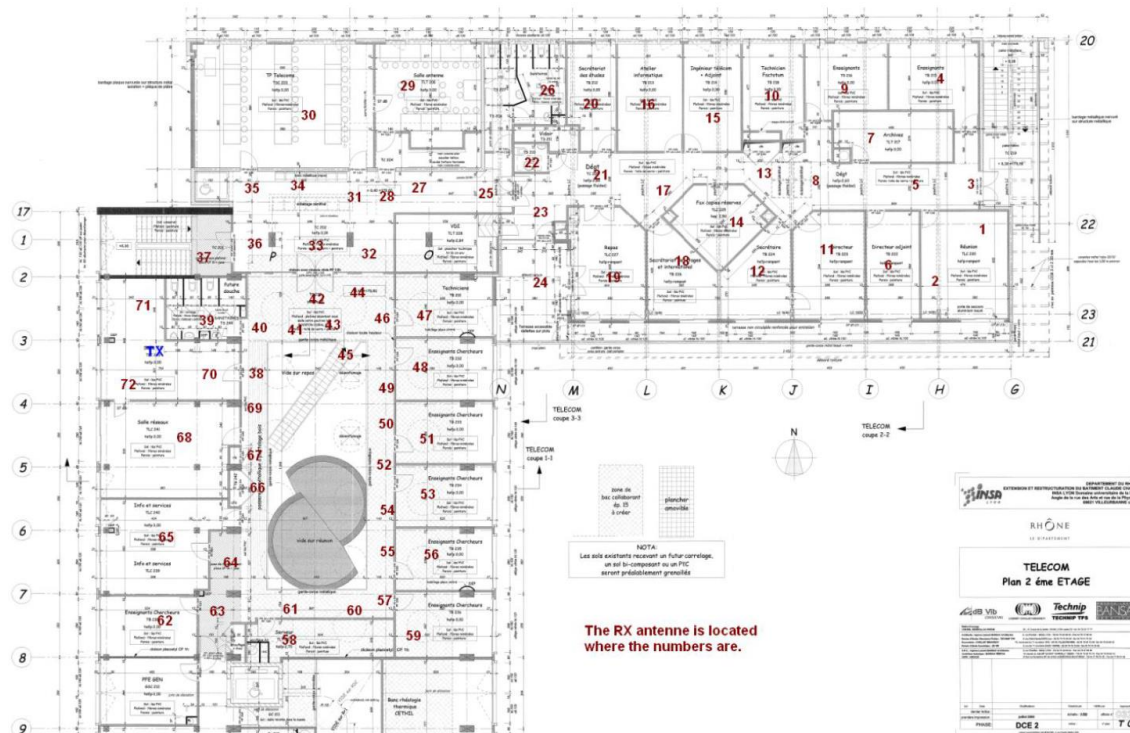


Figure 3.19 Floor blueprint where the measurements were made. Vertical polarization of the Tx antenna.

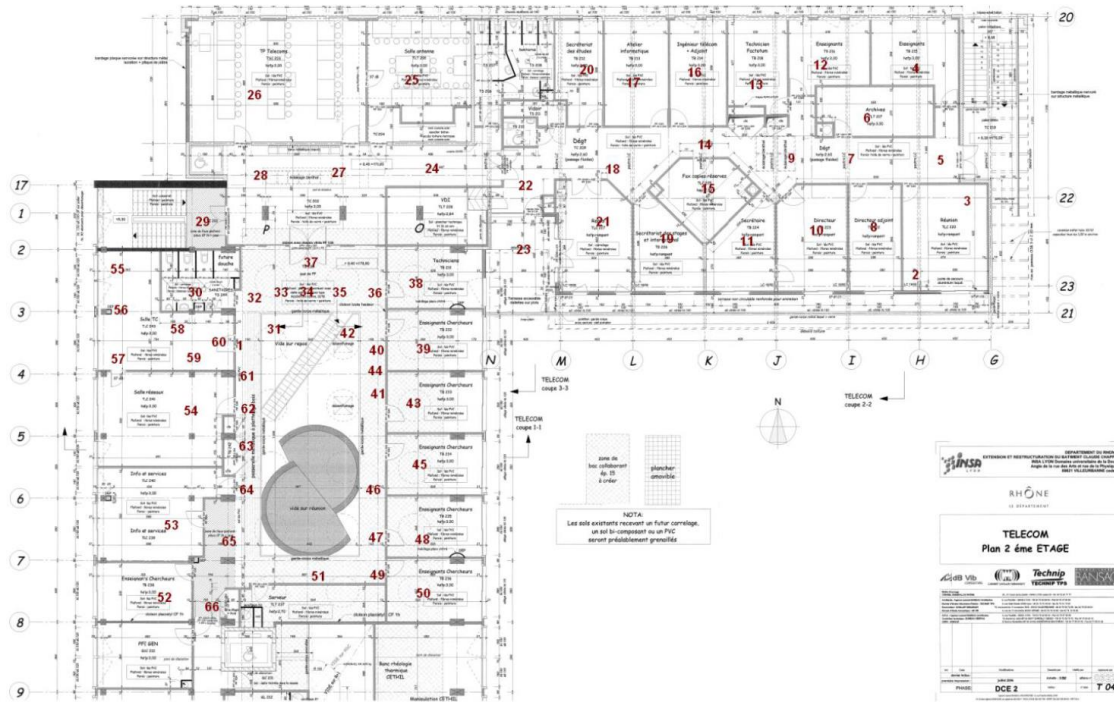


Figure 3.20 Floor blueprint where the measurements were made. Horizontal polarization of the Tx antenna.

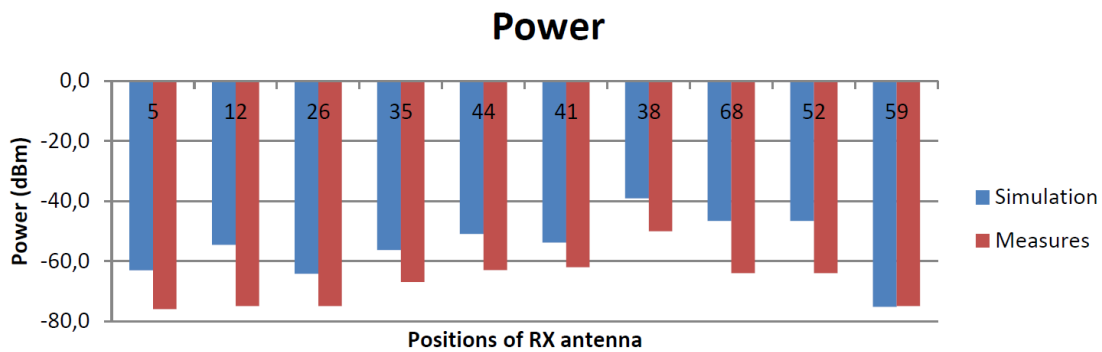
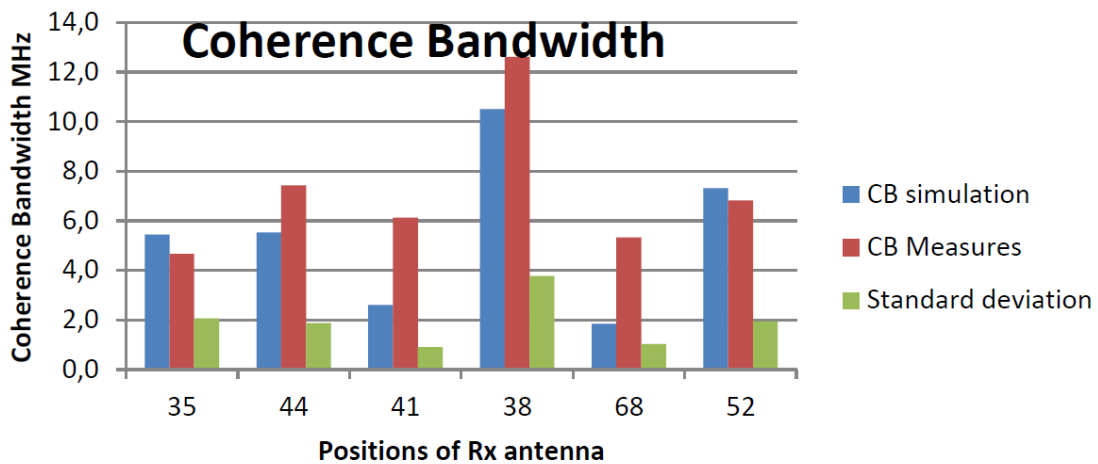


Figure 3.21 Mean power comparison between simulation and measurements.



3.22 Coherence bandwidth comparison between simulation and measurements.

Figure

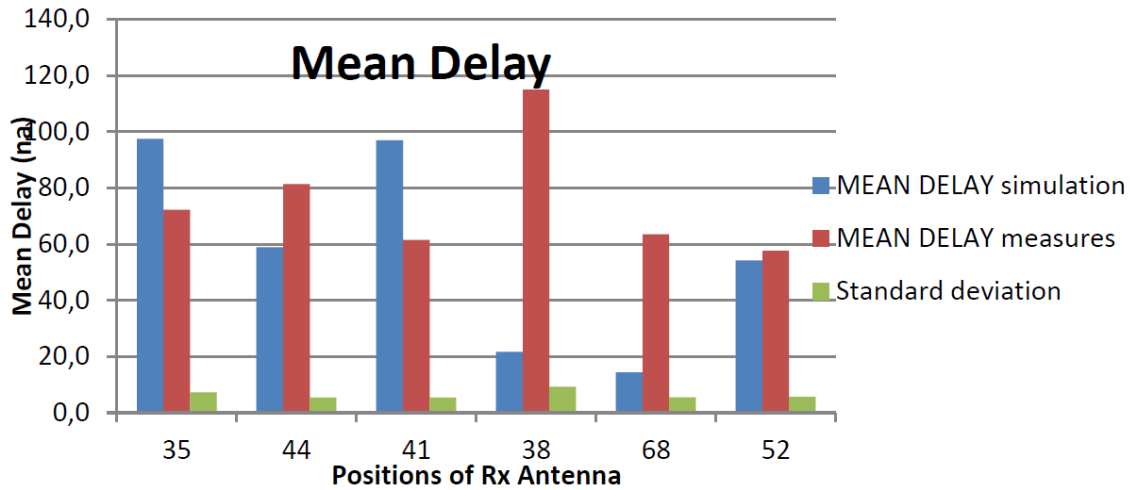


Figure 3.23 Mean delay comparison between simulation and measurements.

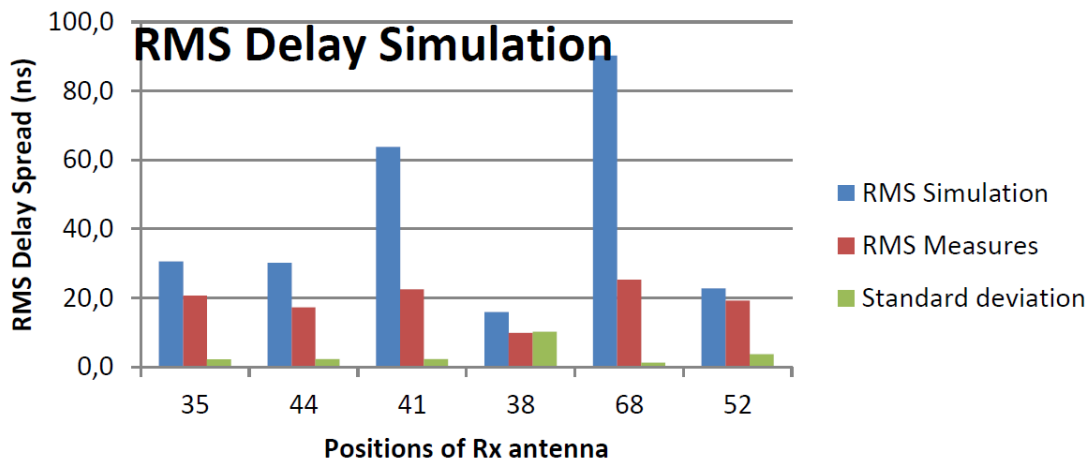


Figure 3.24 RMS delay comparison between simulation and measurements.

The results of the simulation are not exactly the result of the measurements but the order of the values is well approximated. There is not an interval of confidence from the simulator because it uses a deterministic method. The empirical method of the measurements allowed calculating the standard deviation for each channel parameter. For 50 impulses responses the standard deviation in most of the cases was very small and acceptable. The excess delay wasn't a parameter to have in consideration here because the only reference that exists to differentiate each sequence is the principal path, from the impulse response we don't know exactly where the paths of the beginning and the ending of the data are.

The difference between the simulation and measures results could be caused by:

- The simulator has not in consideration the furniture, tools, wireless devices, people walking in the lab, open or close doors.
- The simulator was calibrated from one measurement in the mentioned positions. But the real wireless channel has a random behavior therefore the calibration is also random.
- 50 impulses responses gave a small standard deviation, maybe more records are necessary.

- The instantaneous power measured was an average of the power spectrum taken from the spectrum analyzer.
- The height and angle of the antennas for the simulator are not exactly the same as in real experiment.

3.3 Modulated signals: BER calculation

The objective of the BER computation setup is to measure the performance of a real transmitter-receiver wireless system. The final aim is to validate a coverage prediction software tool. Some technical solutions will not be present in real systems as the availability of the Transmitted Symbol Sequence in the reception. That sequence is used when it knowledge do not influence the performance of the system under study. One good example is it use in part as pilot symbols or to do the BER computation at the end.

3.3.1 Setup for BER calculation

A setup was developed with a transmitter and a receiver to make the estimation of the BER. The central frequency was an unused one (WIMAX) 3.5GHz. The symbol rate was 3.5 MSymbols/s. With that Symbol Rate and with the Indoor Scenario of the CITI building the channel is flat and if there is movement, with fading. The transmitter is the Rohde & Swartz SMBV100A Radio Frequency generator with ARB function which is programmed with Agilent ADS. The transmitter antenna is omnidirectional with 6dBi gain. The transmitted bit sequence chosen was the Maximal Length Sequence of order 23 (Length= $2^{23}-1$). This bit sequence is repeated by the modulation order and modulated to form the transmitted Symbol Sequence also with length $2^{23}-1$. In case of longer acquisitions which happens in most of times this transmitted Symbol Sequence with length $2^{23}-1$ is repeated. The receiver antenna is equal to the transmitter one. The receiver is the Agilent VSA with principal modules 89605B and E1439C. The first is the bandpass Receiver and the later is the ADC module. At the receiver the raw Complex Baseband Signal is sampled with all impairments within because the VSA Software (that does impairment compensation) does not supply the raw bits as output in enough number. It is also doubt that it can supply reliably without solving the phase ambiguity of the modulation which only could be done transmitting pilot symbols. Thus, It was implemented an impairment compensation chain to find out the BER from the received sampled Complex Baseband Signal. The Bit Sequence is imputed in the QAM modulator and then imputed in a RRC FIR. The resulting sequence is the Baseband Transmitted signal which is ARB programmed over LAN on the R&S SMBV100A Vector Signal Generator. This only is needed to be done one time for each Modulation setting change.

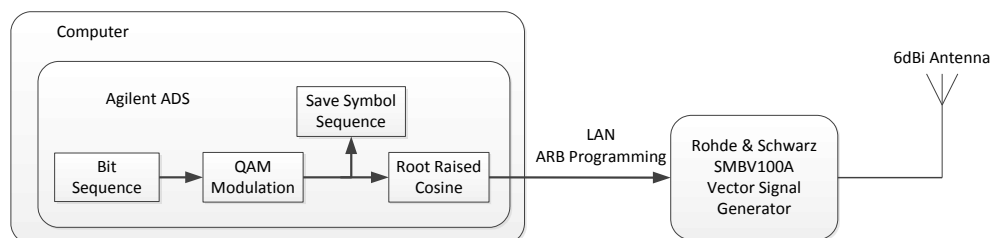


Figure 3.25 Transmitter Chain. The ARB Programming over LAN only needs to be done one time for each QAM Modulation setting change.

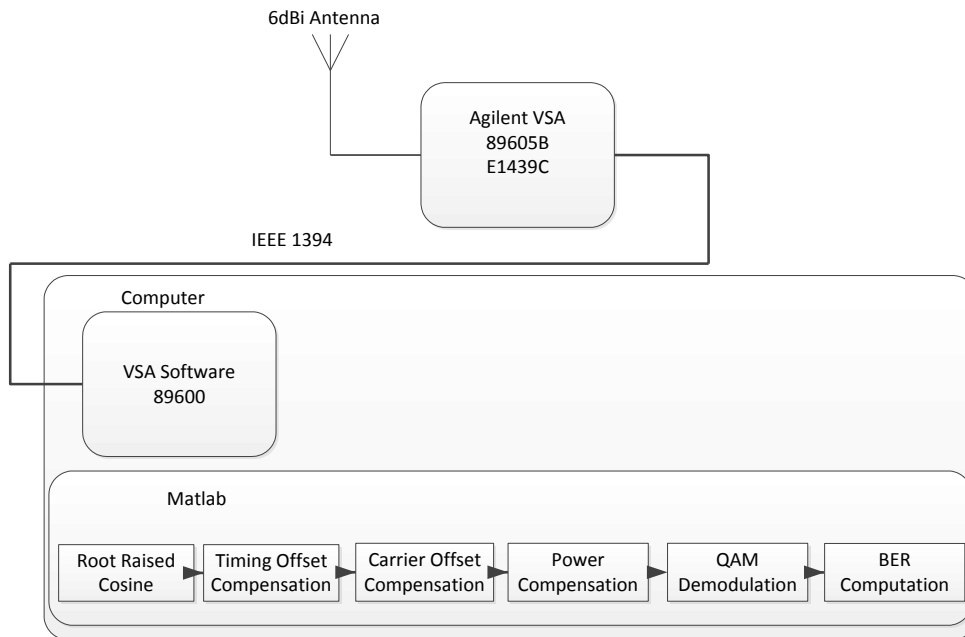


Figure 3.26 Receiver Chain. The Matlab program is run offline.

Figure presents the receiving chain. The raw Baseband signal is acquired by the E1439 VSA module with a sample rate multiple of the symbol rate and transferred to a computer through an IEEE 1394 connection. Then the acquired signal is offline compensated for impairments as:

1. Timing Offset Compensation – The sampled signal is compensated for the small mismatch between the symbol frequency in the transmitter and the receiver. Also the instantaneous time phase offset is compensated. Small but it could represent several symbols at the end of the sequence and so an unsynchronized sequence.
2. Carrier Offset Compensation – This includes the compensation for the difference of frequency (frequency offset) of the carrier at transmission and at the receiver local oscillator (minus the Intermediate Frequency). This is reflected in the sampled complex signal as a linear phase evolution (relative phase to the transmitted symbol sequence). Also it is compensated the small variations of frequency around the frequency offset.
3. Power Compensation – The signal is Power Compensated such the final power of the signal is the nearest to the power of one plus the noise power. That is done with the aid of pilot symbols.

3.3.2 Description of the Receiver Compensation Chain

The measurement example presented will be for a high E_b / N_0 because it is case that it is more difficult to reach match between theory and measurement.

The first block, implemented through a Matlab Script, of the offline Compensation Chain is the Root Raised Cosine whose parameter is $\alpha=0.35$. This block uses the Overlap-Add algorithm to implement the RRC FIR.

The second block is Timing Offset Compensation one. This block (Matlab Script) is based the Matlab function Early-Late Gate Timing Offset Compensation. The function has as one output the Timing Phase (in samples) which is used by the script to shift the sequence accordingly to maintain it (the timing phase) in a certain range. In case of a shift of the sequence and so a timing offset step, it is taken in account the memory of the compensation iterative algorithm. It was experimented with a

baseband symbol upsample of 3, 4 and 8 and only the later upsample is adequate taking in account the interpolator precision inside the timing phase compensation Matlab function. For a symbol upsample of 8 and a symbol rate of 3.5M the maximum acquisition time is 8.5 seconds. Figure presents the Timing Phase Evolution during compensation.

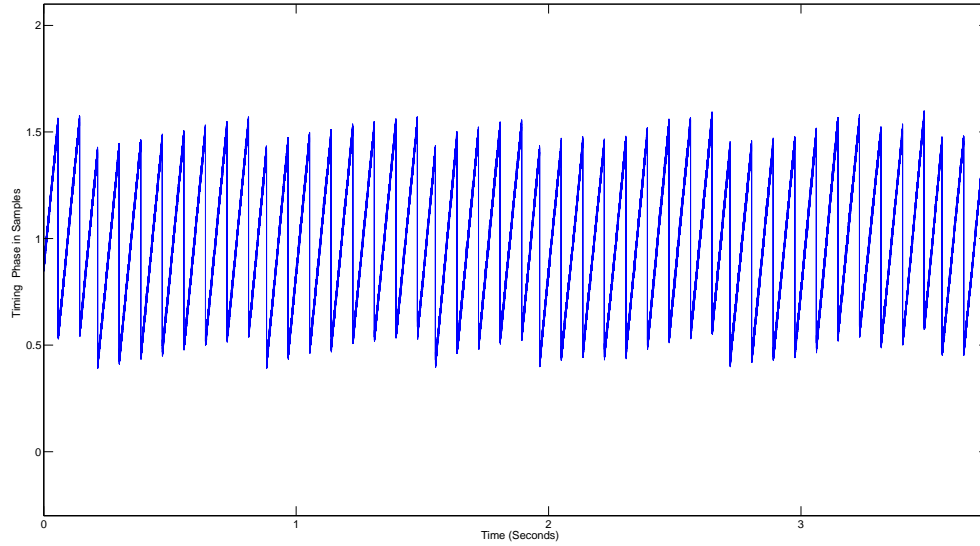


Figure 3.27 Evolution of the Timing Phase in Samples with the range limited.

The next block is the Carrier Frequency Offset Compensation. The frequency offset is computed from the slope of wave determined with Eq. 3.2 which gives information about the phase of the symbols. $r(k)$ (with k taken 128 values) are the symbols that must be computed the phase from. The result is a Saw alike discrete wave with values from $-\pi/4$ to $\pi/4$. If it is summed multiples of $-\pi/2$ or $\pi/2$ in such a way the wave has no steps. From the slope of this wave it can be taken the frequency offset. Must be referred that the phase found with **Erreur ! Source du renvoi introuvable.** is not the absolute phase because it has a phase modulation ambiguity. If the true phase is between $-\pi/4$ and $\pi/4$, Eq. 3.2 gives the right result. If the true phase is outside that range, the phase given by Eq. 3.2 is the true phase rotated by a multiple of $\pi/2$.

$$\hat{\theta}_{Blind} = \frac{1}{4} \arg \left(\sum_k [r(k)]^4 \right) \quad (3.2)$$

The k must take values of a set of dimension the modulation alphabet size or multiple of that.

A second script does a narrow search of the carrier frequency offset, around the offset frequency found with Eq. 3.2 [1] [2]. The objective is to find the relative time phase between the time offset compensated symbol sequence and transmitted symbol sequence and obtain the reference for relative phase graphs, noise graphs and BER computation. The operation between brackets of Eq. 3.3 is the spectrum of the cross correlation between $r(n)$ and $s(n)$.

$$\hat{\nu}_{off} = \arg \max_{\tilde{\nu}} \left(\sum_{n=0}^{N-1} r(n) s^*(n-\tau)_N e^{-2\pi n \tilde{\nu} / N} \right), \quad \tau \in \{0, \dots, N-1\} \quad (3.3)$$

$r(n)$ is the time offset compensated symbol sequence, $s(n)$ is the transmitted symbol sequence and $N = 2^{23} - 1$. The length of the transmitting sequence has little influence in the time of execution and none in the performance of the chain. The search is made in discrete Frequency Domain and for each $\tilde{\nu}$ is done an inverse DFT to find the maximum. The delay in symbols of the maximum determines the relative phase of $r(n)$ and $s(n)$. Fig. 3.28 shows the result of the operation between brackets of Eq. 3.3 for the frequency offset searched.

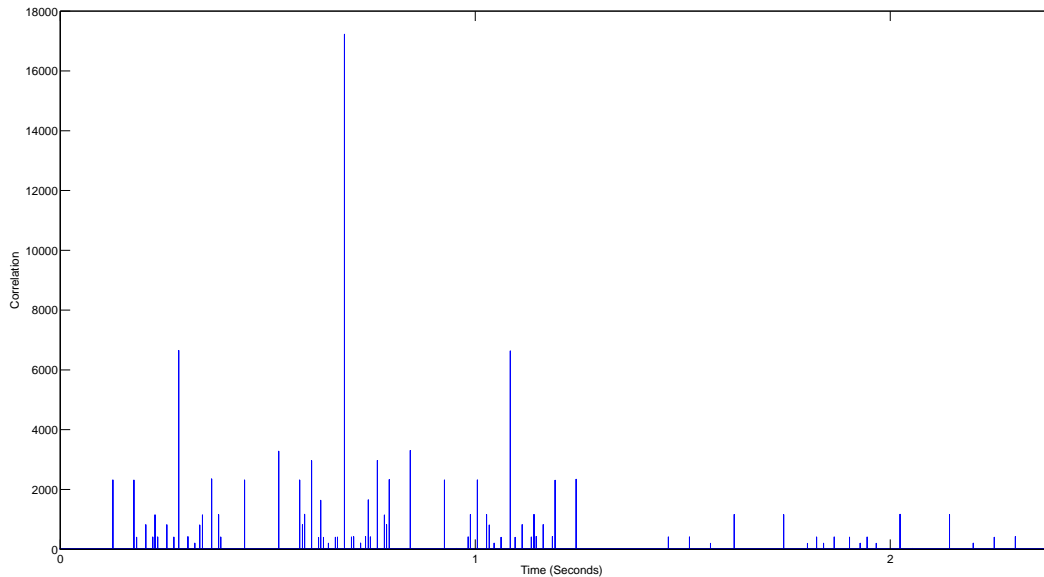


Figure 3.28 Example of correlation between the transmitted sequence and the timing offset compensated one.

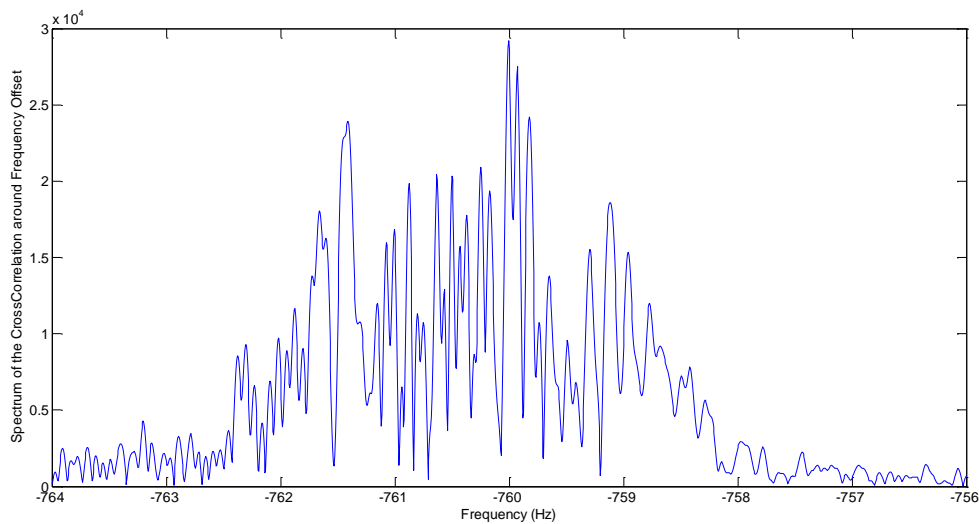


Figure 3.29 Spectrum of the Cross Correlation between synchronized transmitted sequence and Timing Offset Compensated one around Frequency Offset.

Fig. 3.29 shows the Spectrum of the Cross Correlation between synchronized transmitted sequence and Timing Offset Compensated one around Frequency Offset. This is not a Figure provided by the chain and it is from a longer acquisition. The frequency resolution is improved due a lower frequency step and longer time window ($N > 2^{23} - 1$). The carrier frequency power is spread due to clocks

shifts and it due also to Doppler shift if there is movement. Because the frequency offset is not a tone, after central (in terms of slope of the phase progress given by Eq. 3.2) frequency offset compensation it remains a fine frequency and phase offset to be compensated. It can be seen in Fig. 3.30 the remained frequency and phase offset.

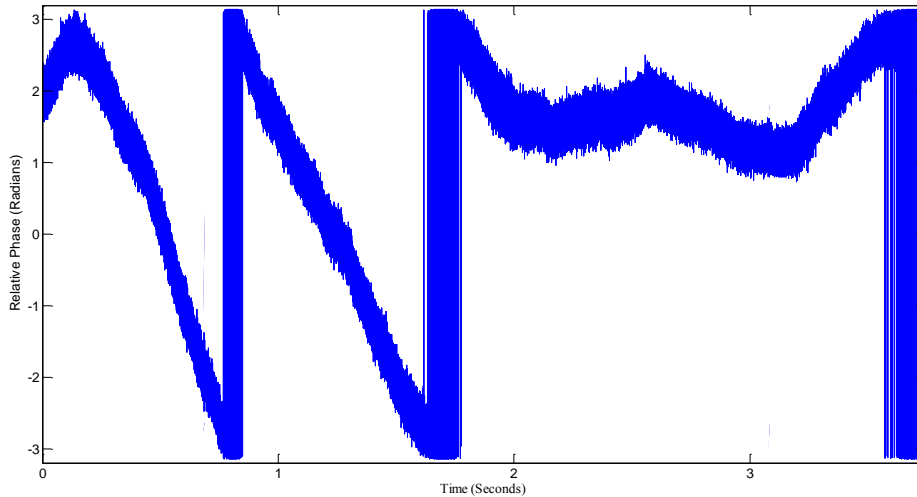


Figure 3.30 Relative phase to the transmitted sequence after central Frequency Offset compensation.

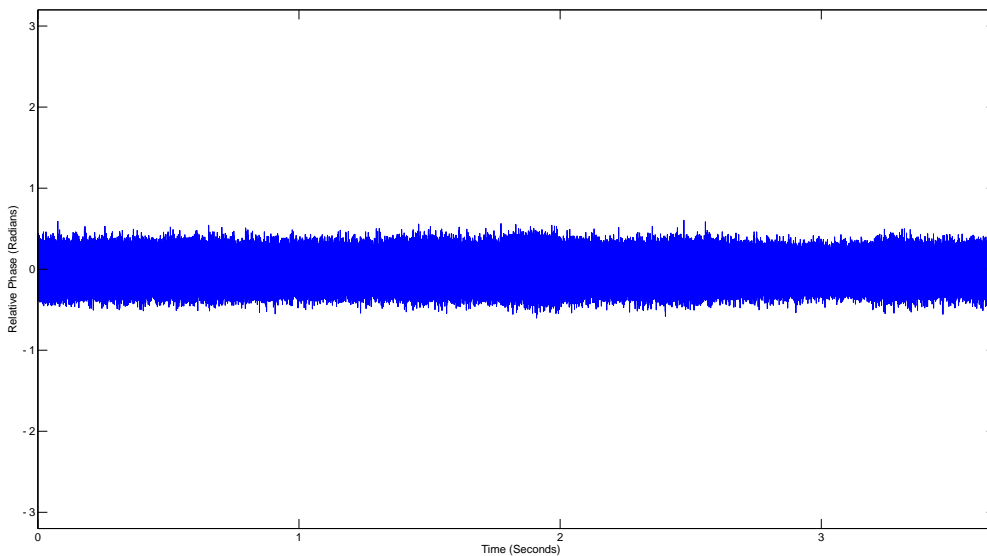


Figure 3.31 Relative phase to the transmitted sequence after Fine Frequency Offset compensation.

For Fine Frequency Offset Compensation the sequence is partitioned in bursts whose size is configurable. In each burst, the phase ambiguity is solved by the use of part of the transmitted sequence as pilot symbols and by Eq. 3.4 [2]

$$\hat{\theta} = \arg \left\{ \sum_{\{k\} \subset \{0, \dots, N-1\}} r(k) s^*(k) \right\} \quad (3.4)$$

$r(k)$ is the received sequence burst after previous compensations and $s(k)$ is the transmitted symbol sequence burst, N the burst size. The angle given by Eq. 3.4 is subtracted from the burst

symbols phases. Next, the phase progress in each burst is determined. That phase progress was approximated to a line by the least squares and subtracted to the original phase. After done to all the bursts the resulting relative phase is shown in Fig. 3.31.

The next block in the chain is the power compensation. It can be seen the power of the uncompensated power sequence in Figure . It can be noticed the fading due to movement.

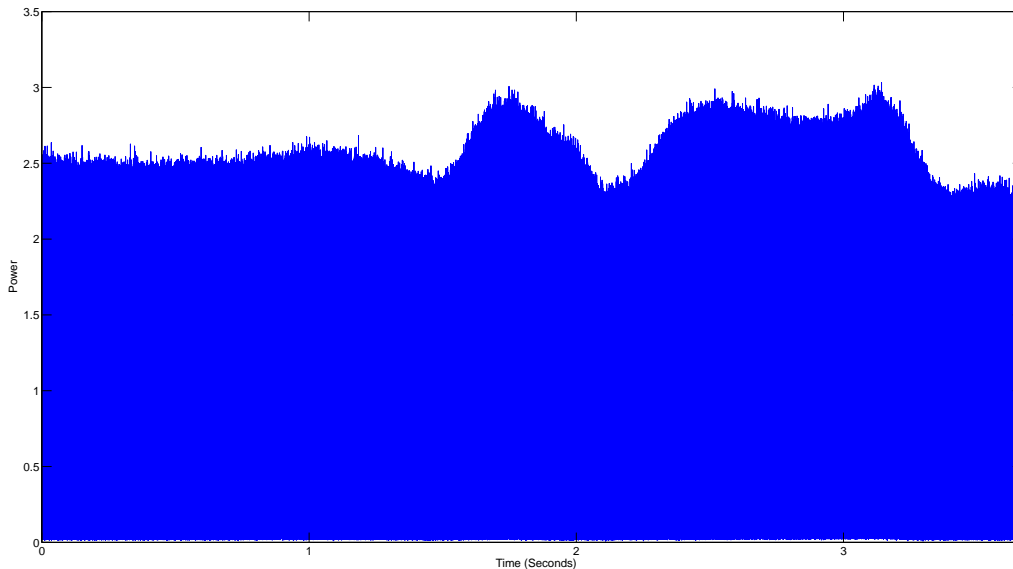


Figure 3.32 Power of the uncompensated power sequence.

The sequence is partitioned again in bursts whose size is configurable. From a subset of transmitted sequence is taken pilot symbols to determine the power and from the received sequence also. The number of pilot symbols is configurable and are a subset of the burst symbols. Then the all burst is power compensated such as

$$NF = \sqrt{\frac{P_t + P_d}{P_r}} \quad (3.5)$$

NF is the normalization factor, P_t is the average power of the transmitted pilots P_r is the average power of the receiving pilots and P_d is the average power of the disturbance of the pilots. The NF is found iteratively because P_d it is not known at first. Fig. 3.33 shows the power of the power compensated sequence. Fig. 3.34 shows the power of the power of the disturbance or noise. Fig. 3.35 shows the constellation of the first compensated 100000 symbols.

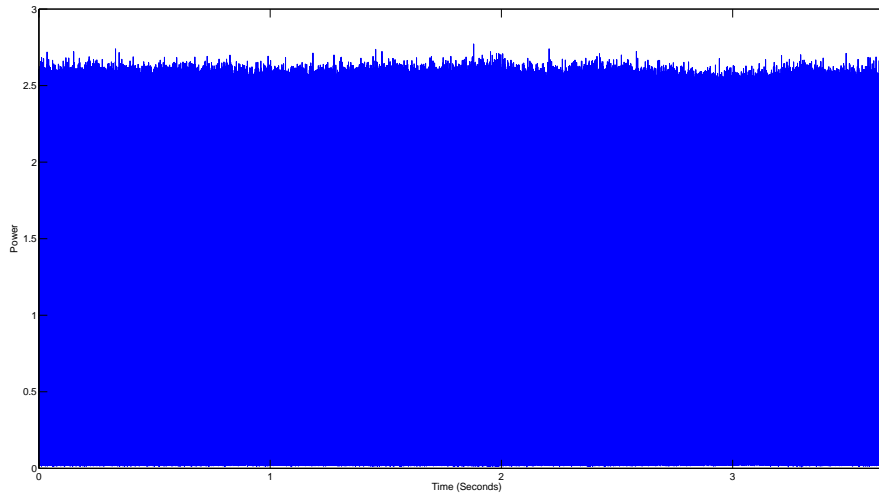


Figure 3.33 Power of the Power Compensated Sequence.

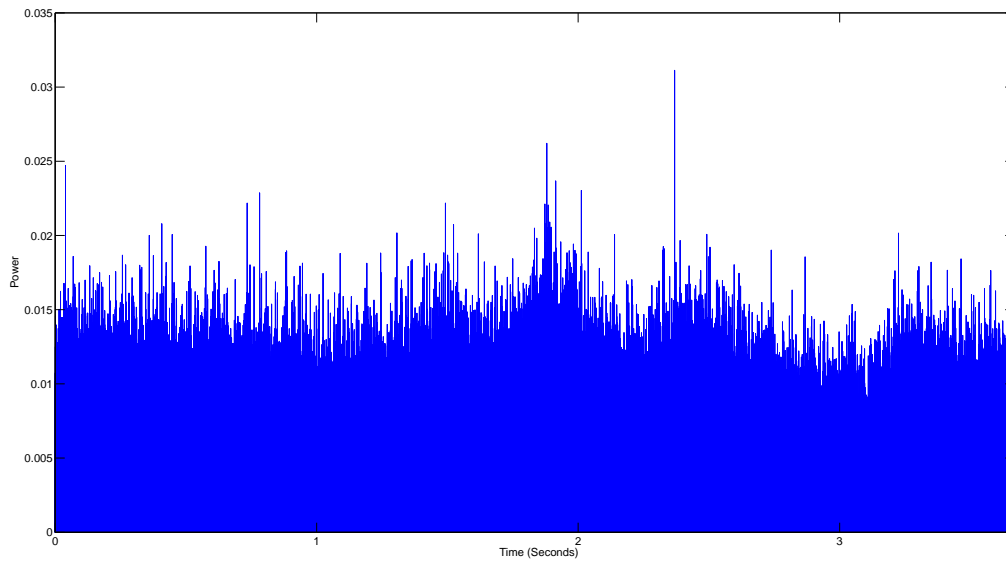


Figure 3.34 Power of Noise of the Power Compensated Sequence.

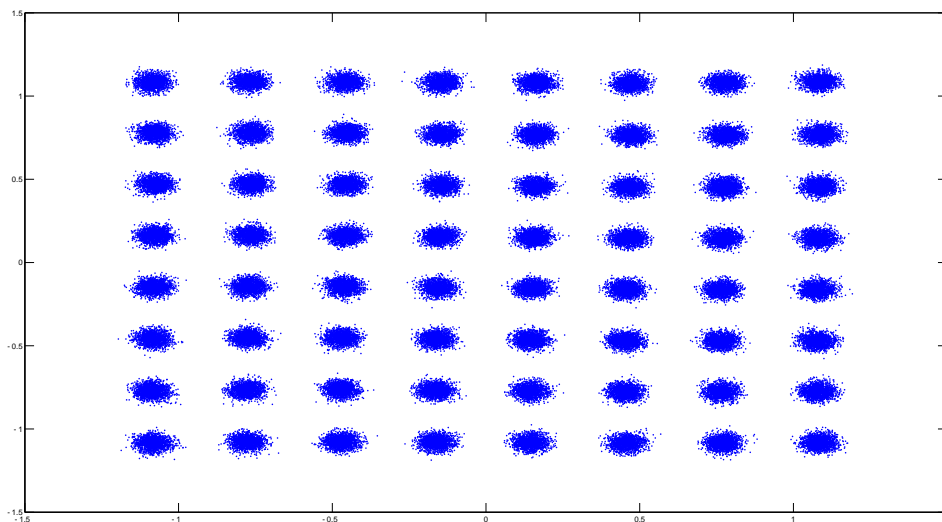


Figure 3.35 Constellation of the first compensated 100000 symbols.

The last block of the compensation chain is the BER computation. It is made the demodulation of both the compensated received sequence and the transmitted sequence and bit compared. Fig. 3.36 shows the BER found in function of a power factor.

3.3.3 Validation of the Results

For a BER comparison with a coverage prediction tool it is needed to average the BER for several measure points in turn of a central one. That is to average the effect of the small scale fading. For now the chain will be validated for a point to point link without small scale fading averaging.

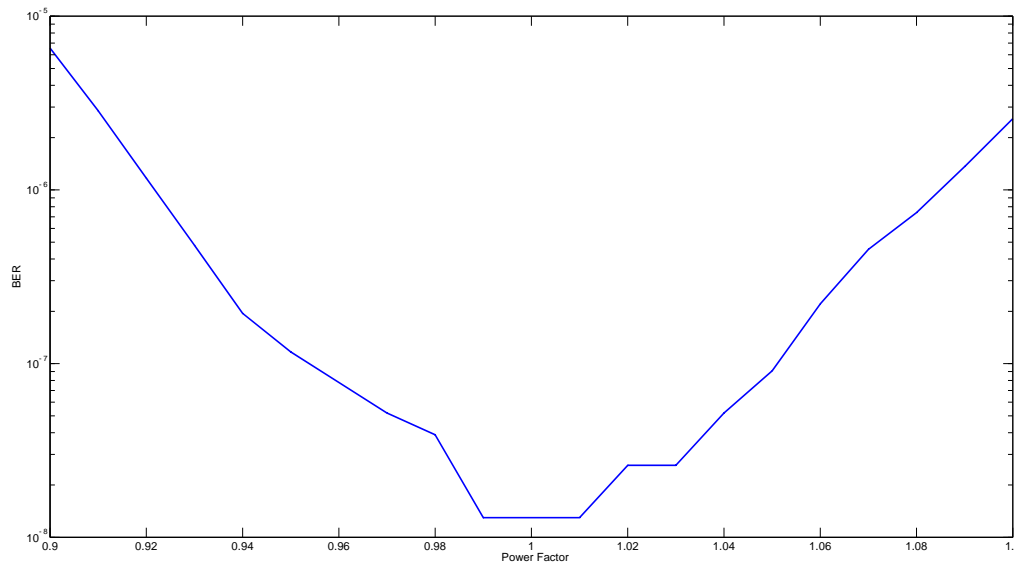


Figure 3.36 The BER in function of the normalized power of the sequence times a power factor.

Now it will be given the parameters of the measurement that give rise to most (less one) of the graphics of the last section. The modulation was 64-QAM. The measuring time was 3.7 sec giving rise to about 77Million bits. The acquisition sample rate was ten times the symbol rate. The VSA noise level was -88dBm (in 3.5MHz bandwidth \Leftarrow Passband, RRC, Symbol Rate=3.5M). This corresponds to the sensitivity of the VSA that it is near the -153dBm/Hz. The received signal level was -59dBm. This corresponds to E_b / N_0 of 21.2 dB at passband. The noise or disturbance power level after all compensations is 1.65×10^{-3} for a symbol sequence power of one. By Eq. 3.6 [3] it can be computed E_b / N_0 before demodulation which is about 20dB.

$$\sigma_{bb}^2 = \frac{mA^2}{(E_b / N_0) R_c \log_2(M)} \quad (3.6)$$

with σ_{bb}^2 the variance or power of the compensated discrete signal noise or disturbance, E_b the energy per bit, N_0 is the noise power density, m is the upsample factor ($m=1$), A^2 is the average power of the baseband symbols ($A^2=1$), R_c is the rate of the channel code ($R_c=1$) and M is the constellation size ($M=64$).

The values of E_b / N_0 at passband and after compensation are a close match in practical or measuring terms.

The theoretical BER for a Gaussian Channel and for $E_b / N_0 = 20$ dB is given by Eq. 3.7 [4]

$$BER = \frac{2(1-1/L)}{\log_2(L)} Q \left(\sqrt{\frac{3 \log_2(L)}{L^2 - 1} \frac{2E_b}{N_0}} \right) \quad (3.7)$$

with $L = \sqrt{M}$ and Q is the well-known Q function. The theoretical BER, considering the compensated signal is 2.3×10^{-8} . The practical BER was 1.3×10^{-8} but it is not representative because it only happen one error in a bit. In case of a longer acquisition, a close match only indicates that the disturbance or noise after compensation is Gaussian. The relevant match is between the passband signal and compensated sequence E_b / N_0 s.

4. Computation of statistics of the channel, simulation/measurement comparison

Radio propagation channels can experience the large scale fading and the small scale fading simultaneously. Since the large scale fading and the small scale fading should be tackled in different manners, we will introduce them separately in the following sections. Totally, we can extract the following fading statistics: for the large scale propagation characteristics, we can extract the path loss exponent and the standard deviation of the shadow fading. For the small scale fading, we can extract the Power Delay Profile (PDP), the envelope Probability Density Function (PDF), the Frequency Correlation Function (FCF), the Rice factor, the mean delay, and the root mean square delay. Moreover, we can also predict the Bit Error Rate (BER).

4.1 Extraction of the large scale propagation characteristics

In this section, we present the extraction of the large scale propagation characteristics, namely the mean path loss and the shadow fading. First, the large scale propagation characteristics are described. Then we check whether or not the MR-FDPF model is capable of simulating the shadow fading phenomenon. At last, how to extract the large scale propagation characteristics is addressed.

4.1.1 Large scale propagation characteristics

When expressed in dB, the instantaneous path loss can be considered as the sum of the mean path loss, shadow fading and small scale fading as follows [1]

$$PL(d) = L(d) + X_\sigma + F \quad (4.1)$$

where $PL(d)$, $L(d)$, X_σ and F denote the instantaneous path loss, the mean path loss, shadow fading and small scale fading associated with the Tx-Rx (transmitter and receiver) separation distance d , respectively. Unlike the small scale fading which characterizes the rapid fluctuations of the received signal strength over very short travel distances (a few wavelengths), the large scale fading, i.e., shadow fading, characterizes signal strength variation over large distances [2].

Typically the mean path loss $L(d)$ is deterministic and is log dependent on the Tx-Rx separation distance d according to the one-slope model as follows

$$L(d) = L_0 + 10n \cdot \log_{10}(d) \quad (4.2)$$

where L_0 is a constant which accounts for system losses and n is the path loss exponent depending on the specific propagation environment. For instance in free space propagation $n = 2$.

The shadow fading X_σ is a zero-mean Gaussian distributed random variable (in dB) with standard deviation σ . The small scale fading is typically described by Rayleigh distribution for NLOS (non-line-of-sight) propagation and Rice distribution for LOS (line-of-sight) propagation [2].

The large scale propagation characteristics are very useful for determining the coverage area or evaluating system performance. For instance, with large scale propagation characteristics, system designers can determine how large the coverage area of a transmitter is and what fade margin is required to achieve a certain level of edge reliability.

4.1.2 Capability of simulating shadow fading phenomenon

From a theoretical point of view, small scale fading and shadow fading can be averaged out over an area, e.g. a square area, of a proper size. In other words, neither small scale fading nor shadow fading can be observed if the averaging area is large enough. The obtained path loss curve after averaging over a large enough area will be very smooth because it only contains the mean path loss. If MR-FDPF is capable of simulating the fading characteristics, it should show the averaging effect described above. Therefore, we investigate this by doing averaging over square areas of different sizes, from $5\lambda \times 5\lambda$ to $50\lambda \times 50\lambda$, with a step of 5λ , where λ denotes the wavelength. The averaging effect from MR-FDPF simulation is shown in Fig. 1. In this figure, a shadowing effect is evidenced over $5\lambda \times 5\lambda$ area, and $10\lambda \times 10\lambda$ area too, but there is a trend: the larger the size of the averaging area is, the less the shadowing effect can be observed. When the size of the area is about $40\lambda \times 40\lambda$, the shadowing effect almost can not be observed, which means that the shadowing has been averaged out. Fig. 4.1 demonstrates that the MR-FDPF is capable of providing the shadow fading phenomenon.

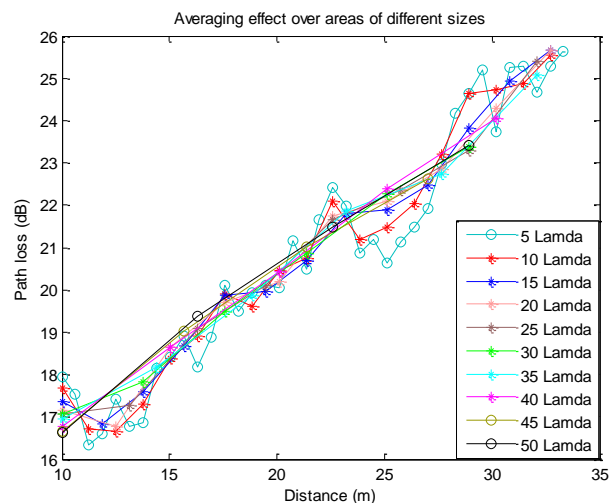


Figure 4.1: The averaging effect over areas of different sizes.

4.1.3 Extraction of the large scale propagation characteristics

In order to get the large scale propagation characteristics, first we should average out the small scale fading. The obtained path loss after averaging out the small scale fading is usually called the local mean path loss. The most critical point for averaging out the small scale fading is the determination of the size of the averaging area.

According to [3] [4], if the samples are expressed in dB, the number of samples associated with 90% confidence interval is $N = 85$. Provided that for the MR-FDPF model, a square area can be chosen, the number of samples associated with each side of the square is thus \sqrt{N} . In addition, for a Rayleigh distributed signal envelope, the uncorrelated distance for two adjacent samples is 0.38λ [4]. Finally, we obtain the minimum length of the side of the square is $0.38\lambda \times \sqrt{N}$. On the other side, if it is a LOS propagation scenario, the received signal envelope may be Rice distributed rather than Rayleigh, then in this case a smaller sample size may be sufficient [4].

Since the performance of the MR-FDPF will be verified by comparison to the measurements conducted at Stanford by Dr. N. Czik [5] which will be described in subsection 4.1.4, we run the MR-FDPF

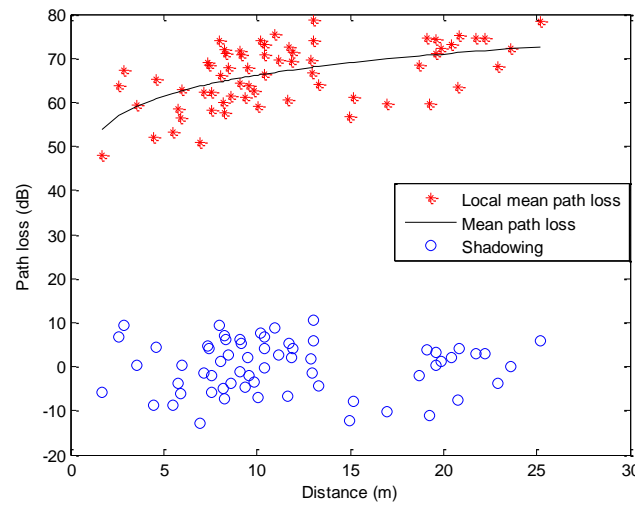


Figure 4.2: The obtained local mean path loss, mean path loss and shadowing from the MR-FDPF model.

simulation with the same scenario as in the measurements. The simulation frequency is 2.45 GHz, and there are 8 transmitters and 8 receivers (i.e. 64 links in total). For more detailed scenario information, please refer to subsection 4.1.4.

According to the description above, the local mean path loss averaged over an area of $3.8\lambda \times 3.8\lambda$ is obtained, shown in Fig. 4.2 by the red stars.

The local mean path loss includes both the mean path loss and the shadow fading. Since the mean path loss depends on the log distance shown in Eq. 4.2, we choose to get the L_0 and n by using the curve fitting tool of Matlab such that the difference between the local mean path loss and the estimated mean path loss is minimized in a mean square error sense. Substituting the estimated $L_0 = 50.26$ and $n = 1.592$ into Eq. 4.2, we obtain the mean path loss

$$L(d) = 50.26 + 10 \times 1.592 \cdot \log_{10}(d) \quad (4.3)$$

Here $n = 1.592$ indicates that there exists a waveguide effect in the propagation. The obtained mean path loss is shown by the black continuous curve in Fig. 2. Finally, the shadow fading can be obtained by just subtracting the mean path loss from the local mean path loss, which is denoted by the blue circles in Fig.4.2.

In order to validate the shadow fading we have extracted, we compare its Cumulative Distribution Function (CDF) with that of a normal distribution. The comparison result is shown in Fig. 4.3. From the figure, we can see that the extracted shadow fading and the theoretical result are very similar.

Moreover, we also compute the standard deviation of the extracted shadow fading, which is 5.87 dB.

4.1.4 Experimental evaluation

The results from the measurement campaign corresponding to “I2I moving receivers” scenario conducted at Stanford [5] are exploited to verify the performance of the proposed approach based on the MR-FDPF.

The office scenario

The scenario was a typical 16 x 34 m office space made of 30 cubicles and 7 small separated rooms. 8 transmitters and 8 receivers were distributed in the office as illustrated in Fig. 4.4. All the transmitters were fixed in their locations, whereas all the receivers were randomly moved inside their cubicles when conducting the measurements. All the transmitters and receivers were equipped with omnidirectional antennas. Four materials were mainly used in the office, i.e., concrete for the main walls, plaster for the

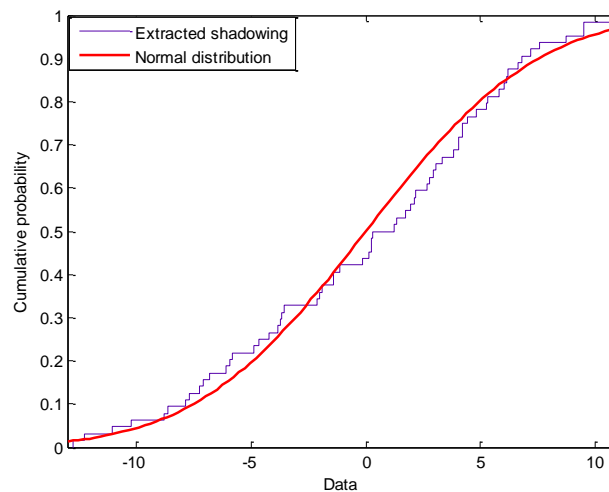


Figure 4.3: CDF comparison between the extracted shadow fading from the MR-FDPF model and normal distribution.

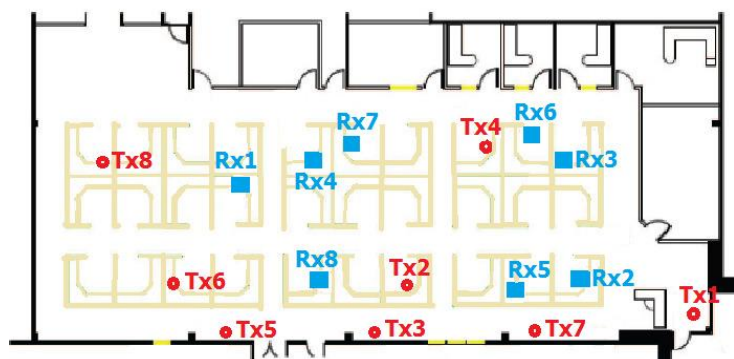


Figure 4.4: The measurement scenario.

internal walls, glass for the external glass wall and wood for the cubicles located in the central part of the office.

Measurement setup

8 x 8 MIMO channels at a center frequency of 2.45 GHz were measured simultaneously with a RUSK MEDAV channel sounder [6]. In the measurement, 120 time blocks covering a total time of 32 seconds and 220 frequency bins covering a total bandwidth of 70 MHz were recorded. For large scale fading study, narrowband measurements are sufficient, hence the measurement data is restricted to the center frequency. Note that the averaging over the 120 time blocks implies the averaging over space since the receivers were moving when recording.

Simulation

In order to verify the proposed method, the simulation is conducted at 2.45 GHz with 0 dBm transmit power. The space resolution of the simulation is 2 cm. The Fig. 4.5 presents the radio coverage simulated with the MR-FDPF model.

Results

Here, we extract the large scale propagation characteristics from the measurement. First of all, we obtain the local mean power by averaging over the 120 time blocks, which is shown by the red stars in Fig. 4.6. In the same way as in the simulation, the deterministic mean path loss is obtained by curve fitting

$$L(d) = 47.25 + 10 \times 1.442 \cdot \log_{10}(d) \tag{4.4}$$

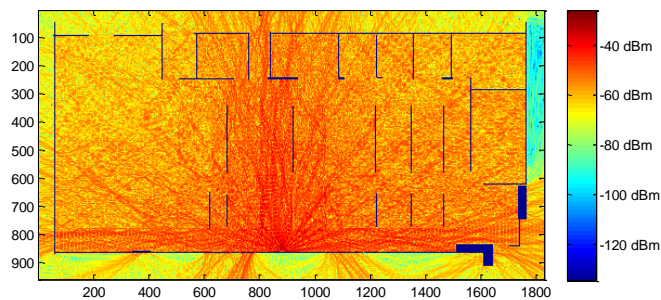


Figure 4.5: radio coverage prediction provided by the MR-FDPF model at 2:45 GHz plotted in dBm.

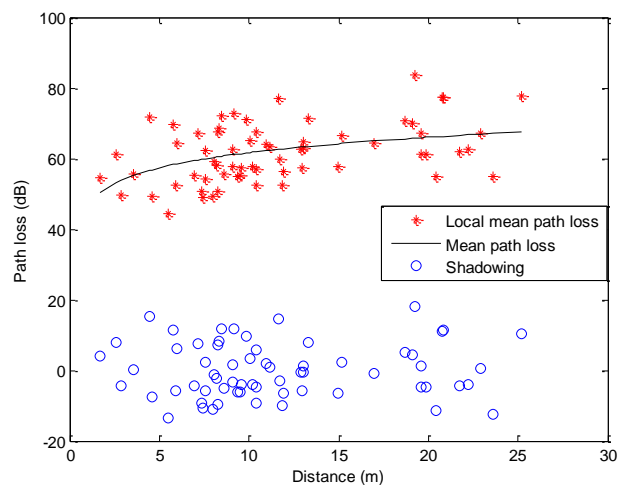


Figure 4.6: The obtained local mean path loss, mean path loss and shadowing from measurement.

The mean path loss is shown in Fig. 4.6 by the black continuous curve. Once we get the mean path loss, the shadow fading is obtained by subtracting the mean path loss from the local mean path loss, which is denoted by the blue circles in Fig. 4.6.

The CDF comparison between the extracted shadow fading and normal distribution is shown in Fig. 4.7. This good match demonstrates that the proposed approach for extracting the shadow fading is effective. The standard deviation of the extracted shadow fading from the measurement is 7.66 dB.

Finally, by comparing the parameters extracted from the MR-FDPF model and measurement in Tab. 4.1, we can see that they fit each other very well. The path loss exponents n both from the MR-FDPF model and measurement are smaller than 2, which indicates that there exists a waveguide effect in the propagation. The standard deviation of shadowing from simulation is slightly lower than that from measurement. We suggest that this is due to the unmodeled furniture which would contribute more to fading. The match between the simulation and measurement demonstrates that the MR-FDPF model is capable of simulating large scale propagation characteristics.

	n	The standard deviation σ
MR-FDPF	1.59	5.87 dB
Measurement	1.44	7.66 dB

Table 4.1: Comparison between the simulation and measurement

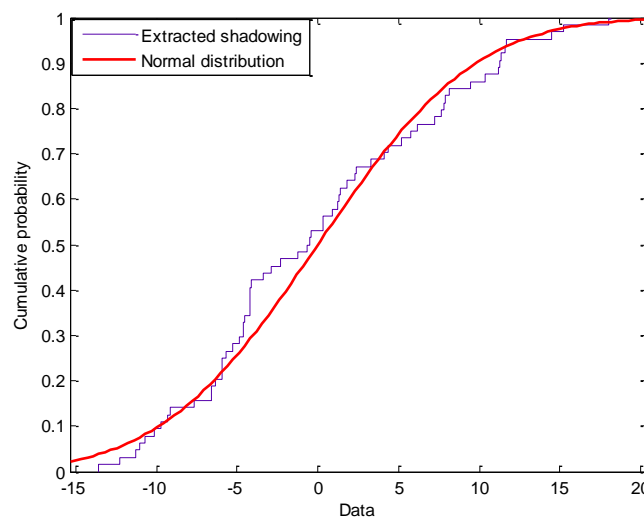


Figure 4.7: CDF comparison of the extracted shadowing and normal distribution from measurement.

4.2 Extraction of the small scale fading statistics

In this section, we describe how the small scale fading statistics can be extracted from the electric field strength predicted by the MR-FDPF model. The extraction performance is verified by comparisons with measurement results.

4.2.1 Extraction of the small scale fading statistics

First, note that since the transmitted signal is always known, the electric field strength predicted with the MR-FDPF method at the position \bar{r} can be equivalently described in terms of the transfer function $H(f, \bar{r})$ of the propagation channel between the transmitting antenna and a virtual receiving antenna located at the position \bar{r} .

At every position \bar{r} , the electric field strength and, consequently, the radio channel transfer function $H(f, \bar{r})$ satisfies the wave equation [2]. Thus, the transfer function $H(f, \bar{r})$ can be legitimately represented by the SLAC model [4] defined as follows

$$H(f, \bar{r}) = \sum_{l=1}^N \alpha_l \exp(j[\Phi_l - \vec{k}_l \cdot \bar{r} - 2\pi f \tau_l]) + w(f, \bar{r}) \quad (4.5)$$

Each plane wave in Eq. 4.5 is characterized by the constant amplitude $\{\alpha_l\}$, the wavevector $\{\vec{k}_l\}$, the time delay $\{\tau_l\}$, and the phase $\{\Phi_l\}$ which is a realization of the random variable following the uniform distribution over the interval $[0, 2\pi]$. The term $w(f, \bar{r})$ in Eq. 4.5 corresponds to the diffuse wave component [4].

Implicitly, in Eq. 4.5, we assume that the transfer function $H(f, \bar{r})$ as well as the electric field strength predicted by the MR-FDPF method is a realization of the corresponding stochastic process. This assumption can be justified by observing that multiple uncertainties are inherent in modeling any complex propagation scenario. For example, adjustments (corrections) made to the model geographical database, would result in a new realization of the predicted transfer function $H(f, \bar{r})$.

We also presume that the diffuse wave component $w(f, \bar{r})$ in Eq. 4.5 is a realization of a random zero-mean complex Gaussian process uncorrelated with respect to the frequency f and the spatial position \bar{r} .

The parameters $\{\alpha_l, \tau_l, \vec{k}_l\}_{l=1}^N$ of the SLAC model in Eq. 4.5 are determined by using the well-known space-alternating generalized expectation-maximization algorithm (SAGE) [8]. Note that under assumptions made above, the estimates $\{\hat{\alpha}_l, \hat{\tau}_l, \hat{\vec{k}}_l\}_{l=1}^N$ obtained by the SAGE algorithm asymptotically approach the maximum likelihood (ML) estimates.

The estimated parameters $\{\hat{\alpha}_l, \hat{\tau}_l, \hat{\vec{k}}_l\}_{l=1}^N$ of the SLAC model in Eq. 4.5 allow determining the statistical properties of the radio channel corresponding to the link between the transmitter and receiver positions. The statistical properties, namely the power delay profile (PDP) $\hat{S}(\hat{\tau}_l)$, the envelope PDF $\hat{f}_R(\rho)$, the FCF $\hat{C}(\Delta f)$, the Rice factor \hat{K} , the mean delay $\hat{\tau}_m$, and the root mean square delay $\hat{\tau}_{rms}$ are calculated as follows [9]:

$$\hat{S}(\hat{\tau}_l) = \sum_{l=1}^N |\hat{\alpha}_l|^2 \delta(\tau - \tau_l) \quad (4.6)$$

$$\hat{f}_R(\rho) = \rho \int_0^\infty J_0(\nu\rho) \left[\prod_{l=1}^N J_0(\hat{\alpha}_l \nu) \right] \nu d\nu \quad (4.7)$$

$$\hat{C}(\Delta f) = \sum_{l=1}^N |\alpha_l|^2 \exp(-j2\pi\tau_l \Delta f) \quad (4.8)$$

$$\hat{K} = \frac{\max((\hat{\alpha}_l)^2)}{\sum_{l=1}^N (\hat{\alpha}_l)^2 - \max((\hat{\alpha}_l)^2)} \quad (4.9)$$

$$\hat{\tau}_m = \frac{\sum_{l=1}^N \hat{\tau}_l \hat{\alpha}_l^2}{\sum_{l=1}^N \hat{\alpha}_l^2} \quad (4.10)$$

$$\hat{\tau}_{rms} = \sqrt{\frac{\sum_{l=1}^N (\hat{\tau}_l - \hat{\tau}_m)^2 \hat{\alpha}_l^2}{\sum_{l=1}^N \hat{\alpha}_l^2}} \quad (4.11)$$

Furthermore, multiple realizations of the transfer function $H(f, \vec{r})$ can be obtained by substituting the estimated parameters $\left\{ \hat{\alpha}_l, \hat{\tau}_l, \hat{k}_l \right\}_{l=1}^N$ into the SLAC model in Eq. 4.5.

4.2.2 Experimental evaluation

In order to verify the performance of the proposed method, we conduct both the simulation and measurement.

Simulation

In the simulation, CITI lab has been chosen as the indoor propagation scenario where MR-FDPF method is used. The radio coverage map of CITI lab predicted with the MR-FDPF method is presented in Fig. 4.8. In order to extract the fading statistics, the simulations have been performed at 41 frequencies, at the range 3.477GHz to 3.523GHz, with the frequency step 1.152MHz. The spatial resolution of the MR-FDPF method is 1.4cm. The locations of the transmitter and the virtual receiver are indicated by Tx and Rx, respectively, in Fig. 4.8. The Rx is a virtual rectangular antenna array consisting of $7 \times 7 = 49$ equidistant elements with spacing equal to 1.4cm. The transmitter power is 17dBm. The SAGE algorithm is applied to the predicted channel transfer function. The number of multiple paths is assumed to be 15.

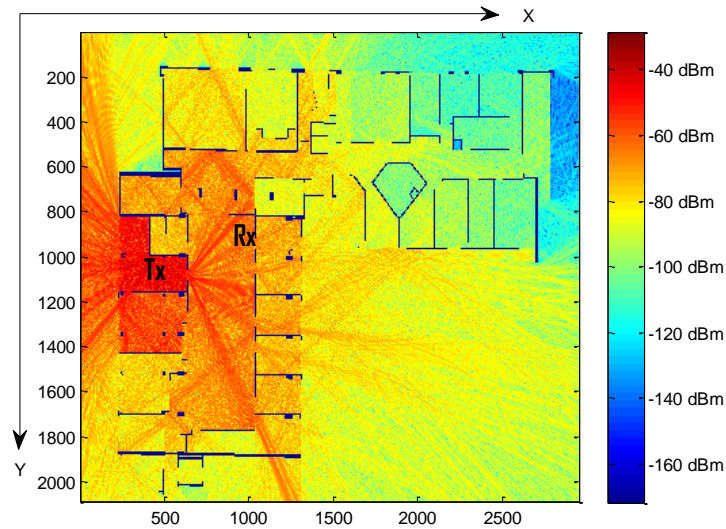


Fig. 4.8: The coverage map predicted with MR-FDPF method

Measurement

The measurement is conducted at the same position in CITI lab as shown in Fig. 4.8. The Transmitter includes the arbitrary waveform generator (ESG4438C by Agilent Technology ©) and the directional

antenna (3164-08 by ETS-Lindgren ©). The vector signal analyser (VSA 89641 by Agilent Technology ©) is equipped with a 3.5GHz, 6dBi, omnidirectional antenna. The 0.2dB bandwidth of the VSA is 20MHz. Fourteen measurements corresponding to different time instances have been conducted. For each measurement, 9 positions are measured around the Rx in Fig. 4.8. For each referred receiving position, 4608080 samples are collected during 100ms.

Results

In order to evaluate the proposed approach, we compare the simulation and measurement results. Fig. 4.9 presents the comparison of channel impulse responses of the SLAC model and that obtained directly by the MR-FDPF method. We can see that they have a good match of each other. The envelope PDFs of the SLAC model estimated by the proposed approach has also been compared to the histogram of channel transfer function in Fig. 4.10. The histogram of the envelope of the measured channel transfer function is depicted in Fig. 4.11. The Rayleigh PDF curve is also plotted for comparison reasons. From Fig. 4.10 we see that the PDF of the SLAC model fits very well the PDF of the MR-FDPF method. Furthermore, both of them match the PDF obtained from the measurements and shown in Fig. 4.11.

The angle spectrum of the SLAC model is given in Fig. 4.12. As can be seen from Fig. 4.12, the estimated angles are grouped near 180 and 0/360 degrees. The group around 180 degrees includes the line-of-sight (LOS) direction, which is approximately equal to 160 degrees. The second group, i.e., the waves with the angles near 0/360 degrees are mainly due to the reflection by the walls behind the Rx.

By the proposed approach, we can also obtain the estimated Rice factor, mean delay, and root mean square delay from the predictions provided by the MR-FDPF method. The results are presented in the Table 4.2.

Parameters	From the SLAC Model	Mean Values from Measurements	Mean Values from Measurements
The Rice factor	1.3979	1.4705	[0, 4.9432]
The Root mean square delay	31.78ns	52.71ns	[0, 141.58ns]
The mean delay	57.568ns		

TABLE 4.2 Comparison of Estimated Values from the SLAC Model and Measurements

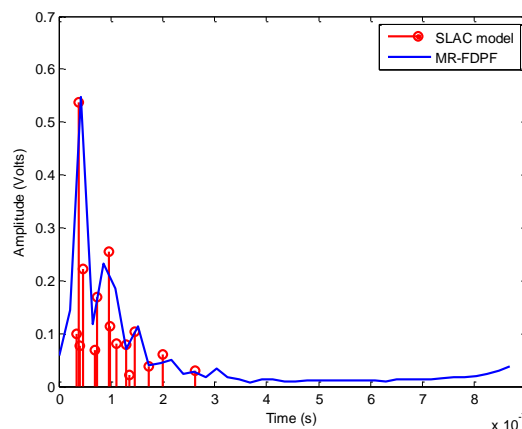


Fig. 4.9: The comparison of the impulse responses

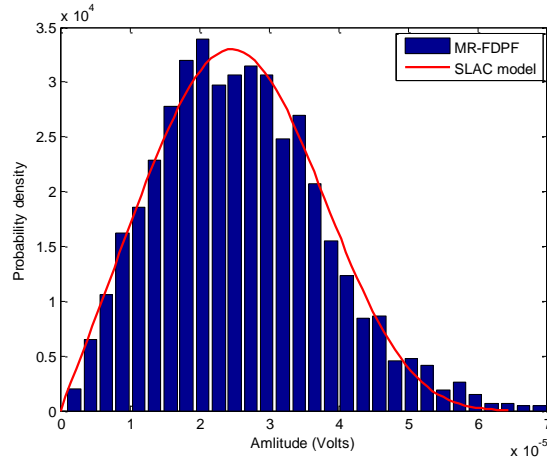


Fig. 4.10: The comparison of the channel envelope PDFs

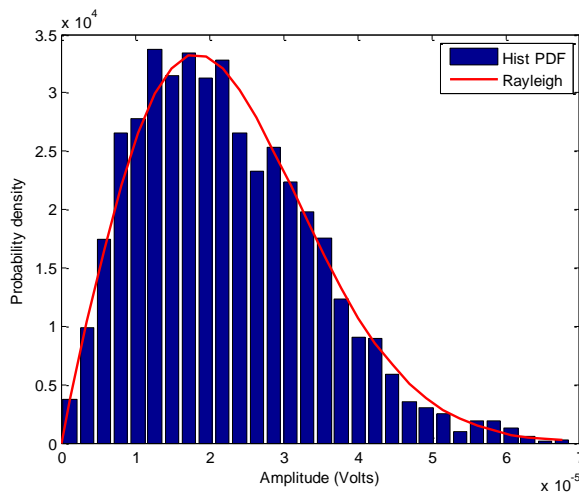


Fig. 4.11: The histogram PDF of measurements

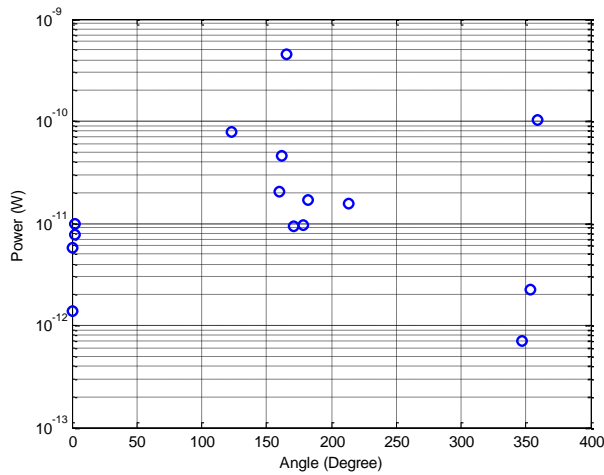


Fig.4.12: The estimated channel angular power spectrum

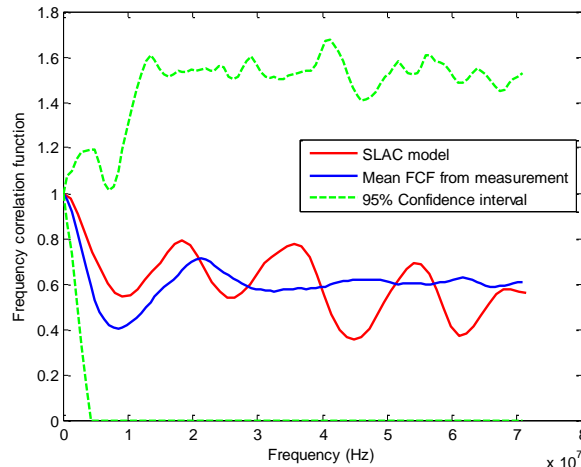


Fig. 4.13: The comparison of FCFs obtained from the SLAC model and measurements

The angle spectrum and the mean delay estimated by the proposed approach have not been compared with the characteristics estimated from the measurements as the measurements taken at different time instances can not be synchronized on the VSA 89641. Also for this reason, we have not presented here the estimated values of other parameters, such as the angle of arrival (AOA) spread, the mean power, and the spatial cross-correlation function (SCCF), which can also be estimated by the proposed approach.

The 95% confidence intervals calculated using Chebyshev's inequality are also given in Table I. It can be seen that the simulation results are well located in the 95% confidence intervals of the measurements. In Fig. 13, we show the comparison of the estimated FCF obtained from the SLAC model and the measurements data.

The angle spectrum and the mean delay estimated by the proposed approach have not been compared with the characteristics estimated from the measurements as the measurements taken at different time instances can not be synchronized on the VSA 89641. Also for this reason, we have not presented here the estimated values of other parameters, such as the angle of arrival (AOA) spread, the mean power, and the spatial cross-correlation function (SCCF), which can also be estimated by the proposed approach.

4.3 Realistic prediction of BER for adaptive modulation

Bit Error Rate (BER) is an important parameter for evaluating the performance of wireless networks. Many wireless applications, such as, adaptive modulation and coding (AMC) scheme and optimal power allocation, use the BER to dynamically adapt their schemes. Hence, a realistic and accurate prediction of BER is crucial for these higher-layer protocols and applications.

Moreover, from the channel modeling perspective, many radio propagation simulators provide the mean power prediction. However, only mean power is not enough to fully describe the behavior of radio channels. Realistic radio channels are random processes and present fading due to e.g. movements of surrounding objects. A fine radio propagation simulator should also be able to provide the fading information, and thus an accurate BER prediction can be achieved. Actually, the BER

statistics is indeed the input needed by network simulators, e.g. NS-3, to perform realistic simulations.

In this section, a realistic BER for indoor wireless transmissions is predicted. With the predicted BER, adaptive modulation is implemented at the end.

4.3.1 Theoretical BER analysis

Theoretically, the average BER over fading channels is obtained by averaging the corresponding BER of Additive White Gaussian Noise (AWGN) channels over the Probability Density Function (PDF) of the instantaneous SNR which depends on the fading [11]. That is

$$P_{b:fading}(E) = \int_0^{\infty} P_{b:AWGN}(E; \gamma) P_{\gamma}(\gamma) d\gamma \quad (4.12)$$

where $\gamma \triangleq \alpha^2 E_b / N_0$ denotes the instantaneous SNR per bit, α is the fading amplitude, E_b is the signal energy per bit, N_0 is the noise power spectral density, $P_{\gamma}(\gamma)$ is the PDF of the instantaneous SNR depending on the fading, $P_{b:fading}(E)$ is the BER over fading channels and $P_{b:AWGN}(E)$ is the BER over AWGN channels conditioned on the fading.

Normally, the $P_{b:AWGN}(E)$ is a Gaussian Q-function for ideal coherent detection. On the other hand, the Moment Generating Function (MGF) $M_g(s)$ associated with a specific fading is defined by [11]

$$M_{\gamma}(s) = \int_0^{\infty} e^{s\gamma} \cdot P_{\gamma}(\gamma) d\gamma \quad (4.13)$$

Using the definition of the MGF together with the desired form of the Gaussian Q-function instead of the classic form, which is

$$Q(x) = \frac{1}{\pi} \int_0^{\pi/2} \exp\left(-\frac{x^2}{2 \sin^2 \theta}\right) d\theta \quad (4.14)$$

we come to a unified and simplest way for computing the $P_{b:fading}(E)$ since the MGFs of a number of fading models are already available. Then typically, the $P_{b:fading}(E)$ is just a single integral with finite limits and integrand containing the MGF of the fading.

One point we should emphasize is that the $P_{b:AWGN}(E)$ here which is used to compute the $P_{b:fading}(E)$ should not be the commonly used approximate AWGN BER obtained from the approximate relationship between the BER $P_b(E)$ and Symbol Error Rate (SER) $P_s(E)$ as follows

$$P_{b:AWGN}(E) \approx \frac{P_{s:AWGN}(E)}{\log_2 M} \quad (4.15)$$

because this approximation is only valid for large symbol SNR, but the limits of the integral in equation (4.12) are from zero to infinity (i.e. g can vary from zero to infinity over fading channels). The $P_{b:AWGN}(E)$ used here should be either the exact AWGN BER or the approximate AWGN BER which is accurate at both low and high SNR.

Here, we adopt the approximate AWGN BER of Lu et al. [12] as the $P_{b:AWGN}(E)$ to compute the $P_{b:fading}(E)$ since it is very accurate at both low and high SNR and it is much simpler than the exact AWGN BER [13] [14] [15] [16]. Thus, for M-PSK modulations, we have

$$P_{b:AWGN}(E) \approx \frac{2}{\max(\log_2 M, 2)} \cdot \sum_{i=1}^{\max(\frac{M}{4}, 1)} Q \left(\sqrt{\frac{2E_b \log_2 M}{N_0}} \sin \frac{(2i-1)\pi}{M} \right) \quad (4.16)$$

where M is the modulation order, e.g. $M = 2$ for BPSK, $M = 4$ for QPSK. For M-QAM modulations, we have

$$P_{b:AWGN}(E) \approx \frac{4}{\log_2 M} \left(1 - \frac{1}{\sqrt{M}}\right) \cdot \sum_{i=1}^{\sqrt{M}/2} Q \left((2i-1) \sqrt{\frac{3E_b \log_2 M}{N_0}} \right) \quad (4.17)$$

Therefore, for the BER for the M-PSK modulations over fading channels, we have

$$P_{b:fading}(E) \approx \frac{2}{\max(\log_2 M, 2)} \cdot \sum_{i=1}^{\max(\frac{M}{4}, 1)} \frac{1}{\pi} \int_0^{\pi/2} M_\gamma \left(-\frac{\log_2 M}{\sin^2 \theta} \sin^2 \frac{(2i-1)\pi}{M} \right) d\theta \quad (4.18)$$

For the BER for the M-QAM modulations over fading channels, we have

$$P_{b:fading}(E) \approx \frac{4}{\log_2 M} \left(1 - \frac{1}{\sqrt{M}}\right) \cdot \sum_{i=1}^{\sqrt{M}/2} \frac{1}{\pi} \int_0^{\pi/2} M_\gamma \left(-\frac{(2i-1)^2 \cdot 3 \cdot \log_2 M}{2 \sin^2 \theta \cdot (M-1)} \right) d\theta \quad (4.19)$$

Therefore, the BER over fading channels depends exactly on the MGF of fading channels. Recall the MGF of fading channels, we know that the MGF of fading channels is usually related to the fading parameters and the average SNR. So in the following section, we introduce the methods for estimating the fading parameters, namely, the Rice K factor and the m parameter of the Nakagami- m fading.

4.3.2 Estimation of the Rice K factor

In multipath propagation channels, Rayleigh and Rice are the most widely used distributions for modeling the small-scale fading [7]. Rayleigh distribution applies for non-line-of-sight (NLOS) scenarios, whereas Rice distribution is more suitable when there exists also a line-of-sight (LOS) component in the propagation. The Rice factor is defined as the ratio of the power of the LOS component to the NLOS components (usually called diffuse components)

$$K = \frac{A^2}{2s^2} \quad (4.20)$$

where A is the amplitude of the LOS component and $2s^2$ is the variance of the diffuse components. Over the past few decades, estimation of K factor has attracted great interest [8]–[10] since Rice K factor is an indicator of link quality. It is of importance to remind that Rayleigh distribution is a special case of Rice when $K = 0$, and when $K \rightarrow \infty$, Rice distribution approximates Gaussian distribution.

The most commonly used $K \rightarrow \infty$ method for estimating the K factor is the moment-based method [8] because of its simplicity compared to other methods, such as Maximum-Likelihood (ML) method [9], [10]. However, the moment-based method also has its limitation: when the K factor values are low, the moment-based

method can provide physically meaningless results [9]–[11]. In other words, the moment-based methodology works well for high K factor values.

In this section, the underlying scenario is an indoor environment with the transmitter (Tx) located in a small office, which implies that the K-values would be small at most of positions. Moreover, we will provide a K factor map of the whole building, so we hope the applicable range of estimation method can be as large as possible. Thus, we decide not to use the traditional moment-based method, but the RICEFIT method developed by Ridgway in MATLAB [12]. We choose the RICEFIT method also because it estimates the A and s separately. This is important for the goodness-of-fit tests, where a fully specified cumulative distribution function (CDF) is needed since only a K factor cannot completely determine the CDF of a Rice distribution.

4.3.3 REMARKS OF GOODNESS-OF-FIT TESTS

The Kolmogorov–Smirnov test [13] is one of the most well-known goodness-of-fit tests that is based on the maximum absolute vertical difference between the empirical distribution function (EDF) $F_n(x)$ and the hypothetical distribution function $F(x)$. The Kolmogorov–Smirnov test has the advantage of no assumptions made about the distribution of the data. However, the classic Kolmogorov–Smirnov test with the standard table of critical values is only valid when the $F(x)$ is fully specified. If the distribution is not fully specified and one or more parameters need to be estimated from the data, the results will be conservative [14]. The requirement of a fully specified distribution is a serious limitation because, in reality, most of the time we do not know exactly the distribution. We usually need to estimate parameters from the data. Therefore, some authors have developed the modified versions of the Kolmogorov–Smirnov test in order to be suitable for the case where a fully specified distribution cannot be provided. For example, Lilliefors has adapted the Kolmogorov–Smirnov test for normal distribution with unknown mean and variance in [15] and exponential distribution with unknown mean in [16], respectively. As a modification of the Kolmogorov–Smirnov test, the Anderson–Darling test [17] has been improved by Stephens to test for the following distributions with unknown parameters, such as normal, exponential, Weibull, extreme value, gamma, logistic, etc. [13].

What we plan to test in this letter is Rice distribution with unknown parameters, which is unfortunately, to the best of our knowledge, available neither from the Anderson–Darling test and Lilliefors test nor from any other available goodness-of-fit tests. This is because Rice distribution is not even a member of distributions in the location-scale family, in which case the distribution of the test statistics will not depend on the true values of the unknown parameters [13]. Since the goodness-of-fit test is not the main purpose of this work, we decide to still use the Kolmogorov–Smirnov statistic to perform the goodness-of-fit test, but just keep in mind that the results are conservative. For example, when the sample size is 144, the critical value 0.112 in the standard table corresponds to 5% significance level, but if we estimate any parameters of Rice distribution from the data, this 0.112 actually corresponds to a significance level less than 5%.

4.3.4 Results and discussion

Scenarios

The CITI building of INSA-Lyon in France is chosen as the indoor propagation scenario simulated with the WIPLAN tool. The simulation is performed at the frequency of 3.5 GHz with the spatial resolution of 2 cm. The location of the Tx is inside a small office that is indicated by Tx in Fig. 4.14. The equivalent isotropically radiated power (EIRP) of the Tx is 23 dBm.

Rice K Factor Map

As discussed above, here we use the RICEFIT method to estimate the Rice K factor. In Fig. 4.14, the K factor map extracted from the MR-FDPF model is shown in decibels. Each K factor in Fig. 4.14 is estimated over a

local area with 23×23 pixels, but only $12 \times 12 = 144$ of them taken according to an alternating pattern are used to perform the estimation since only uncorrelated samples are expected. According to [18], the uncorrelated distance of two samples is about $0.38l = 3.26\text{cm}$, and on the other hand, the distance between two pixels in the simulation is 2 cm, so each pixel will be uncorrelated with its second neighbor.

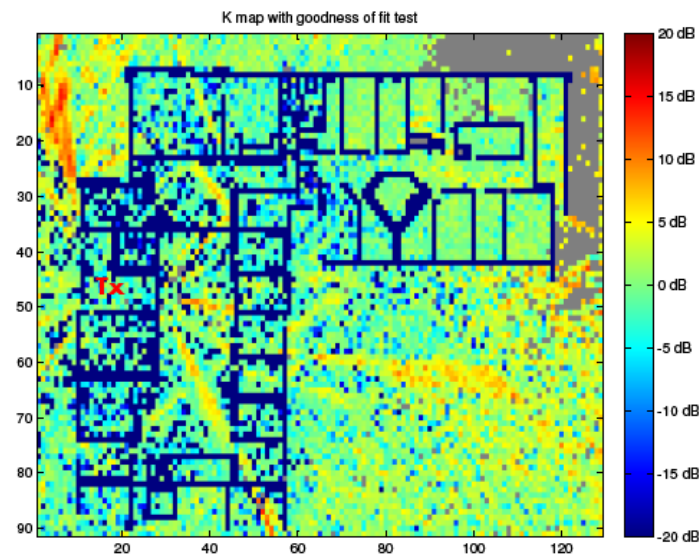


Fig. 4.14. Rice K map with goodness-of-fit test.

Evaluation of the Performance of the Estimation of the K Factor

In order to evaluate the performance of the estimated K factor, we perform the goodness-of-fit test. As discussed above, the Kolmogorov–Smirnov test is chosen and is performed at 5% significance level, although the actual significance level will be less than 5%. The gray points in Fig. 4.14 are the locations where the estimated K factor has failed the Kolmogorov–Smirnov test. It is observed that most of the failed K factors are located in the top right corner and outside the building. It is suggested that the envelop distribution there does not retain the strong Rice characteristics [19]. For the failed locations, we do not consider them in the following BER and modulation maps since the estimated K factors there are not reliable. They will be left in gray as well.

Prediction of BER and AMC

It has been shown that the Rice K factor has an important impact on the capacity and performance of wireless communication systems [20]. For instance, the BER characteristics of wireless communication systems depend not only on the signal-to-noise ratio (SNR), but also on the K factor. Therefore, the prediction of BER with considering the K factor will be more accurate.

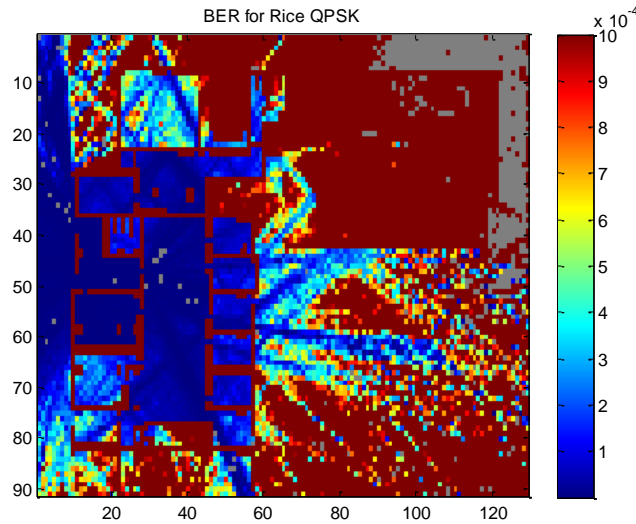


Fig. 4.15. BER map for QPSK modulation under Rice channels.

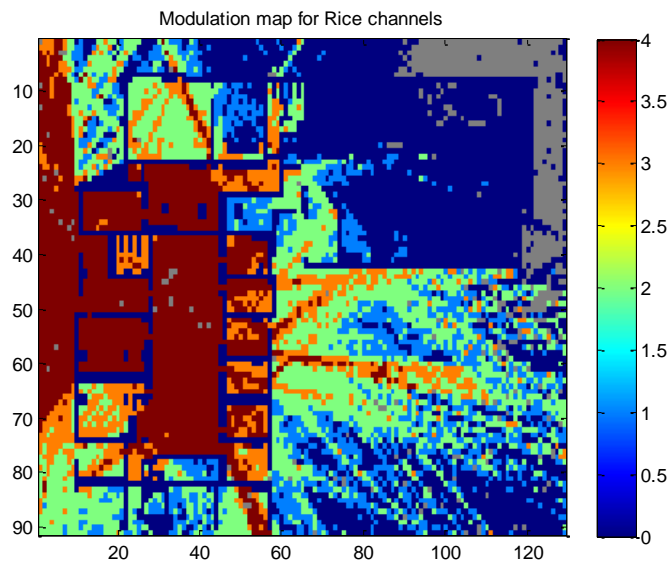


Fig. 4.16. Modulation map of AMC under Rice channels.

In Fig. 4.15, we show the BER map for QPSK modulation with considering the Rice K factor. The BER is calculated from the value of the K factor and the SNR, considering that the thermal noise is based on a 3.5 MHz bandwidth. We can also show the BER maps for AWGN channels. However, due to the limited space here, and also because the impact of K factor on BER is equivalent to the impact on modulation maps of adaptive modulation schemes, we decide to only show here the modulation maps.

In order to simplify the study, we consider only the uncoded BER of 10^{-3} as the threshold to adapt the modulation schemes. The possible modulations are BPSK, QPSK, 16QAM, and 64QAM. In Figs. 4.16 and 4.17, the modulation maps are obtained under the Rice and AWGN channels, respectively. In these two figures, the numbers in the color bar denote the modulation schemes: 1, 2, 3, and 4 denote BPSK, QPSK, 16QAM and 64QAM, respectively, and 0 denotes none of these four modulation schemes can satisfy the target BER. From

Figs. 4.16 and 4.17, we can see that modulation maps under Rice channels and AWGN channels are very different, which illustrates that the widely used mean power approach can lead to a completely false prediction.

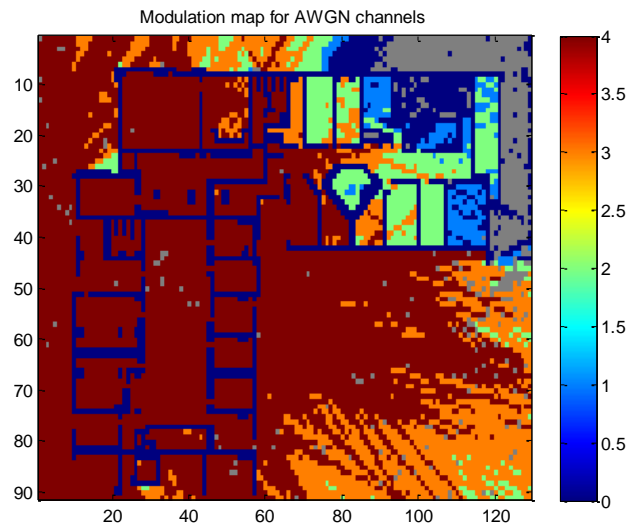


Fig. 4.17. Modulation map of AMC under AWGN channels.

Discussion

We see that a realistic prediction of BER and modulation maps of AMC can be achieved by considering not only the SNR, but also the fading parameters from WIPLAN. Although in this letter we only considered the Rice fading model, the methodology provided here is general and can be applied to other fading models, e.g., Hoyt and Weibull models.

In this section, we extracted the large scale propagation characteristics and the small scale fading statistics. For the large scale propagation characteristics, we extracted the path loss exponent and the standard deviation of the shadow fading. For the small scale fading, we extracted the Power Delay Profile (PDP), the envelope Probability Density Function (PDF), the Frequency Correlation Function (FCF), the Rice factor, the mean delay, and the root mean square delay. Moreover, we also predicted the Bit Error Rate (BER) at the last part of this section.

5. Description of Wideband Building-to-Building Measurement Campaign in Office and Residential Areas in Lund

5.1 Measurement Locations

The measurement campaign was carried out at 2 separate locations in Lund, Sweden. Location A was the E-Huset of LTH, Ole Römers väg 3, as shown in Fig. 5.1; Location B was a residential area around “Möllevångsvägen” to the north of Lund city centre, see Fig. 5.2

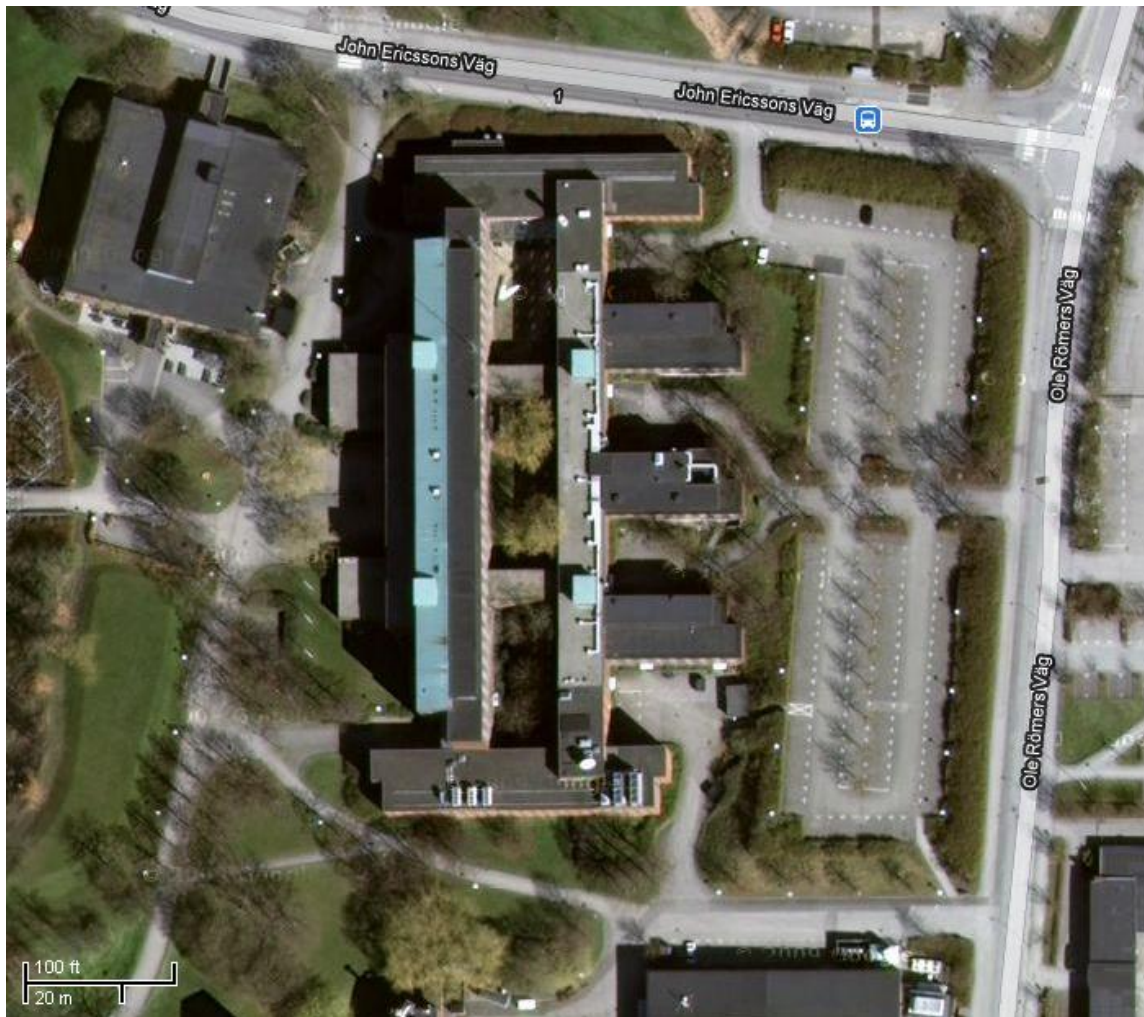


Figure 5.1: The E-Huset building of Lund Institute of Technology and its surrounding areas

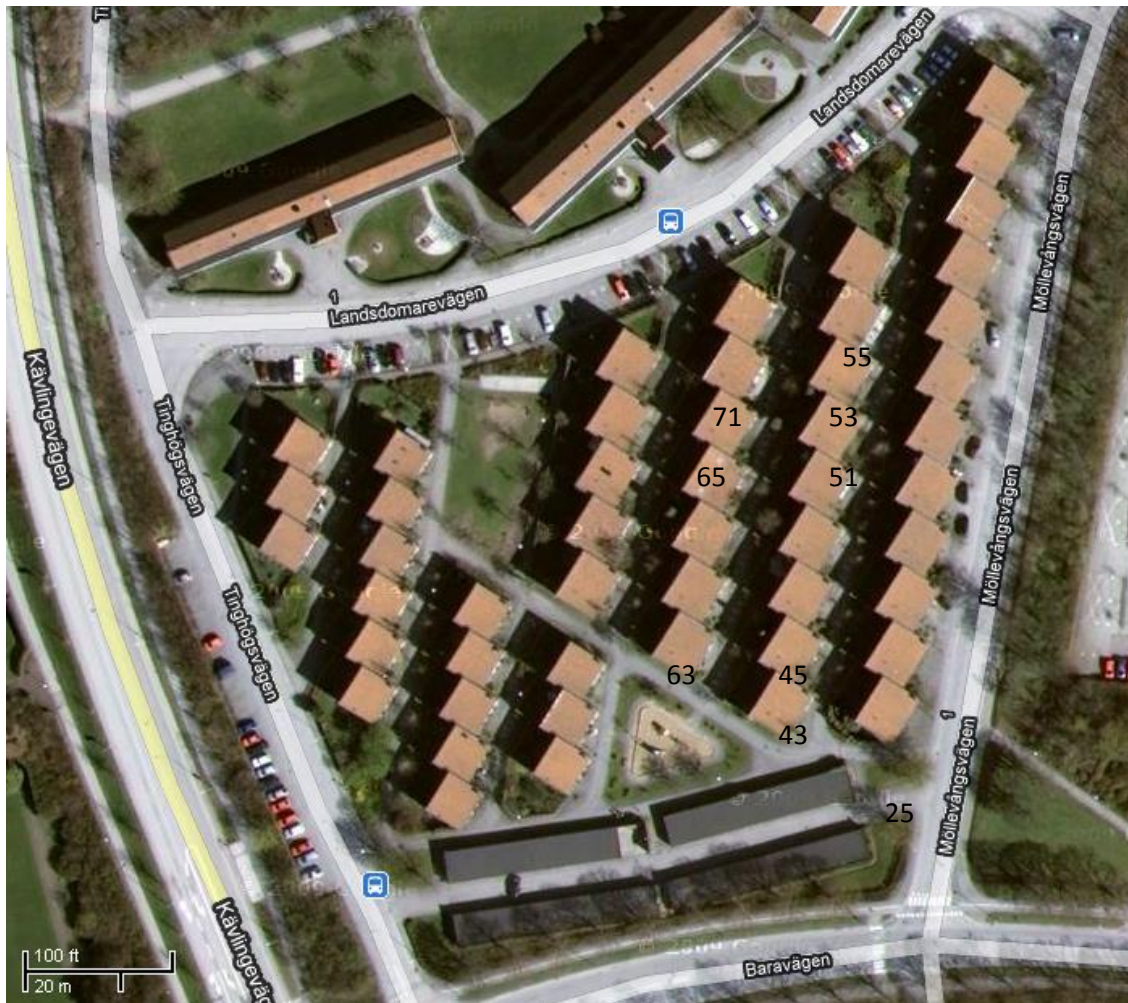


Figure 5.2: The residential area around “Möllevångsvägen”. The Rx was inside house 63.

5.2 Measurement set-up

We used a transmitting antenna (Tx) with 32 elements arranged in 4 rows by 8 columns on a planar surface (two dual polarized rows in the middle of the array were used) and a receiving antenna (Rx) with 64 elements arranged in 4 rows by 16 columns on a cylindrical surface.

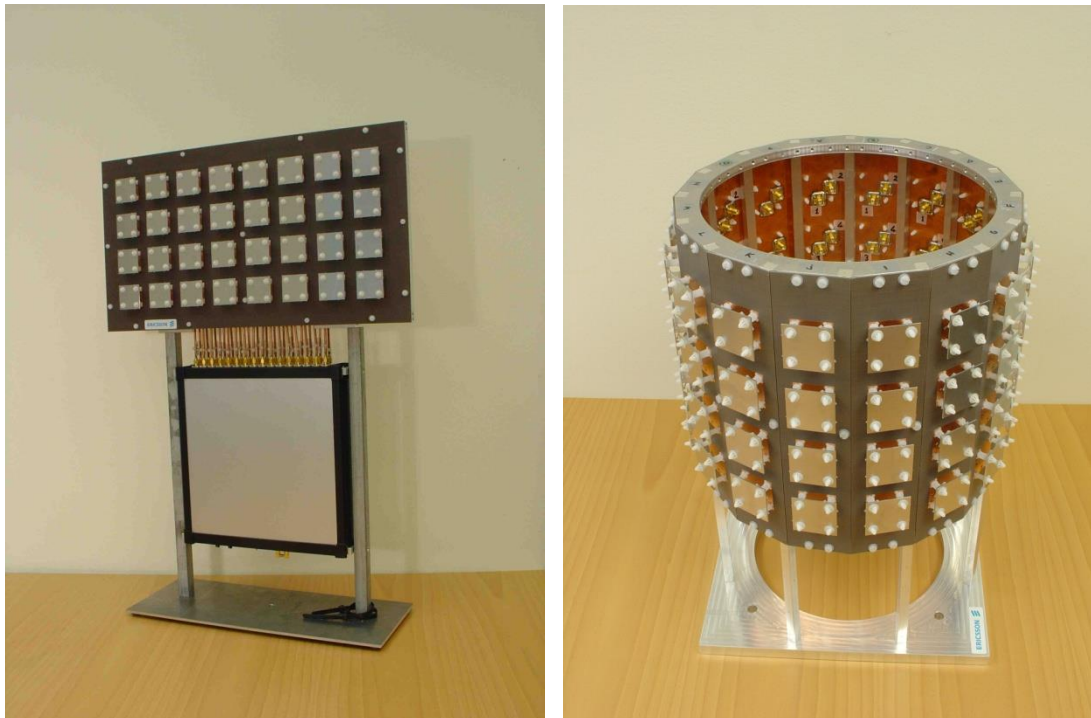


Figure 5.3 Tx antenna left (two mid rows were used for the measurements) and Rx antenna right.

Measurement data were recorded with the Lund RUSK LUND channel sounder as shown in Fig 5.4. The measurements were performed at a central frequency of 2.6 GHz and a signal bandwidth of 50 MHz. The transmit power was 40 dBm (the output power of the sounder is 27 dBm and an external amplifier with 13 dB gain incl. cable losses); a 20 dB attenuator as well as a 10 dB LNA were used at some measurement positions as specified in Tables 1 & 2 for location A and Table 4 for location B.

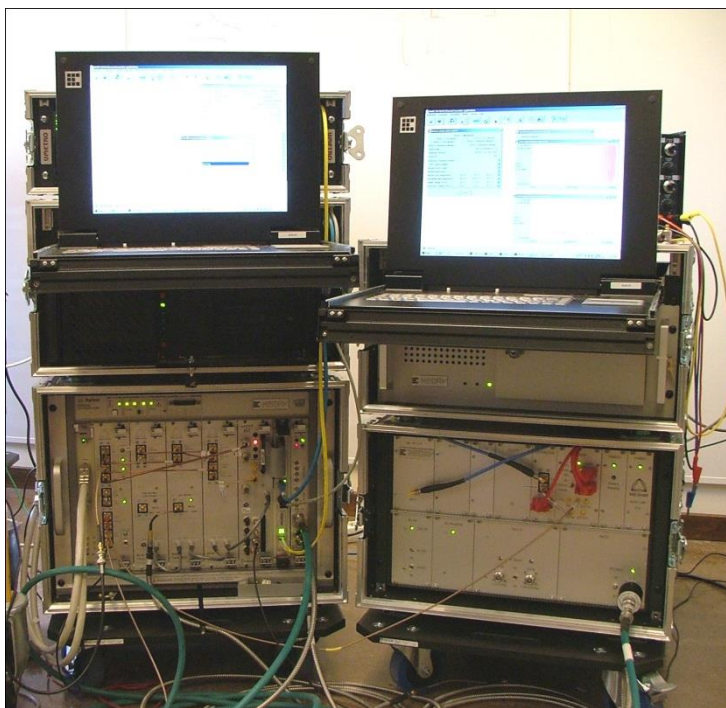


Figure 5.4 RUSK LUND channel sounder

The maximum delay recorded was 1.6s for location A and 3.2s for location B. At the receiver, the transfer function was measured at 161 points in the frequency domain. The sampling time for one MIMO snapshot was $2 \times 32 \times (128 + 1) \times 3.2 \times 10^{-6}$ s. Five consecutive snapshots form one block and there were no delay between those. Between each block there was an additional delay of 1 s, 20 blocks were measured per route so that the total measurement time was 20s. Post-analysis has shown that the channels in the outdoor measurement are not completely static within one block, so if not otherwise necessary avoid block averaging.

Measurement parameters (from the measurement data file)

frequency: 2.6000e+009
bandwidth: 50000000
length: 3.2000e-006
txpower: 27
extatten: 0
extgain: 0
hw: [1x1 struct]
antenna: [1x1 struct]
snap: 5
gap: 0
trigger: 'Internal time trigger'
blockgap: 1.0039
recmode: 'fixed number of blocks'
blocks: 20
samplerate: 640000000
dataformat: 'WMT-V1'
switchgaps: 1
ifreq: 160000000
freqmirrored: 0
agcmode: 0
period: [1x1 struct]
numsamples: 2048
numchannels: 4128
numsnapshots: 100

Location A: Office Building Environment

We mounted the Tx on a stand 1.68m tall and placed it in room 2316, on the 2nd floor. The Tx was positioned next to the walls of this room to emulate likely femtocell placements. In total, there were 4 distinct placements, one for each wall; the Tx was always facing the middle of the room except for the north position, where it was facing the window.

While the Tx was kept in room 2316 throughout, the Rx was moved between the surrounding rooms, corridors and outside of the building. It was placed on a trolley table with dimensions of 0.9m long by 0.6m wide by 0.85m tall.

We started our measurements in the large rooms of 2425 to 2430, which are located within the northernmost block of E-Huset, immediately across from the block containing the transmitter room. See Fig.3 below for detail of the measurement points.

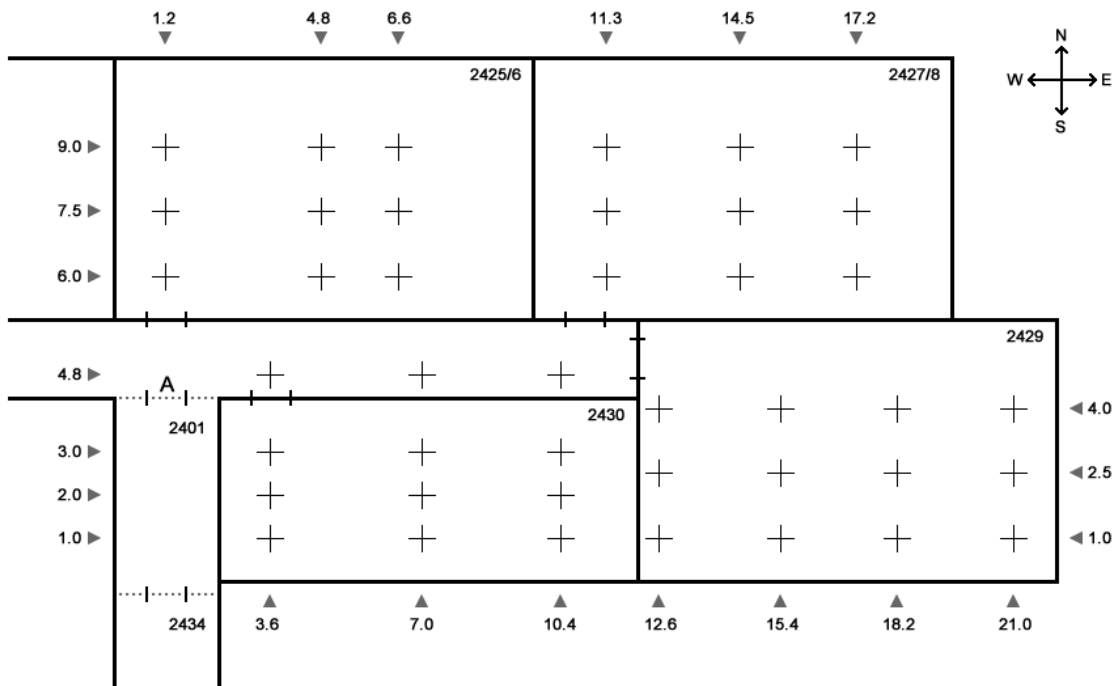


Figure 5.5: Measurement positions in rooms 2425-30

The dimensions of the 3 larger rooms are 9.7m by 6.0m while the smaller room 2430 is 9.7m by 4.2m. The crosses mark the south-west corner of the trolley table. The orientation of the Rx was kept constant throughout all the measurements at location A, with the column mark by red letter L facing north.

In-order to archive suitable received power levels we used different configurations of the following:

- 20 dB Attenuator
- 40 dBm Transmit Power +Amplifier Gain (Check!)
- 10 dB Low noise amplifier.

For this set of measurements the settings were:

Tx position	2425-2428 / corridor			2429			2430		
	Ant	Amp	LNA	Ant	Amp	LNA	Ant	Amp	LNA
N	X	√	√	X	√	√	X	√	X
S	X	√	√	X	√	X	√	√	√
E	X	√	√	X	√	√	X	√	X
W	X	√	√	X	√	√	X	√	X

Table 5.1: Configuration of the attenuator, amplifier and LNA in rooms 2325-30

Next, we measured in the corridors 2304, 2401 and 2434. The first measuring point was 2 meters south of door A, as labeled on Fig. 5.5, and 1.3m west of the eastern corridor wall. We then moved the Rx 2 meters south each time until a total of 30 meters.

The next set of measurements was done in the offices neighboring the Tx room and the nearby corridor. As seen in Fig. 5.6, these rooms are smaller and more clustered, thus providing a contrast in environment to the open space arrangement earlier.

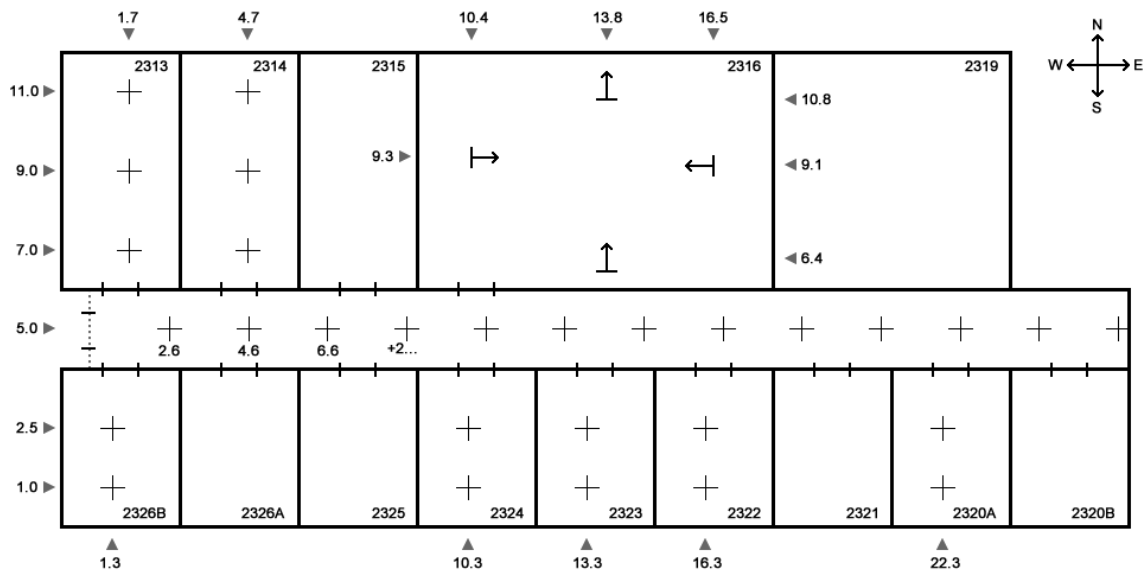


Figure 5.6: Measurements in offices immediately neighboring the Tx.

The room containing the Tx in is 9m by 6m, the bigger offices adjacent to it are 6m by 3m and the smaller ones to the south are 4m by 3m.

This time the power modifying equipments were setup as follows:

Tx position	2313/2326B			2314 / 2320-2324			Corridor 1, 11-13			Corridor 2-7			Corridor 8-10		
	An	Am	LN	An	Am	LN	An	Am	LN	An	Am	LN	An	Am	LN
N	X	√	√	X	√	√	√	√	√	√	√	√	√	√	√
S	X	X	√	X	√	√	√	√	√	√	√	√	√	√	√
E	X	X	√	X	√	√	√	√	√	√	√	√	√	√	X
W	X	√	√	X	√	√	√	√	√	√	√	X	√	√	√

Table 5.2: Configuration of the attenuator, amplifier and LNA in rooms 2313-26

The last set of measurements at location A was done outside the building, in the enclosure between the block containing the Tx and the block to its north, where we first measured in. This set of measurements was done differently to the ones inside, in the sense that we had Rx on the move instead of being at fixed points. We placed the Rx 1.5m above the ground and moved it continuously in straight lines parallel to the walls of corridor 2434; the lines were equidistantly separated by 2 meters.

The first line was 4 meters from the corridor wall and the last line was 20 meters. Due to trees and bushes in the area not all the lines are of equal length, Table 5.3 provides the full details:

Line #	Distance from the wall (m)	Direction of travel	Number of measurement blocks
1	4	S	50
2	6	N	50
3	8	S	50
4	10	N	50
5	12	S	50
6	14	S	15
7	16	S	15
8	18	S	15
9	20	S	15

Table 5.3: Details of the outdoors measurement at location A

Location B: Residential Environment

The second location we measured in was a residential area with several rows of connected houses. A birds eye's view of the area was shown earlier in Fig. 5.2. Fig 5.7 gives a view at the street level:



Figure 5.7: View of the residential area at street level

The Rx was kept stationary this time, in house 63, while the Tx was on the move instead.

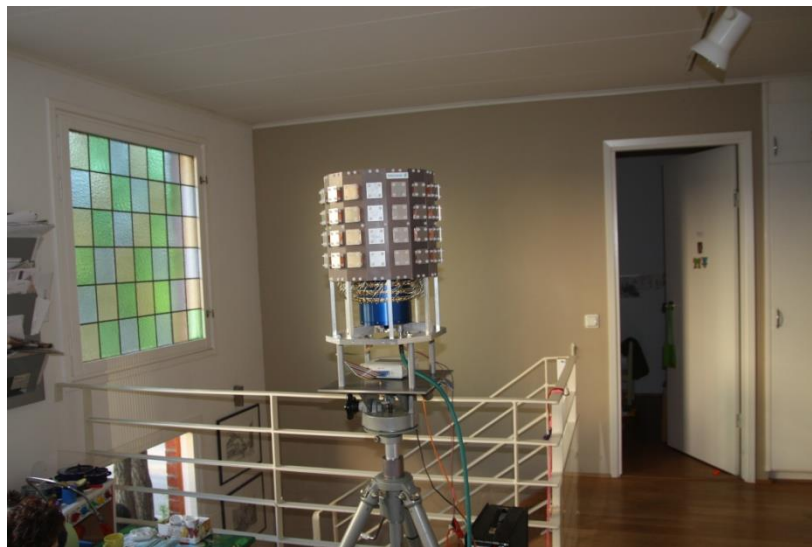


Figure 5.8 Rx in upper floor of house 63.

The configuration of the power modifiers remained constant throughout these measurements, shown in the following table:

Attenuator	OFF
Amplifier	ON
Low noise amplifier	ON

Table 5.4: Configuration of the attenuator, amplifier and LNA at location B

Initially the Rx was setup in the downstairs living room, as shown in Fig. 5.6, while it was there we managed to get the Tx into houses 51, 53 and 65. We measured both upstairs and downstairs for all 3 houses and on each floor of each house we measured all 4 orientation of the Tx (facing the different cardinal directions). Each measurement was 20 seconds long and during this time we slowly moved the Tx perpendicularly along the direction it was facing, see Fig.5.7.

After we finished in the houses we moved onto the footpaths, we aligned the Tx with the front door of a particular house and moved pass 2 houses for each 20 second measurement. One difference from the indoor measurements was that the Tx only faced east and west.

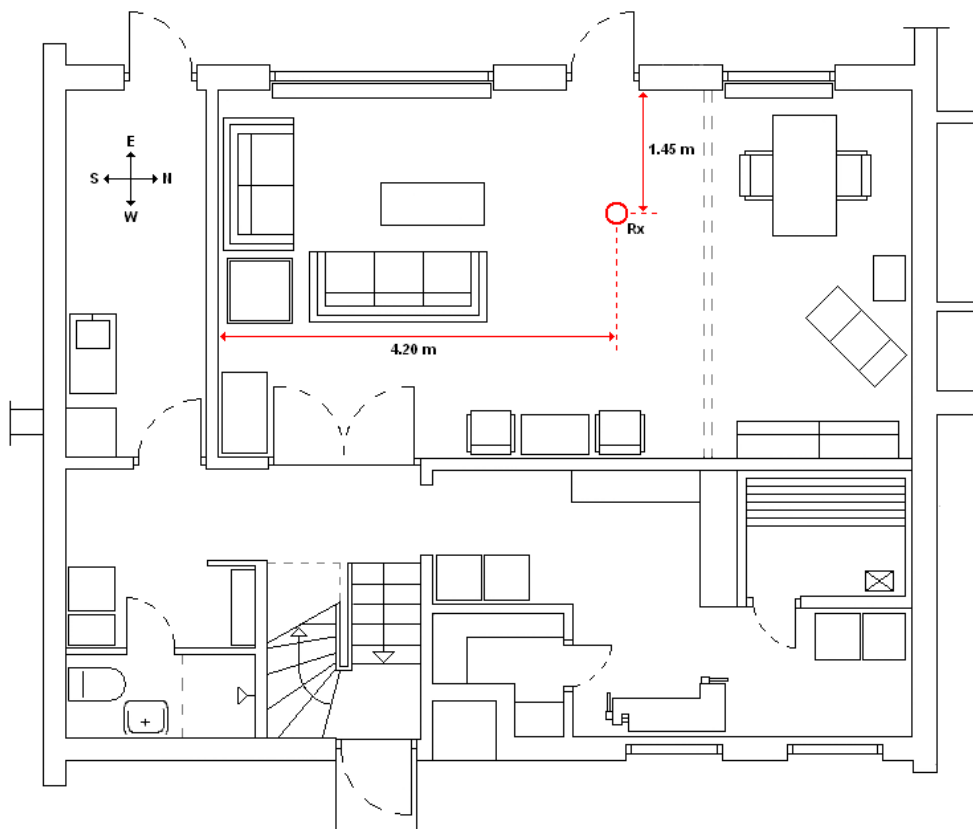


Figure 5.9: Setup of the Rx at downstairs of House 63.

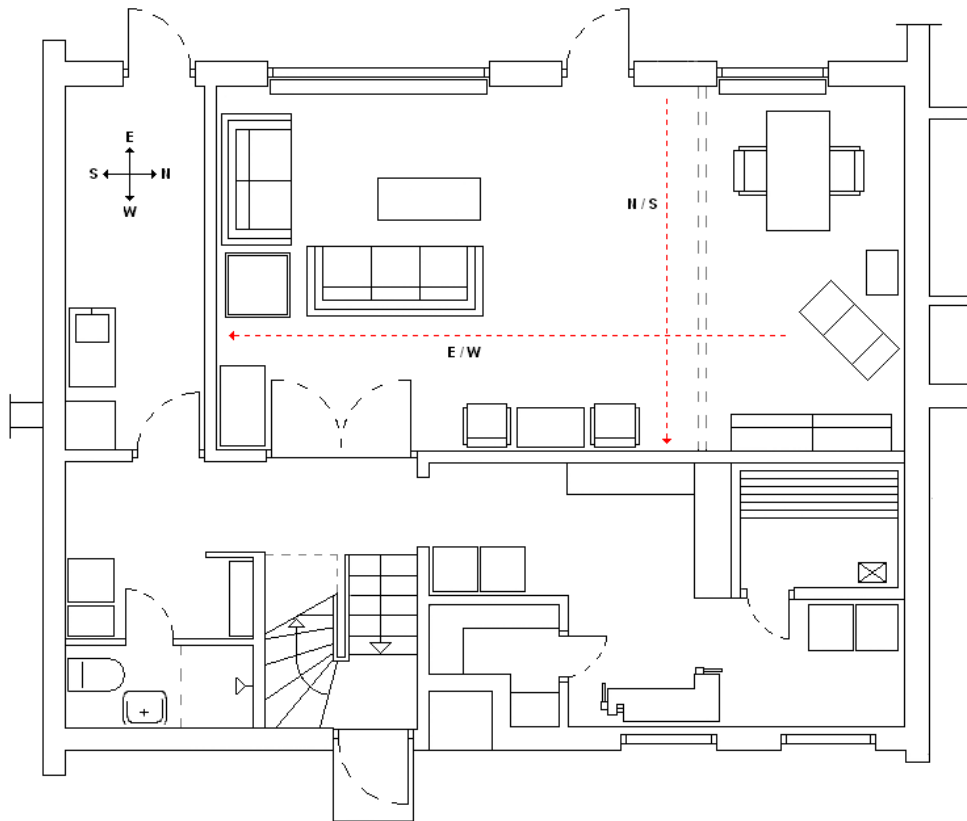


Figure 5.10: Movement of Tx during the downstairs measurements.

We proceeded to move the Rx to the upstairs and repeated the process for houses 51, 53, and 65; additionally, we also measured in the downstairs of 25 and 45. Fig 5.8 and 5.9 shows the position of the Rx and the movement of the Tx when they are upstairs, respectively. Table 5.5 summarizes the measurements taken in this environment:

Rx	Tx (indoor)	Tx (outdoor)
63 upstairs	25d, 45d, 51d, 51u, 53d, 53u, 65d, 65u	25, 29, 33, 37, 41, 43, 45, 47, 49, 51, 53
63 downstairs	51d, 51u, 53d, 53u, 65d, 65u	55, 65, 67, 71

Table 5.5: Measurements taken in the residential scenario

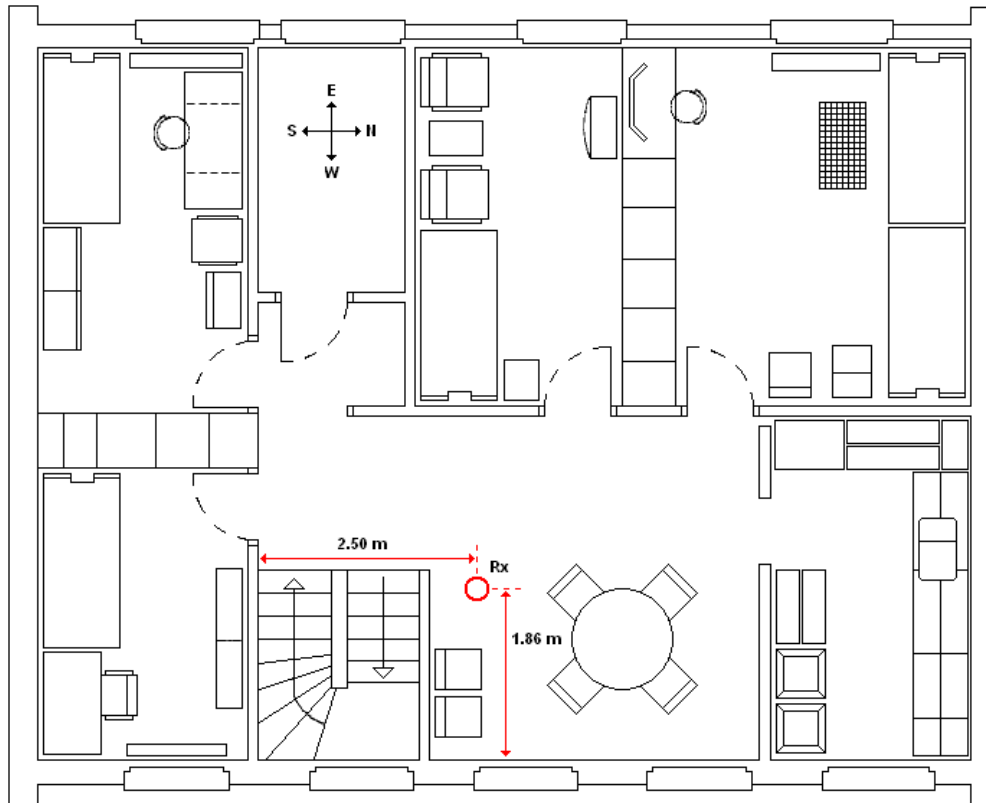


Figure 5.11: Setup of the Rx at upstairs of House 63(East is upwards, change this in the drawing)

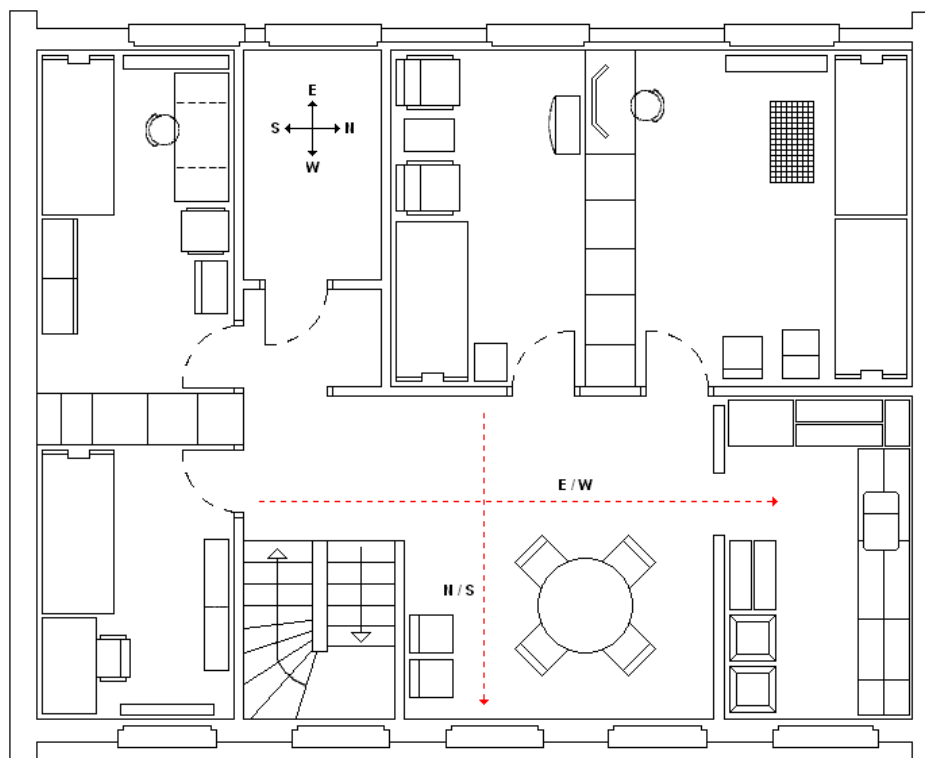


Figure 5.12: Movement of Tx during the upstairs measurements (East is upwards, change this in the drawing)

File naming

The names of the measurement files take the form of TxLocTxOriRxLoc_RxSub where:

TxLoc is the location of Tx, e.g. room 2316 = 2136, upstairs of house 51 = 51U, outside of house 51 = 51O etc. House number in outdoor measurement refers to a position west of the garden entrance

TxOri is the orientation of the Tx, i.e. N, S, E or W defined as the direction of the back plane of the antenna

RxLoc is the location of the Rx, e.g. room 2314 = 2314. Special cases are:

- corr1 = corridor 2403 (between rooms 2425 and 2430).
- corr2 = corridors 2304, 2401 and 2434.
- corr3 = corridor 2312.
- out = enclosure between 2313-19 and 2429-30 outside the building.
- some files are missing this slot before the “_”, it means the Rx is in house 63 in the residential area

RxSub is the sub location of the Rx, e.g. measurement point 1 = 001, upstairs = U etc.

Some files have the letter “a” or “b” appended near its end, it means the particular measurement was repeated for whatever reason. Always use the highest letter if they are present.

There are also errors in some of the file names and other various exceptions, a list of them is given below:

- 2316Ecorr3_002 is missing, this is because 2316Ecorr3_003 is actually measurement point 2 and 2316Ecorr3_004 is measurement point 3 and so on.
- 53UW_U should actually be 53EW_U, 53EW_U is 53EW_Ua.
- 51S_U should be 51US_U
- In the residential area, files containing 51tD represents the true downstairs of house 51.
- For 65DS_D the LNA was OFF, this is the only exception in the residential area
- 65DW_D and 65OE_D machine started halted for a few seconds after pressing start, the Tx would have already moved some distance.
- 71OE_D machine reported 3 snapshot errors, 67OE_D reported 6.

How to read sounder data

Place the unzipped “importfilter” folder under C:\...\MATLAB\R2008b (or whatever version you have) and add that path with subfolders under File/Set path...

Add the following paths in the classpath.txt (access by typing edit classpath.txt in the command window). Modify path to hyeffimport directory if necessary. Note that in Windows 7, Matlab must be run as administrator in order to save the changes to classpath.txt.

- C:\Program Files\MATLAB\R2010a\importfilter\hyeffimport\bin\MatlabXMLRead.jar
- C:\Program Files\MATLAB\R2010a\importfilter\hyeffimport\bin\sax.jar
- C:\Program Files\MATLAB\R2010a\importfilter\hyeffimport\bin\jasp-api.jar

You can now use a whole range of command. Denoting the search path to a particular measurement (say H:\DRIVEWAY2009\Measurement data\Scenario 2\07_Sc2p2_C2C_090611_SRT1_003\ for example) by “S”, the most useful commands are

```
import = hyeffimport(S);
```

```
parameter = getReadDataDefaults(import);
```

```
[import,H,axisdata] = readDataFR(import,parameter);
```

The output “H” contains the frequency response for Tx-Rx channel 1, (temporal) snapshot 1. What channel and snapshot you want to look at can be modified by altering the struct variable “parameter” through the following:

```
parameter.channel.idxlist = 1:4; % To use e.g., channels 1,2,3,4
```

```
parameter.snapshot.idxlist = 300:5:350; % To use e.g., snapshots 300,305,310,315,...,350
```

The limiting factor here is the memory of the computer. Details regarding the measurement setup can be obtained through

```
setup = getSetupRxHost(import);
```

Those are the basic commands. There are more in the sounder documentation, though they are rarely used.

There were some issues when using the import filter on a 64 bit version of matlab (including R2007b, 2009b, 2010), Matlab complained that a MEX file was missing. It can be solved by installing the 32 bit version of matlab (worked with R2007b, but is supposed to work with e.g. 2009b as well).

Hyeffimport_3_02_003 is supposed to work with 64 bit versions., but it has not been verified yet.

The 4128 channels measured are ordered so that all 128 Rx channels are measured for Tx1, then all 128 channels for Tx2 etc. Note that Rx1 is repeated once to allow the Tx switch to finish, see table for channel numbering.

Table 5.6. Measurement scheme.

Channel	Tx	Rx
1	1	1
2	1	1
3	1	2
4	1	3
...		
129	1	128
130	2	1
131	2	1
132	2	2
...		
258	2	128
...		

5.3 Analysis of Measurement Data

5.3.1 Office scenario

The figure below shows one of the measurements scenarios that took place in the E-huset building of LTH. Arrows mark the positions of the Tx along with the direction it was facing, while pluses mark the positions of the Rx. The numbers along the top left and bottom indicates the distance in meters from the lower left corner of room 2326B to each point of interest.

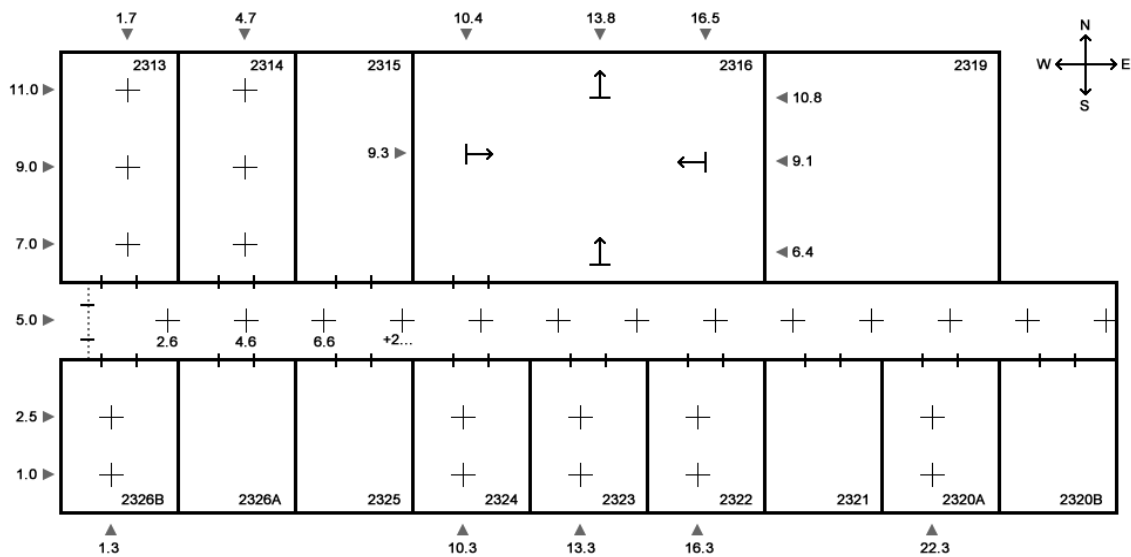


Figure 5.13: One measurement scenario in E-Huset

The data measured at each point takes the form of a giant 3D matrix (H) with its three dimensions representing snapshot, frequency and channel respectively. The precise dimension of the H matrix in the particular scenario above is 10 x 81 x 4096. Each of the matrix elements is a double precision complex number, which provides information on the received signal in the form of amplitude (absolute value) and phase (argument). Received power can then be calculated by squaring the amplitude, finally the absolute power P is converted into relative form using the equation:

$$P \text{ (dBm)} = 10 * \log_{10}P + 30 \tag{5.1}$$

A plot of the received power versus the distance in this particular scenario is shown below:

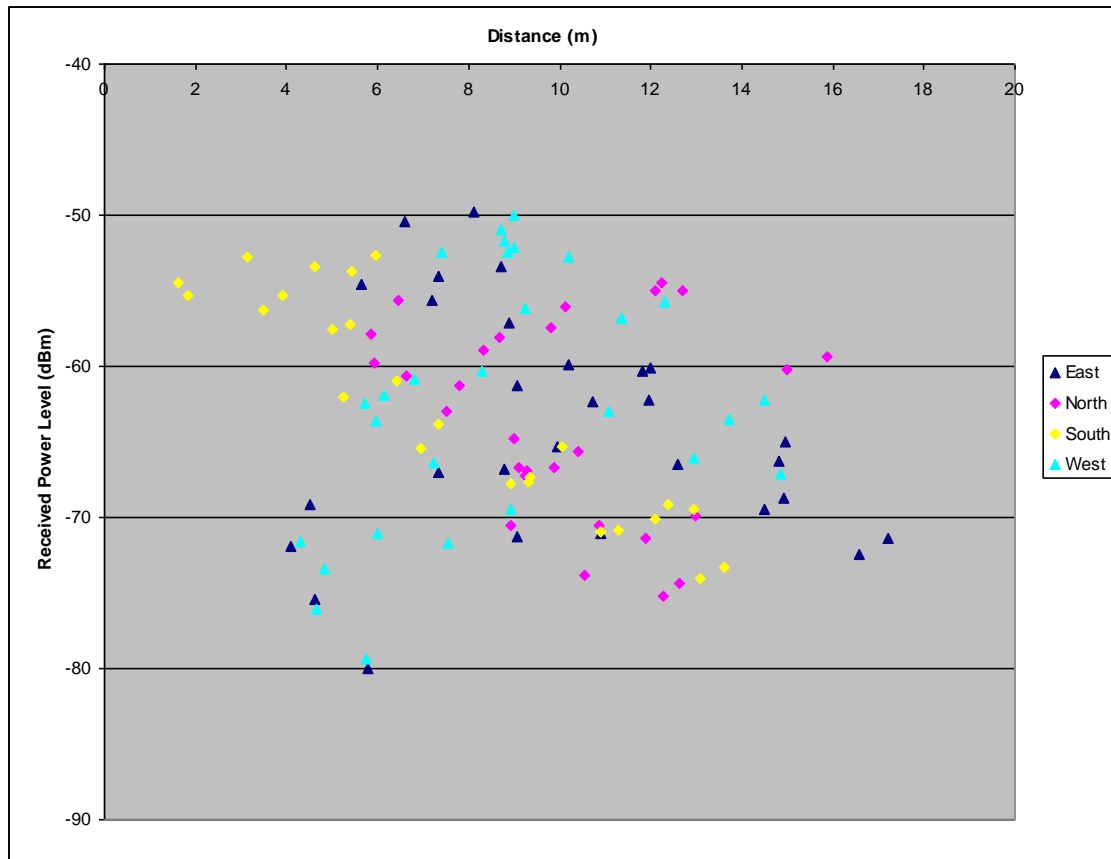


Figure 5.14: A plot of received power against straight line distance between Tx and Rx

Apart from a few outliers, the graph does show the general expected trend, that is as distance increase the received power decrease. Looking more closely at the individual Tx positions, its clear that data series from the south Tx position show the best trend by far. This can be explained by looking at the positions of the Rx relative to the position of the Tx and the direction it was facing. In the case of the south position the Tx was facing north where as almost all of the Rx positions are to its south, this creates roughly equal propagation conditions in terms of path taken from the Tx to each of the Rx and the obstacles between, thus straight line distance becomes a better indicator of path loss and the trend is shown more clearly. When we look at the west Tx position we can see that although the straight line distance to the measuring points in rooms 2313/14 are quite low, the points are in the opposite direction relative to the Tx and the direction it's facing. Therefore the signal would have to be reflected back across the transmitter room and travel a much longer distance as well as through more obstacles, hence the received power level is expected to be low. This is reflected by the outliers to the bottom left corner of the graph.

Because each of the antenna array elements was dual polarised, we can also look at the polarisation aspects of the data study the cross polarisation behaviours. The 4096 channels can be divided into four groups, VV, VH, HV, and HH, where VH represent the channels in which the Tx element is vertically polarised and the Rx element is horizontally polarised and others follow the same example.

A plot of the same data but also including separate polarisation values for each data point clearly show that, by a wide margin (up to 10 dB), the channels in the VV group have the highest received power levels and hence the least path loss.

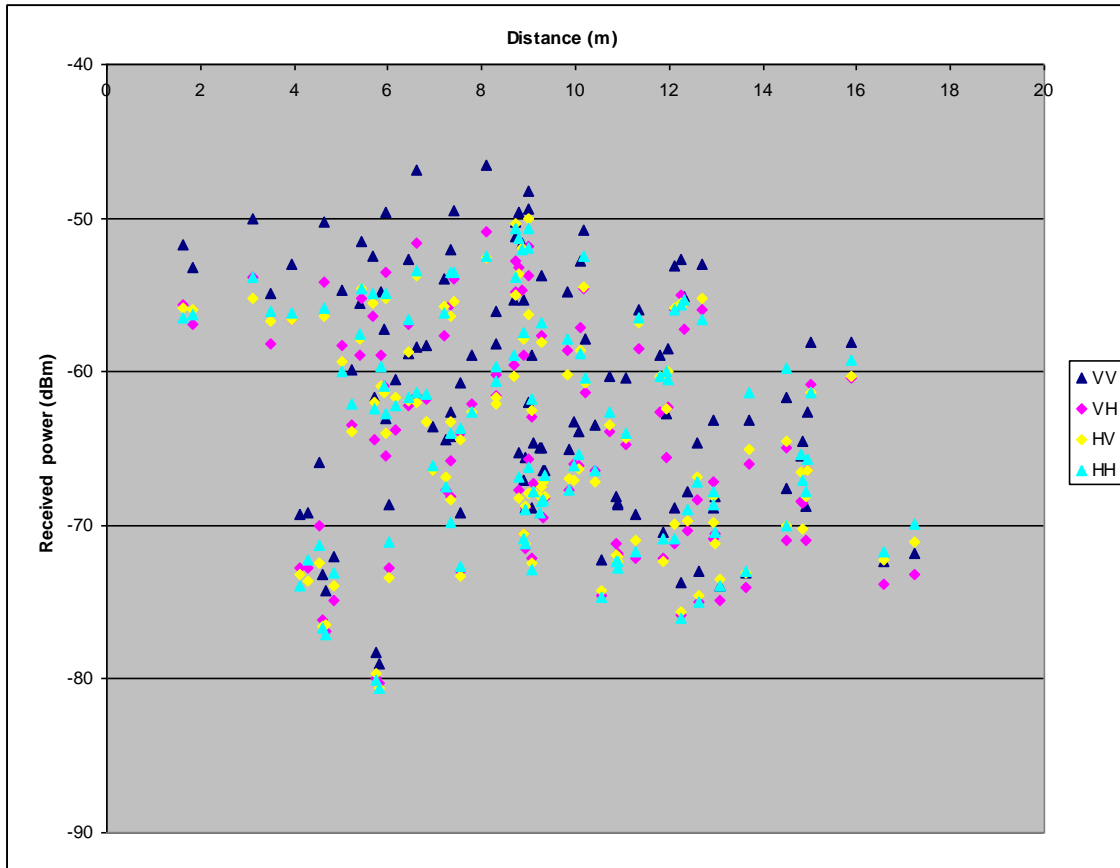


Figure 5.15: A plot of received power against straight line distance between Tx and Rx showing polarisation values

From received power levels the path loss can be calculated by taking into account the equipment set information which includes things like transmit power, antenna gains and other possible losses and gains in the system.

Another aspect we can look into this the frequency, all of the measurements were taken at a central frequency of 2.6 GHz with spread of 50 MHz. In the above scenario the frequency bandwidth is equally divided into 80 sub-bands of 0.625MHz. Figure 5.7 shows a plot of pathloss versus distance for frequencies 1, 21, 41, 61 and 81. It appears that the central frequency does not have the least pathloss and therefore highest received powers; rather frequencies 21 and 61 show the least pathloss by up to 5 dB.

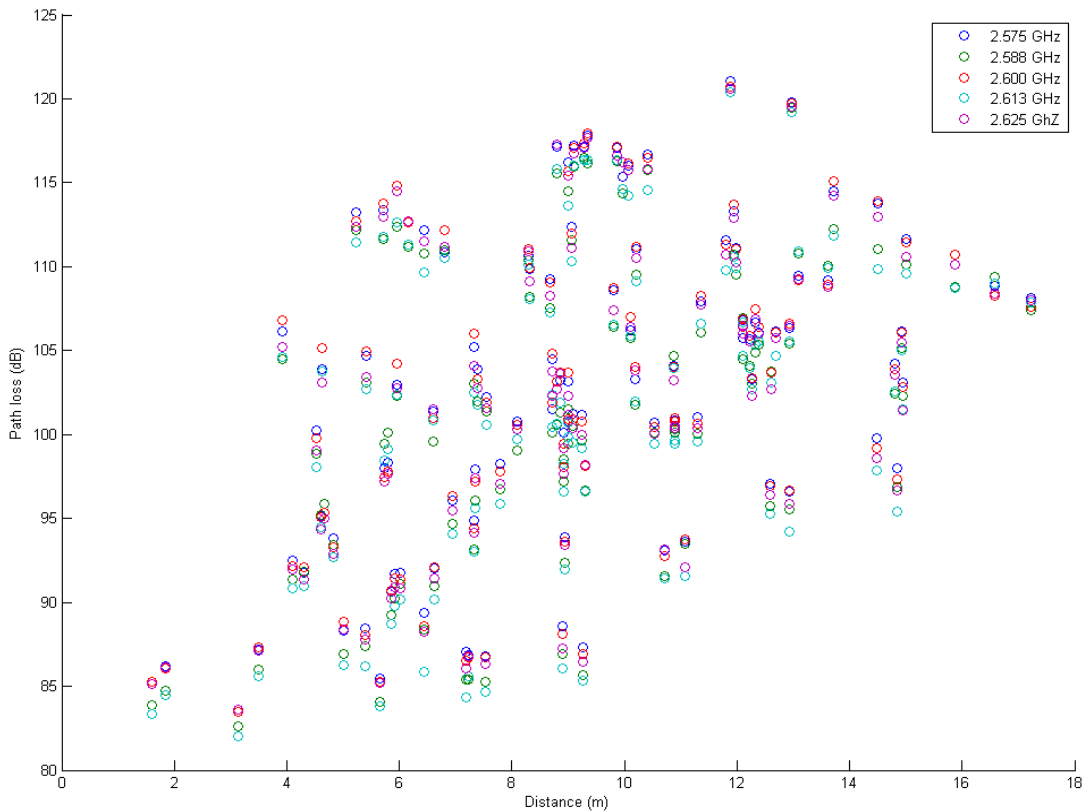


Figure 5.16: Pathloss against distance for 5 different frequencies.

Indeed when we plot received power against frequency for any measurement point we can see that the path loss the lowest around frequencies 10, 20, 60 and 70

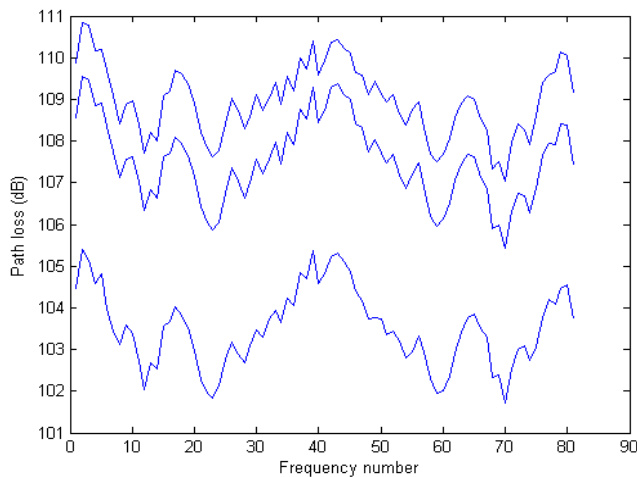


Figure 5.17: Pathloss against frequency at 3 separate measuring points.

5.3.2 Residential scenario

The measurements in the residential scenario, where signal levels in MIMO channels from one house to another was measured, was to my best knowledge the first time such measurements has take place. The Rx was placed in house 63 and the Tx was placed in various other houses as well as outside

in the pathways. Figure 5.7 shows the house numbers, table 1 shows the complete set of measurements, note that “d” denotes a downstairs position and “u” denotes an upstairs position.

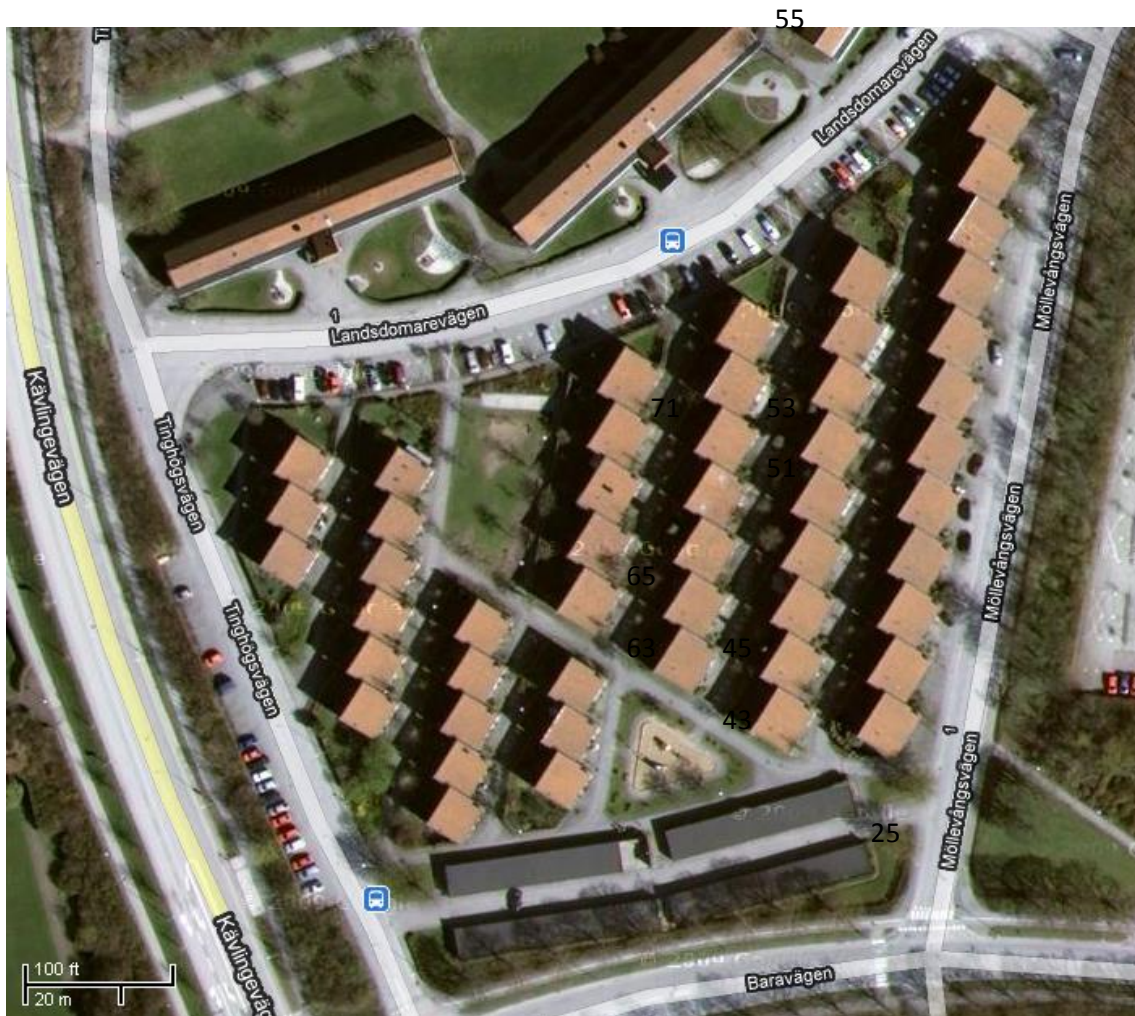


Figure 5.18: Birds-eye-view of the residential area showing the house numbers

Rx position	Tx positions	
	Indoor (inside house No.)	Outdoor (to the west of house No.)
63u	25d, 45d, 51d, 51u, 53d, 53u, 65d, 65u	25, 29, 33, 37, 41, 43, 45, 47, 49, 51, 53
63d	51d, 51u, 53d, 53u, 65d, 65u	55, 65, 67, 71

Table 5.7: Antenna positions in residential measurements

Figure 5.19 shows the channel powers between residential houses (IOI channels) when the Rx was placed upstairs.

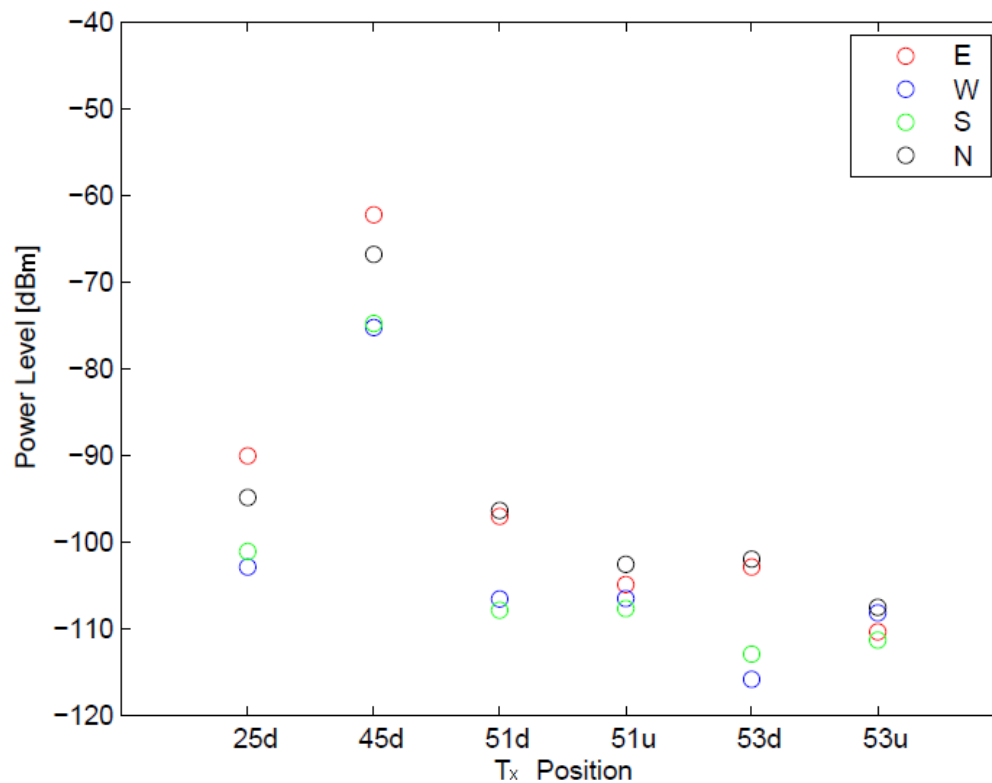


Figure 5.19: Received power level between residential hoses.

As expected, the power levels are higher when the distance between the houses is smaller. The orientation of the Tx also has a significant effect on the received power, with maximum discrepancy of around 15 dB, this could be due to the interior structure of the houses. Interestingly enough, there is no major difference in received power levels between upstairs and downstairs Tx positions. These interference power levels give us a good idea of the penetration loss to be expected from residential houses and whether they can insulate femtocell signals from surrounding in order to avoid interference.

Reference

- [1] A. Molisch, *Wireless communications*. New York, NY, USA: John Wiley & Sons, 2011.
- [2] T. Rappaport et al., *Wireless communications: principles and practice*. Prentice Hall PTR New Jersey, 1996, vol. 207.
- [3] S. Saunders and A. Aragon-Zavala, *Antennas and propagation for wireless communication systems*. Wiley, 2007.
- [4] J. Parsons, *The mobile radio propagation channel*. Wiley Online Library, 2000, vol. 81.
- [5] N. Czinik, B. Bandemer, G. Vazquez-Vilar, A. Paulraj, and L. Jalloul, July 2008 radio measurement campaign: Measurement documentation," Stanford University, Smart Antennas Research Group, Tech. Rep., July 2008.
- [6] Rusk medav channel sounders," 2008, [Online]. Available: <http://www.channelsounder.de>.
- [7] P. Luthi, *Lattice wave automata: from radio wave to fracture propagation*," Ph.D. dissertation, Computer Science Department, University of Geneva, 24 rue General-Dufour, 1211 Geneva 4, Switzerland, 1998.
- [8] G. Durgin, *Theory of stochastic local area channel modeling for wireless communications*," Ph.D. dissertation, Citeseer, 2000.
- [9] B. Fleury, M. Tschudin, R. Heddergott, D. Dahlhaus, and K. Ingeman Pedersen, Channel parameter estimation in mobile radio environments using the sage algorithm," *Selected Areas in Communications, IEEE Journal on*, vol. 17, no. 3, pp. 434 - 450, Mar. 1999.
- [10] G. Durgin, *Space-time wireless channels*. Prentice Hall, 2003.
- [11] M. Simon and M. Alouini, *Digital communication over fading channels*. Wiley-IEEE Press, 2004, vol. 86.

- [12] J. Lu, K. Letaief, J. Chuang, and M. Liou, "M-PSK and M-QAM BER computation using signal-space concepts," *IEEE Transactions on Communications*, vol. 47, no. 2, pp. 181-184, 1999.
- [13] P. Lee, "Computation of the bit error rate of coherent m-ary psk with gray code bit mapping," *IEEE Transactions on Communications*, vol. 34, no. 5, pp. 488-491, 1986.
- [14] J. Lassing, E. Strom, E. Agrell, and T. Ottosson, "Computation of the exact bit-error rate of coherent m-ary psk with gray code bit mapping," *IEEE Transactions on Communications*, vol. 51, no. 11, pp. 1758-1760, 2003.
- [15] D. Yoon, K. Cho, and J. Lee, "Bit error probability of m-ary quadrature amplitude modulation," in *IEEE 52nd Vehicular Technology Conference, VTC-Fall, 2000*, vol. 5. IEEE, 2000, pp. 2422-2427.
- [16] K. Cho and D. Yoon, "On the general BER expression of one-and two dimensional amplitude modulations," *IEEE Transactions on Communications*, vol. 50, no. 7, pp. 1074-1080, 2002.
- [17] A. Abdi, C. Tepedelenlioglu, M. Kaveh, and G. Giannakis, "On the estimation of the K parameter for the rice fading distribution," *IEEE Communications Letters*, vol. 5, no. 3, pp. 92 {94, Mar. 2001.
- [18] J. Sijbers, A. Den Dekker, P. Scheunders, and D. Van Dyck, "Maximum likelihood estimation of rician distribution parameters," *IEEE Transactions on Medical Imaging*, vol. 17, no. 3, pp. 357-361, 1998.
- [19] C. Carobbi and M. Cati, "The absolute maximum of the likelihood function of the rice distribution: Existence and uniqueness," *IEEE Transactions on Instrumentation and Measurement*, vol. 57, no. 4, pp. 682-689, 2008.
- [20] L. Greenstein, S. Ghassemzadeh, V. Erceg, and D. Michelson, "Ricean K factors in narrow-band fixed wireless channels: Theory, experiments, and statistical models," *IEEE Transactions on Vehicular Technology*, vol. 58, no. 8, pp. 4000-4012, 2009.
- [21] G. Ridgway, "RICEFIT," 2008, [Online] <http://www.mathworks.com/matlabcentral/fileexchange/14237ricerician-distribution/content/rician/ricefit.m>.
- [22] A. Abdi and M. Kaveh, "Performance comparison of three different estimators for the nakagami m parameter using monte carlo simulation," *IEEE Communications Letters*, vol. 4, no. 4, pp. 119-121, 2000.
- [23] Q. Zhang, "A note on the estimation of nakagami-m fading parameter," *Communications Letters, IEEE*, vol. 6, no. 6, pp. 237{238, 2002.
- [24] H. Thom, "A note on the gamma distribution," *Monthly Weather Review*, vol. 86, no. 4, pp. 117-122, 1958.
- [25] J. Greenwood and D. Durand, "Aids for fitting the gamma distribution by maximum likelihood," *Technometrics*, vol. 2, no. 1, pp. 55-65, 1960.
- [26] K. Bowman and L. Shenton, "Properties of estimators for the gamma distribution," *History and Philosophy of Logic*, vol. 11, no. 4, pp. 377-519, 1982.
- [27] R. D'Agostino and M. Stephens, *Goodness-of-fit techniques*. New York: Marcel Dekker, 1986, vol. 68.
- [28] F. Massey Jr, "The kolmogorov-smirnov test for goodness of fit," *Journal of the American Statistical Association*, vol. 46, no. 253, pp. 68-78, 1951.
- [29] H. Lilliefors, "On the kolmogorov-smirnov test for normality with mean and variance unknown," *Journal of the American Statistical Association*, vol. 62, no. 318, pp. 399-402, 1967.
- [30] "On the kolmogorov-smirnov test for the exponential distribution with mean unknown," *Journal of the American Statistical Association*, vol. 64, no. 325, pp. 387-389, 1969.
- [31] T. Anderson and D. Darling, "A test of goodness of fit," *Journal of the American Statistical Association*, vol. 49, no. 268, pp. 765-769, 1954.
- [32] S. Wyne, T. Santos, F. Tufvesson, and A. Molisch, "Channel measurements of an indoor office scenario for wireless sensor applications," in *IEEE Global Telecommunications Conference, GLOBECOM'07*. IEEE, 2007, pp. 3831-3836.
- [33] V. Tarokh, N. Seshadri, and A. Calderbank, "Space-time codes for high data rate wireless communication: Performance criterion and code construction," *IEEE Transactions on Information Theory*, vol. 44, no. 2, pp. 744-765, 1998.
- [34] J.Zhang and G.de la Roche, *Femtocells: Technologies and Deployment*. JohnWiley & Sons Ltd, January 2010.
- [35] D. Lopez-Perez, A. Valcarce, G. de la Roche, and J. Zhang, "OFDMA Femtocells: A Roadmap on Interference Avoidance," *IEEE Communications Magazine*, September 2009.
- [36] Y. Miura, Y. Oda, and T. Taga, "Outdoor-to-indoor propagation modelling with the identification of path passing through wall openings," in *The 13th IEEE International Symposium on Personal, Indoor and Mobile Radio Communications (PIMRC)*, vol. 1, Sept 2002.
- [37] S. Stavrou and S. Saunders, "Factors influencing outdoor to indoor radiowave propagation," in *Twelfth International Conference on Antennas and Propagation(ICAP 2003)*, vol. 2, April 2003.
- [38] S.Wyne, N. Czink, J. Karedal, P. Almers, F. Tufvesson, and A.Molisch, "A Cluster-Based Analysis of Outdoor-to-

- Indoor Office MIMO Measurements at 5.2 GHz,” in IEEE 64th Vehicular Technology Conference (VTC-Fall), Sept 2006.
- [39] T. Kurner and A. Meier, “Prediction of Outdoor and Outdoor-to-Indoor Coverage in Urban Areas at 1.8 GHz,” *IEEE Journal on Selected Areas in Communications*, vol. 20, pp. 496–506, 2002.
- [40] S. Reynaud, M. Mouhamadou, K. Fakihi, O. Akhdar, C. Decroze, D. Carsenat, E. Douzon, and T. Monediere, “Outdoor to Indoor Channel Characterization by Simulations and Measurements for Optimising WiMAX Relay Network Deployment,” in *IEEE 61st Vehicular Technology Conference VTC-Spring*, April 2009.
- [41] G. de la Roche, P. Flipo, Z. Lai, G. Villemaud, J. Zhang, and J.-M. Gorce, “Combination of geometric and finite difference models for radio wave propagation in outdoor to indoor scenarios,” in *European Conference on Antennas and Propagation (EuCAP2010)*, Barcelona, Spain, April 2010.
- [42] V. Degli-Esposti, F. Fuschini, E. Vitucci, and G. Falciasecca, “Speed-Up Techniques for Ray Tracing Field Prediction Models,” *IEEE Transactions on Antennas and Propagation*, vol. 57, pp. 1469–1480, May 2009.
- [43] D. Schettino, F. Moreira, and C. Rego, “Efficient Ray Tracing for Radio Channel Characterization of Urban Scenarios,” *IEEE Transactions on Magnetics*, vol. 43, pp. 1305–1308, April 2007.
- [44] Y. Corre and Y. Lostanlen, “3D urban propagation model for large ray-tracing computation,” in *International Conference On Electromagnetics In Advanced Applications*, Torino, Italy, September 2007.
- [45] G. Wolfle, B. E. Gschwendtner, and F. M. Landstorfer, “Intelligent ray tracing – a new approach for the field strength prediction in microcells,” in *Vehicular Technology Conference*, 5 2007, pp. 790–794.
- [46] Z. Lai, N. Bessis, G. de la Roche, H. Song, J. Zhang, and G. Clapworthy, “An intelligent ray launching for urban propagation prediction,” in the *Third European Conference On Antennas and Propagation (EuCAP)*, Berlin, Germany, 3 2009.
- [47] Z. Lai, N. Bessis, G. de la Roche, H. Song, J. Zhang, and G. Clapworthy, “A new approach to solve angular dispersion of discrete ray launching for urban scenarios,” in *Loughborough Antennas and Propagation Conference (LAPC)*, Loughborough, UK, November 2009.
- [48] Z. Lai, N. Bessis, P. Kuonen, G. De La Roche, J. Zhang, and G. Clapworthy, “The development of a parallel ray launching algorithm for wireless network planning,” *International Journal of Distributed Systems and Technologies (IJ DST)*, 2010.
- [49] K. Yee, “Numerical Solution of Initial Boundary Value Problems Involving Maxwell’s Equations in Isotropic Media,” *IEEE Transactions on Antennas and Propagation*, pp. 302–307, May 1966.
- [50] G. Kondylis, F. DeFlaviis, G. J. Pottie, and Y. Rahmat-Samii, “Indoor channel characterization for wireless communications using reduced finite difference time domain,” *Proceedings of the IEEE Vehicular Technology Conference*, vol. 3, pp. 1402–1406, May 1999.
- [51] A. Lauer, I. Wolff, A. Bahr, J. Pamp, and J. Kunisch, “Multi-mode fdtd simulations of indoor propagation including antenna properties,” in *Proceedings of the IEEE 45th Vehicular Technology Conference*, Chicago, USA, 1995, pp. 454–458.
- [52] M. Pahud, F. Guidec, and T. Cornu, “Performance evaluation of a radiowave propagation parallel simulator,” in *Proceedings of the Third International Conference on Massively Parallel Computing System*, USA, 4 1998.
- [53] J.-M. Gorce, K. Jaffres-Runser, and G. de la Roche, “Deterministic approach for fast simulations of indoor radio wave propagation,” *IEEE Transactions on Antennas and Propagation*, vol. 55, pp. 938–942, March 2007.
- [54] G. de la Roche, K. Jaffres-Runser, and J.-M. Gorce, “On predicting in-building WIFI coverage with a fast discrete approach,” *International Journal of Mobile Network Design and Innovation*, vol. 2, pp. 3–12, 2007.
- [55] J.-M. Gorce, G. Villemaud, and P. Flipo, “On Simulating Propagation for OFDM/MIMO Systems with the MRFDPF Model,” in *The 4th European Conference on Antennas and Propagation (EuCAP2010)*, Barcelona, Spain, April 2010.
- [56] L. Nagy, R. Dady, and A. Farkasvolgyi, “Algorithmic complexity of FDTD and ray tracing method for indoor propagation modelling,” in *The Third European Conference On Antennas and Propagation*, Berlin, Germany, 3 2009.
- [57] Y. Wang, S. Safavi-Naeini, and S. K. Chaudhuri, “A hybrid technique based on combining ray tracing and fdtd methods for site-specific modeling of indoor radio wave propagation,” *IEEE Transaction on Antennas and Propagation*, vol. 48, no. 5, pp. 743–754, May 2000.
- [58] S. Reynaud, A. Reineix, C. Guiffaut, and R. Vauzelle, “Modeling indoor propagation using an indirect hybrid method combining the utd and the fdtd methods.” in *7th European Conference on Wireless Technology*, Amsterdam, October 2004.
- [59] M. Thiel and K. Sarabandi, “3D-Wave Propagation Analysis of Indoor Wireless Channels Utilizing Hybrid Methods,” *IEEE Transactions on Antennas and Propagation*, vol. 57, pp. 1539–1546, 2009.
- [60] V. Granville, M. Krivanek, and J.-P. Rasson, “Lipschitzian Optimization without the Lipschitz Constant,” *Optimization Theory and Applications*, vol. 16, pp. 652–656, June 1994.
- [61] D. Jones, C. Perttunen, and B. Stuckman, “Lipschitzian Optimization without the Lipschitz Constant,” *Optimization Theory and Applications*, vol. 79, pp. 157–181, October 1993.

3. Perspectives

All measurements done that are described in this deliverable permit to validate the performance of the radio propagation tools developed in this project. Particularly, the extraction of radio link statistics in a stochastic way is a great improvement to offer more efficient radio planning tools, and all the principle of the implementation of the proposed methods in an operational tool was demonstrated based on realistic measurements.

4. Publications and software results

books and journal papers are in bold characters.

- [1] **Z. Lai, G. Villemaud, M. Luo, J. Zhang, Chapter 2 - Radio Propagation Modelling, in Book "Heterogeneous Cellular Networks - Theory, Simulation, and Deployment" (edited by Xiaoli Chu, David Lopez-Perez, Fredrik Gunnarsson, and Yang Yang), Cambridge University Press, 2012.**
- [2] **D. Umansky, J.-M. Gorce, M. Luo, G. De la Roche, and G. Villemaud, Computationally Efficient MR-FDPF and MR-FDTLM Methods for Multifrequency Simulations, IEEE Transactions on Antennas and Propagation, 61(3):1309 - 1320, 2012.**
- [3] M. Luo, N. Lebedev, G. Villemaud, G. De La Roche, J. Zhang, and J. Gorce, On predicting large scale fading characteristics with the MR-FDPF method, 6th European Conference on Antennas and Propagation (EuCAP 2012), Prague, Czech Republic, March, 2012.
- [4] **M. Luo, G. Villemaud, J.-M. Gorce, and J. Zhang, Realistic Prediction of BER and AMC for Indoor Wireless Transmissions, IEEE Antennas and Wireless Propagation Letters, vol. 11, pp. 1084 – 1087, 2012.**
- [5] M. Luo, G. Villemaud, J. Weng, J.-M. Gorce, and J. Zhang, Realistic Prediction of BER and AMC with MRC Diversity for Indoor Wireless Transmissions, in IEEE Wireless Communications and Networking Conference (WCNC 2013), Shanghai, China, April, 2013.
- [6] M. Luo, G. Villemaud, J.-M. Gorce, and J. Zhang, “Realistic Prediction of BER for Adaptive OFDM Systems”, in 7th European Conference on Antennas and Propagation (Eucap 2013), Gothenburg, Sweden, April, 2013.

PhD thesis of iPLAN researchers

- [7] **Meiling Luo, “Indoor radio propagation modeling for system performance prediction”, PhD Thesis, INSA-Lyon, 17th July, 2013.**